2018-06

# Complex-Based Polymer-Modified Pencil Graphite Electrode for Electrochemical Determination of Selected Drugs in Pharmaceutical and Biological Samples

Abebaw, Shitahun


**BAHIR DAR UNIVERSITY**

**COLLEGE OF SCIENCE**

**DEPARTMENT OF CHEMISTRY**

**DOCTORAL THESIS**

# Complex-Based Polymer-Modified Pencil Graphite Electrode for Electrochemical Determination of Selected Drugs in Pharmaceutical and Biological Samples

---

**By**

**Abebaw Shitahun**

**June, 2018 EC.**

**Bahir Dar, Ethiopia**

**BAHIR DAR UNIVERSITY**

**COLLEGE OF SCIENCE**

**DEPARTMENT OF CHEMISTRY**

**Doctoral Dissertation**

# Complex-Based Polymer-Modified Pencil Graphite Electrode for Electrochemical Determination of Selected Drugs in Pharmaceutical and Biological Samples


**By**

**Abebaw Shitahun**


A dissertation submitted in Partial Fulfillment of the Requirements for the Degree of Doctor of Philosophy in Analytical chemistry


**Minaleshewa Atlabachew (Prof. in Analytical chemistry)**

**Belete Asefa (Asso. prof. in physical chemistry)**

**Atakilt Abebe (Prof. in inorganic chemistry)**

**Amare Benor (Asso. Prof. in physics)**


**June, 2018 EC.**

**Bahir Dar, Ethiopia**

**BAHIR DAR UNIVERSITY**
**COLLEGE OF SCIENCE**

**DEPARTMENT OF CHEMISTRY**

# Declaration

This is to certify that the thesis entitled "**Complex-Based Polymer-Modified Pencil Graphite Electrode for Electrochemical Determination of Selected Drugs in Pharmaceutical and Biological Samples**, submitted in partial fulfillment of the requirements for the degree of Doctor of Philosophy in Analytical chemistry of Department of Chemistry, Bahir Dar University, is a record of original work carried out by me and has never been submitted to this or any other institution to get any other degree or certificates. The assistance and help I received during the course of this investigation have been duly acknowledged.

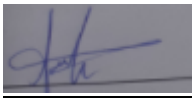


Abebaw Shitahun Date

**BAHIR DAR UNIVERSITY**
**COLLEGE OF SCIENCE**

**DEPARTMENT OF CHEMISTRY**

**Approval of Dissertation**

I hereby certify that I have supervised, read, and evaluated this dissertation titled "**Complex-Based Polymer-Modified Pencil Graphite Electrode for Electrochemical Determination of Selected Drugs in Pharmaceutical and Biological Samples**" by Abebaw Shitahun Ayicheh prepared under my guidance. I recommend the dissertation be submitted for oral defense.

| | | |
|---|---|---|
| **Prof. Minaleshewa Atlabachew** | | June 29, 2026 |
| Advisor's name | Signature | Date |
| **Dr. Belete Asefa** | | June 29, 2026 |
| Co-Advisor's name | Signature | Date |
| **Prof. Atakilt Abebe** | | June-29-2026 G.C |
| Co-Advisor's name | Signature | Date |
| **Dr. Amare Benor** | | June-29-2026 G.C |
| Co-Advisor's name | Signature | Date |
| **Dr. Yonas Beyene** | | 29/6/2026 |
| Department Head's name | Signature | Date |

**Bahir Dar University**

**College of Science**

**Department of Chemistry**

**Approval of Dissertation Defense**

As members of the board of dissertation examiners, we reviewed the thesis entitled "**Complex-Based Polymer-Modified Pencil Graphite Electrode for Electrochemical Determination of Selected Drugs in Pharmaceutical and Biological Samples"** conducted by Mr. Abebaw Shitahun Ayicheh. We hereby approve that the dissertation meets the requirements for the award of the degree of Doctor of Philosophy in Analytical chemistry.

**Board of Examiners**

| External examiner name | Signature | Date |
|---|---|---|
| **Dr. Molla Tefera** |  |  |
| Internal examiner name | Signature | Date |
| **Dr. Tihitinna Asmellash** |  |  |
| **Dr. Hailu Shiferaw** | 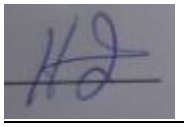 | 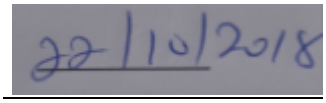 |
| Chair person's name | Signature | Date |
| **Dr. Yonas Beyene** |  | 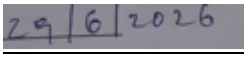 |

**TABLE OF CONTENTS**

## LIST OF FIGURES

## LIST OF TABLES

## LIST OF SCHEME

## LIST OF ACRONYMES

| | |
|---|---|
| ABS | Acetate buffer solutions |
| ASV | Anodic stripping voltammetry |
| BRB | Britton–Robinson buffer |
| CPE | Carbon paste electrode |
| CV | Cyclic voltammetry |
| DPV | Differential pulse voltammetry |
| EIS | Electrochemical impendence spectroscopy |
| FTIR | Fourier transfer infrared |
| GCE | Glassy carbon electrode |
| LOD | Limit of detection |
| NPs | Nanoparticles |
| PBS | Phosphate buffer solution |
| SEM | Scanning electron microscopy |
| SWV | Square wave voltammetry |
| UV-Vis | Ultra violet visible |
| XRD | X-ray diffraction |
| GO | Graphite oxide |
| HPLC | High-performance liquid chromatography |
| LSV | Linear sweep voltammetry |
| RPM | Rotation per minute |
| CME | Chemically modified electrode |
| PGE | Pencil graphite electrode |
| Cpro | Ciprofloxacin |
| Nor | Norfloxacin |
| AdSSWV | Adsorptive stripping square wave voltammetry |
| Caff | Caffeine |
| Chr | Chrysin |
| ICP-OES | Inductively Coupled Plasma Optical Emission Spectrophotometry |
| Rct | Charge transfer resistance |
| ResoNa | Sodium resorcinolate |
| FTO | Fluorine-doped tin oxide |
| $C_{dl}$ | Double layer capacitance |
| $K^o$ | Heterogeneous electron transfer rate constant |
| $I_{pa}$ | Anodic peak current |
| $E_{pa}$ | Anodic peak potential |
| $R^2$ | Correlation coefficient |
| LMCT | Ligand-to-metal charge transfer |

## ACKNOWLEDGEMENTS

First of all, I am thankful to Almighty God, the ultimate source of wisdom and knowledge. I am thankful to my honorable course instructor and advisor, Prof. Minaleshewa Atlabachew, for his continuous and active follow-up, close supervision, and support during the course study and research work. I want to thank my honorable advisors, Prof. Atakilt Abebe, and Dr. Belete Asefa for their constructive comments, insightful recommendations, and for sharing of their valuable time, resources, and technical advice, all of which have contributed to the successful completion of this research work. I want to thank my honorable advisor, Dr. Amare Benor, for his constructive comments, for sharing all his resources and for his technical advice in the successful completion of this research work. I would like to thank Dr. Yonas Beyene, for his time and willingness to assist me in any activity I desire. I would also like to thank Dr. Melaku Metto, Dr.Adane Kassa and Kidanemariam Teklay for their technical support, encouragement, and resource support.

I greatly acknowledge the Swedish International Development Cooperation Agency (SIDA) through the International Science Programme, Uppsala University (ISP), for their financial support. I want to take this opportunity to express my gratitude to my home university, Debre Markos University, for allowing me to pursue my PhD. Additionally, I extend my gratitude to the Chemistry Department of the College of Natural Sciences at Bahir Dar University for giving me access to laboratory equipment and chemicals. I also want to express my appreciation for all the staff at Bahir Dar University's chemistry department. I want to thank Felege Hiwot Referral Hospital for providing a urine sample. Lastly, I would extend my heartfelt gratitude to my family and friends for their love, tolerance, and encouragement throughout my study period.

## ABSTRACT

Ciprofloxacin (Cpro) and Norfloxacin (Nor) are drugs belonging to the fluoroquinolones class, commonly used to treat bacterial infections of humans and animals. However, improper use, unmetabolized excretion, and overuse of Cpro and Nor can lead to bacterial resistance. To mitigate this risk, continuous monitoring using sensitive and selective analytical techniques are required. In this work, Manganese (II)-chrysin ($[Mn(Chr)_3]Cl_2$), Copper (II)-chrysin ($[Cu(Chr)_2Cl]Cl$), and Copper (II)-resorcinol ($Na_2[Cu(Reso)_3Cl]$) complexes were synthesized, characterized and applied to modify pencil graphite electrode (PGE) for electrochemical determination of Cpro, Nor, and (Nor and Caffeine) simultaneously in pharmaceuticals samples, milk samples, urine samples and in the presence of different potential interferences. The tip of the PGE electrode has been immersed in the monomer solution and modified using the potentiodynamic electropolymerization method by placing the pencil graphite electrode inside the prepared pencil holder using the selected potential window and scan cycle. The modified electrode was characterized using CV, electrochemical impedance spectroscopic (EIS), UV-Vis, digital optical microscopy, and contact angle with relative to bare PGE electrode. Both the developed (SWV and AdSSWV) electrochemical methods and the UV-Vis spectroscopic method were calibrated and used for the determination of the concentration of Cpro, Nor, and Caffeine in different sample matrices and the results were compared. The percent recoveries in pharmaceuticals ranged from 84.5 to 114.3%, in urine samples 92.8 to 114.9%, and in milk samples 81.80% to 91.13%. The values of dynamic range, LoD, and sensitivity of the developed method for Cpro were in 1-200 µM, 0.54, and 0.16, respectively. Dynamic range, LoD, and sensitivity for Nor were in 1-100 µM, 0.09, and 0.5, respectively and for Caff were in 10-300 µM, 3.05, and 0.09, respectively. The developed methods were selective towards the tested analytes in the presence of different potential interferences and can be taken for the determination of Cpro, Nor and, Caff in different sample matrices.



**Keywords**: Ciprofloxacin, Pencil Graphite Electrode, electropolymerization, chemical sensor, Norfloxacin, Caffeine, Monomer, Polymer, Thin-film, Complexes

# 1. CHAPTER ONE: INTRODUCTION

## 1.1. Background

Fluoroquinolones are powerful, systemic antibiotics with a range of favorable features, such as high oral bioavailability, a wide volume of distribution, and broad-spectrum antibacterial action [1, 2]. They are used to treat bacterial infections in both people and animals [3, 4]. They are efficient against gram-positive and gram-negative bacteria. Pneumonia, urinary tract infections, intra-abdominal infections, skin infections, and inflammatory illnesses are just a few of the conditions that can be addressed when a patient has a bacterial infection. Gyrase and topoisomerase, the two enzymes crucial for bacterial DNA replication, are inhibited by fluoroquinolones. Because the DNA produced is faulty and incomplete, it disintegrates and causes cell death[5, 6].

The chemical structure of quinolone antibiotics includes a fluorine atom and has a bicyclic core structure. The presence of fluorine atoms in fluoroquinolones' chemical structure offers fluoroquinolones more antibacterial activities and makes it more broad spectrum of activity[7]. Fluoroquinolones such as ciprofloxacin, levofloxacin, moxifloxacin, delafloxacin, gemifloxacin, norfloxacin, enrofloxacin, and ofloxacin are often accessible[8]. The chemical structures of some fluoroquinolones are shown below.

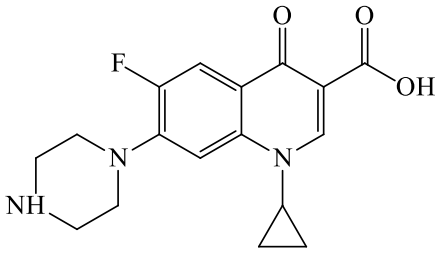


Ciprofloxacin

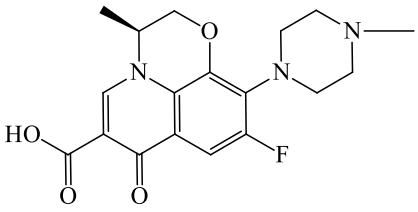


Levofloxacin

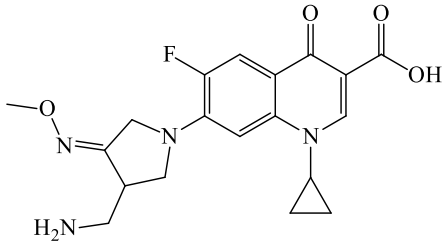


Gemifloxacin

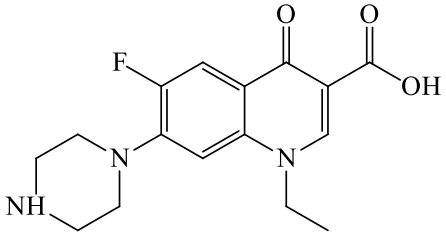


Norfloxacin

Scheme 1. 1: Chemical structure of some fluoroquinolones

Fluoroquinolones' antimicrobial resistance has increased with their extensive use[9]. Moreover, fluoroquinolones have the potential to produce significant negative side effects. Fluoroquinolone use is therefore typically confined to situations in which the benefits clearly outweigh the risks [10, 11]. Therefore, continuous monitoring and studying fluoroquinolones using sensitive and selective detection methods is required.

Ciprofloxacin (Cpro) is a synthetic second-generation drug belonging to the fluoroquinolones class (Scheme 1.1), which is used to treat bacterial infections of the respiratory, urinary tract, gastrointestinal, and skin[12]. Un-metabolized excretion, improper and overuse of Cpro can lead to bacterial resistance [7]. The resistance causes the available treatment options for common bacterial infections to become ineffective. As a result, patients may need more care, use more expensive antibiotics with severe side effects, or result in death [13].

Similarly, Norfloxacin (Nor) is a drug belonging to the fluoroquinolones class (Scheme 1.1), which is also used to treat bacterial infections of the urinary tract, skin, and respiratory system. Discharging Nor into the environment can also affect microbes that are important for maintaining the ecosystem [14]. The discharge also affects the microbes in the aquatic environment [15]. Improper use, un-metabolized excretion, discharge, and overuse of Nor can lead to bacterial resistance [16]. The bacterial resistance can cause the available treatment options to be ineffective [17]. As a result, patients may need more expensive antibiotics with severe side effects and need more care [18].

The one who is prescribed Nor can have a beverage with caffeine sources like tea or coffee. Comparably, drug-drug interaction [19], food-drug interaction may affect the availability of Cpro or Nor [20]. Caffeine (Caff.) is a naturally occurring methylxanthine alkaloid compound. It stimulates the cardiovascular and central nervous systems [21]. Tea leaves, coffee beans, and cocoa beans are some of the common sources of caffeine [22]. 80% of the population of the entire world consumes caffeine daily[23]. To monitor the concentration of Cpro and Nor in different samples, analytical techniques with having high sensitivity, selectivity, and low detection limit is required.

### 1.1.1. Detection Methods

Fluoroquinolones, including Cpro and Nor have been identified and quantified using analytical techniques like HPLC, HPTLC, HPLC-FLD, HPLC-MS, UPLC-MS, LC-MS/MS, and UV-Vis spectroscopy [24-28]. Cpro has been determined using different analytical techniques such as HPLC, UV-Vis spectroscopy, and electrochemical methods of analysis [29-31]. Nor has been also determined using different analytical methods, such as spectroscopic and chromatographic analytical techniques like, HPLC [32], UV-Vis spectroscopy [33], and different electrochemical methods of analysis in different samples [34]. Similarly, caffeine has been determined using the HPLC-UV method [35, 36], UV-Vis spectroscopy [37], FTIR [38], flow injection-FTIR [39], and the electrochemical method of analysis [21].

### 1.1.2. Electrochemical Methods

Due to their multiple features, including their short analytical times, simplicity, high selectivity, low instrumentation cost, flexibility, relative environmental friendliness [40], minimal use of chemical solvents, simple sample preparation, and high sensitivity, makes electrochemical techniques best choice for the identification and quantification of fluoroquinolones in different sample matrices [41, 42]. In electrochemical approaches, voltammetric-based techniques provide a quick, uncomplicated qualitative and quantitative investigation with a very low detection limits [43-45]. The other advantage of electrochemistry is that it allows for the measurement of multiple oxidation states of an element in a solution[46]. In electrochemical methods of analysis, the working electrode is the main factor that determines the result of the experiment since the redox reaction of interest is carried out on its surface[47].

Due to their low cost, wide potential window, low electrical resistivity, adaptability in chemical modification, high conductivity, ability to undergo surface modification, and their chemical inertness, carbon-based electrodes, including glassy carbon electrode, pencil graphite electrode, and carbon paste electrodes [48], are among the most often used electrodes in electroanalytical procedures [49, 50]. The glassy carbon electrode

showed chemical stability, high temperature resistance, high hardness, and minimal charge transfer resistance advantages. However, the glassy carbon electrode is far more expensive than PGE [51]. Thus, using PGE is preferable due to its relatively low cost, user-friendliness, the smallest or no time required for surface cleaning between measurements, and ease of disposal compared to other carbon-based sensors used for quantifying analytes in real samples [52], [53, 54].

A electrodes (chemical sensors) are a measurement devices that translates the physical or chemical properties of a particular analyte into a quantifiable signal that is proportional to the analyte concentration by translating the response into an analytical electrical signal [55]. Transducers are responsible for taking the chemical information of the interaction between the receptor and analyte and converting it into corresponding electrical information[56]. This information is subsequently transferred to a computer or a mechanical component[57].

Modification of the surface of electrodes, provide good reproducibility, increased sensitivity, improved selectivity, a larger usable potential window, enhances electrocatalytic properties, provides a larger surface area, increased stability, and increased conductivity [58, 59]. In electrochemical methods' of analysis, the primary objective is to enhance the electrodes' analytical performances through surface modification and the potential for a catalytic response[60]. Excellent electron transfer kinetics, improved over redox potential, higher selectivity and sensitivity, electrode surface stability during electrochemical measurement, and better usable potential windows are all characteristics of chemically modified electrodes[61].

During electrode modification, the substance can be retained on the surface of electrodes through chemisorption or covalent bonding. Electrostatic deposition of polymers containing electrochemically active groups on the electrode surface is also possible[62]. Depending on whether oxidation or reduction is the first step, molecules with non-bonding electrons, or π-electrons, under go through electropolymerization and produce radical cations or anions respectively. A small amount of adsorption onto the electrode

surface occurs prior to electropolymerizations [63]. At the electrode surface, these radical species pair and proceed through redox reactions to form the thin film. Conductively formed thin film on the electrode's surface mediates charge transfer at the film-solution interface [64].

Electrochemical sensors have been developed from many compounds, such as conducting organic polymers, metal-based nanomaterials, carbon-based nanoparticles, and transition metal complexes. Metal complexes and compounds containing redox-active ligands have been extensively used in electrochemical catalytic applications. The combinations of redox-active ligands with transition metal ions as complex compounds have the capability of multi-electron facilitation. Redox-active ligand-based complexes can either supply or accept electrons in catalytic processes; thus, they increase reactivity in both chemical and electrochemical applications[65]. Complex compounds containing transition metals with bi-dentate or poly-dentate ligands with multiple π-bonds are rich in electron density and can be perfectly suitable for electron mediator applications[66]. The coordination environment in complex compounds enables the adsorption of specific analytes, thereby increasing the system's selectivity. Therefore, the presence of variable oxidation state, the presence of high density of electrons, and the ability to adsorb analytes on its' surface makes transition metal complexes more attractive for the modification of electrochemical sensors. In addition, coordination compounds can be synthesized easily in the lab, and they are cost-effective[67].

## 1.2. Statement of the Problem

Fluoroquinolones are used for animal and human medicine. Due to the overuse and storage of fluoroquinolones, antimicrobial resistance has increased, posing a severe threat to human health and demanding high doses and new pharmacokinetic combinations [68-70]. Moreover, fluoroquinolones have the potential to have major negative side effects. Fluoroquinolone use is, therefore often limited to situations in which the advantages clearly outweigh the risks[71]. Therefore, studying the fluoroquinolones in the environment using highly sensitive method is necessary for safety.

In electrochemical methods of analysis, the glassy carbon electrode is far more expensive than PGE [51]. Thus, using PGE is preferable due to its relatively low cost, user-friendliness, the smallest time required for surface cleaning between each measurements, and ease of disposal compared to other carbon-based electrodes [52]. However, in unmodified bare electrodes including PGE electrode, low sensitivity, excessive over potential and electrode fouling are considered as bottlenecks [72, 73]. Therefore, we need to modify the surface of the electrodes to eliminate the effects of fouling, to increase sensitivity, to improve selectivity, to improve over redox potential, to increase the surface area and to increase conductivity by decreasing resistance using appropriate modifiers [58, 74, 75].

Recently, transition metal complex modifiers have been reported, indicating their promising potential as alternatives based on their several attractive features, such as they can provide high sensitivity, high selectivity, high electrical conductivity, and a larger surface area [76, 77]. This encouraged the researchers in the field to explore new transition metal complexes for electrode modifications.

This could be achieved by carefully identifying modifiers that would have polymerizable electroactivity, a geometry that results in a porous and large surface area over the electrode surface, consequently, high charge movements in the entire polymer with appropriate redox potentials so that it could oxidize or reduce the analytes in given samples. For this purpose, certain transition metal ion complexes could be good candidates and have been focused studies, and several reports have appeared indicating their promising efficient performances [78, 79]. Based on this manganese (II) and chrysin

complex that undertakes redox activities by switching between its +2 and +3 oxidation states of the metal center in desirable potential ranges was synthesized and applied for selected analyte investigation. Chrysin ($C_{17}H_{14}O_7$ (Chr)) is a dihydric phenol. One of its hydroxyls and ketonic oxygen are located in a manner that they cooperatively form coordinate covalent bonds with certain transition metal ions, forming a kinetically stable six-membered ring.

In this work, poly $[Mn(Chr)_3]Cl_2$/PGE for the determination of Cpro, poly$[Cu(Chr)_2Cl]Cl$/PGE for the determination of Nor, and poly$[Cu(Reso)_3Cl]$/PGE for the determination of Nor and Caff simultaneously have been fabricated and applied. Then the results were validated using UV-Vis spectroscopic method analysis.

## 1.3. Objective

### 1.3.1. General Objective:

- The general objective of this study was to fabricate and apply complex based polymers modified pencil graphite electrodes for electrochemical determination of Ciprofloxacin, Norfloxacin, and (Norfloxacin and Caffeine simultaneously) in pharmaceuticals, urine samples, and milk samples

### 1.3.2. Specific Objective:

- ✓ To synthesis and characterize $[Mn(Chr)_3]Cl_2$, $[Cu(Chr)_2Cl]Cl$ and $(Na_2[Cu(Reso)_3Cl])$ metal complexes
- ✓ To modify the pencil graphite electrodes as complex-based polymers modified pencil graphite electrode
- ✓ To evaluate the surface and electrochemical properties of the bare and modified electrodes
- ✓ To optimize crucial experimental parameters influencing sensor performance, including working potential window, number of scan cycles, pH, accumulation time, accumulation potential, step potential, amplitude, and frequency
- ✓ To evaluate the analytical performance of the developed sensors for the determination of Ciprofloxacin, Norfloxacin, and (Norfloxacin and Caffeine simultaneously) in pharmaceuticals, urine samples, and milk samples
- ✓ To validate the accuracy and reliability of the developed electrochemical methods by performing comparative analyses with standard UV-Vis spectrophotometric methods using statistical significance tests

## 1.4. Significance

This study makes a significant contribution to the development of cost-effective, sensitive, and selective electrochemical sensing platforms for the detection of fluoroquinolone antibiotics in complex matrices. The use of pencil graphite electrodes (PGEs), which are inexpensive, readily available, and disposable, offers a practical alternative to conventional electrodes such as glassy carbon electrodes. This is particularly important for resource-limited settings and developing countries, where access to expensive electrodes is often restricted.

The incorporation of complex-based polymer modifiers synthesized from transition metalligand systems (Mnchrysin, Cuchrysin, and Curesorcinol) introduces a novel approach to enhancing the electrochemical performance of PGEs. These modifiers improve sensitivity, selectivity, and surface properties, enabling reliable detection of ciprofloxacin, norfloxacin, and their simultaneous determination with caffeine, even in the presence of potential interfering species. This contributes to the advancement of functional electrode materials in electrochemical sensor design.

From an analytical perspective, the developed methods (SWV and AdSSWV) demonstrate satisfactory detection limits, wide linear dynamic ranges, and acceptable recovery values in pharmaceutical formulations, milk, and urine samples. These results highlight the method's applicability for real-sample analysis, making it suitable for routine quality control in pharmaceutical industries as well as for clinical and environmental monitoring.

In addition, this work provides a scientific foundation for future research in the design of polymer-modified electrodes and electrochemical sensing technologies. The synthesis strategy, electrode fabrication approach, and analytical methodology can be adapted and extended to other pharmaceutical compounds and contaminants of emerging concern. Overall, the developed sensor platform combines affordability, simplicity, and analytical performance, making it a promising candidate for decentralized and on-site monitoring applications.

## 1.5. Scope

In this work, a modified pencil graphite electrodes were prepared using synthesized metal based complexes and characterized using different characterization techniques. Some of the characterization techniques used were CV, FT-IR, UV-Vis, EIS, ICP-OES, Digital optical microscopy, Drop shape analyzer, and Cyclic voltammetry was applied in many ways throughout this work. Some of the activities conducted using CV includes modifying the electrode and characterizing the modified electrode using CV and EIS techniques. FT-IR spectroscopy was used to show the change in functional groups of the ligand and monomer modifier after complex synthesis. Finally, the modified and characterized pencil graphite electrode was applied to the determination of selected fluoroquinolones in pharmaceutical formulations, and biological samples.

# 2. CHAPTER TWO: LITERATURE REVIEW

## 2.1. Antibiotics

Drugs called antibiotics are used to treat or prevent some bacterial infections because they inhibit the growth of microorganisms. They work by killing bacteria or preventing them from spreading. Antibiotics have many applications, especially in the treatment of certain tumors, the control of plant diseases, and as animal growth promoters [80]. Antibiotics are readily available and have a wide range of brand names like Beta-lactam and fluoroquinolones are an examples of an antibiotics [81].

## 2.2. Fluoroquinolones

The fluoroquinolones are a series of systemic, broad-spectrum antibiotics that have been successfully used to treat urinary and respiratory tract infections. A wide variety of aerobic, gram-positive, and gram-negative microorganisms are susceptible to fluoroquinolone activity [71, 82]. Currently, ciprofloxacin, gemifloxacin, levofloxacin, moxifloxacin, norfloxacin, and ofloxacin are among the fluoroquinolones that are offered in many parts of the world [83].

The type II DNA topoisomerases and gyrases, which are necessary for the production of bacterial mRNAs transcription and DNA replication, are thought to be the mechanism through which fluoroquinolones work. They exhibit minimal inhibition of host and human enzymes and have a very good safety record [7, 11, 84].

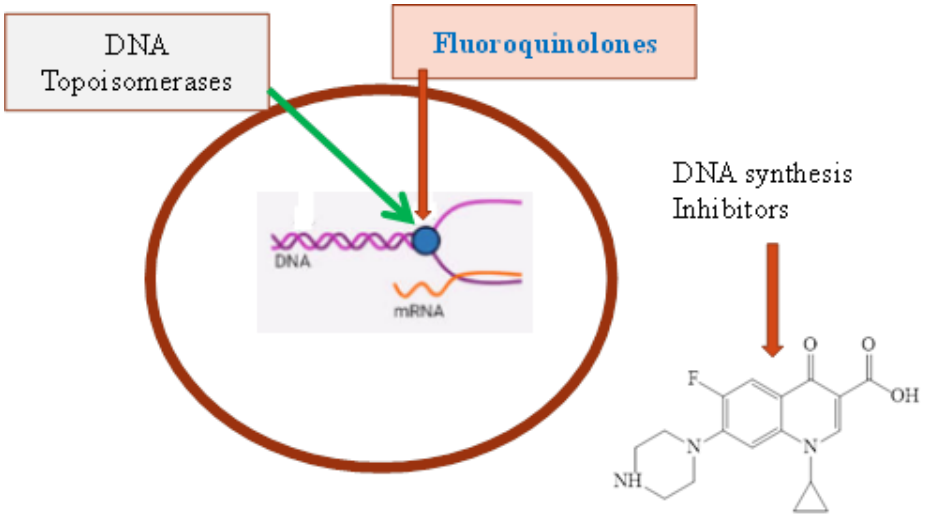


Fig. 2. 1: mechanism of fluoroquinolones

Although fluoroquinolones are generally accepted as one of the antibiotics of choice, because of their availability and widespread use in many areas of the world, growing resistance to this class of antibiotics poses a significant challenge to their usefulness [69, 85].

### 2.3. Drug-Drug interaction

A drug-drug interaction is happen when one drug is altered by the co-administered drug [86]. The effect can may enhance activities, reduce activities, and/or increase the side effect activities of the other drug. The drug-drug interaction is dependent on the patient regarding age, disease, and individual's background [87].

### 2.4. Drug-Food interaction

Drug-food interactions may arise due to misuse or due to lack of knowledge about the active ingredient in the food. The drug-food interaction may reduce or increase the effect of the drug. Some of the known examples to undergo interactions are herbs, alcohols, and fruits may cause failure of the therapy. The bioavailability of the drug can be reduced due to food induced interaction that can be directly related to the clinical effects of the drug [20]. In most cases it is difficult to determine the effects of food on a particular drug, some of the effects are components in food may form chelate and the food may alter the gastric pH [88].

### 2.5. Methods of Detection and Quantification of Fluoroquinolones

Numerous chromatographic, spectroscopic, and mass spectrometric parameters were employed, including gas chromatography-mass spectrophotometry, chromatography-tandem mass spectrophotometry, high-performance liquid chromatography (HPLC), UV-VIS spectrophotometry, and the LC-MS/MS techniques [89-91].

For instance, Elgendy, K., et al. in 2023 used C18, 150 mm × 4.6 mm, 5 μm particle size and flow rate of 1.2 mL /min at a wave-length of 280 nm to perform research on "Rapid HPLC determination of ciprofloxacin, ofloxacin, and marbofloxacin alone or in a mixture"[29]. For the study "Determination of Fluoroquinolones in Pharmaceutical Formulations by Extractive Spectrophotometric Methods Using Ion-Pair Complex

Formation with Bromothymol Blue," Nguyen, T.D., et al. (2018) used UV-Vis spectroscopy and determined the LODs for CFX, LFX, and OFX to be 0.084 g/mL, 0.101 g/mL, and 0.105 g/mL, respectively [92]. In 2011, Xu, H., et al. also studied the analysis of fluoroquinolones in animal feed using LC-MS-MS microwave-assisted extraction, and they were able to detect fluoroquinolones with a limit of detection of 5.0–9.1 ng/g [93].

The need of particular chromophoric reagents to create colored complexes and the requirement for a large sample volume for analysis are the main drawbacks of the spectrophotometric approach. Some of them involve very expensive techniques, significant amounts of reagents, and laborious, time-consuming analysis procedures[92].

### 2.6. Electroanalytical Methods of Detection

With its great selectivity, simplicity, good stability, speed, low cost, straightforward instrumentation, and sensitive detection, the electrochemical method is the best solution for the detection of fluoroquinolone antibiotic residues [94]. These techniques also have incredibly low determination and detection limits. Pesticides, drugs, environmental pollutants, food additives, and drug formulations have all been successfully detected using electroanalytical techniques [95, 96].

However, unmodified bare electrodes proposed low sensitivity, excessive overpotential, and electrode fouling. Therefore, we need to develop the bare electrode for sensitive and selective detection [72, 73]. In recent years, gold nanoparticles, carbon nanomaterials, nanocomposites, and metal complexes have all been widely used in electrochemical sensor applications [97-99].

A wide variety of electroanalytical techniques that are currently employed in electrochemical sensor and biosensors are amperometric, voltammetric, potentiometric, conductometric, and impedimetric [97].

### 2.7. Voltammetric Techniques

Voltammetry is one of the important fields of study in electroanalytical chemistry and has been used for a long time. The current is measured using voltammetric techniques as a function of the applied potential. The most commonly used voltammetric techniques include linear sweep voltammetry (LSV), cyclic voltammetry (CV), differential pulse

voltammetry (DPV), and square wave voltammetry (SWV) in the design of electrochemical sensors. Although the principle is the same for all the techniques, they differ in the way that the potential region is scanned. Based on the scanning method, the most sensitive are DPV and SWV [100, 101]. The peak current of analyte in square wave voltammetry is dependent on several instrumental parameters, including pulse amplitude, frequency, and step potential [102].

## 2.8. Electrochemical Sensor

Chemical sensors are tools that transform the physical or chemical characteristics of an analyte, such as its concentration, activity, and partial pressure, into a quantifiable, analytically meaningful signal that is proportionate to the analyte's concentration. It interacts with many chemical elements and provides valuable data [103]. If the signal is an electrical signal, it is called an electrochemical sensor. Depending on the nature of the electrical signal, electrochemical sensors can be classified as potentiometric, amperometric, and conductimetric sensors [103]. Chemical sensors are the most active and useful form of modern sensor technology due to their many good characteristics, including small size, adequate sensitivity, a larger dynamic range, and an inexpensive cost [104].

A chemical sensor or electrode can be further classified based on their reactivity as an inert or reactive electrode. Reactive electrodes actively participate in the chemical reaction. An inert electrode is a type of electrode that does not participate in a chemical reaction. Some commonly used inert electrodes include pt, Au, and carbon-based electrodes. Electrodes can also be classified as anode and cathode based on the types of reactions on the surface of the electrode [105].

Three electrode systems consist of a working electrode, a reference electrode, and a counter electrode. Various working electrodes, such as glassy carbon electrodes, mercury electrodes, carbon paste electrodes, single or multiwall carbon nanotube, carbon paste electrodes, screen-printed electrodes, indium tin oxide glass electrodes, boron-doped diamond electrodes, gold, etc., have been used in voltammetric techniques for qualitative and quantitative determinations of analytes [106, 107].

Calomel and silver-silver chloride electrodes are the two primary reference electrodes used in electrochemical analysis. The calomel reference electrode contains mercury and mercury chloride compounds. The liquid mercury element and a solid paste of $Hg_2Cl_2$ are connected to a rod covered in a saturated KCl solution. Silver-silver chloride is produced by the reaction of silver cable and the precipitated salt of AgCl placed in a tube of AgCl and KCl solution. This enables ions to be formed as electrons move in and out of the electrode system [108, 109].

## 2.9. Electrode Modifications

All electrochemical sensing techniques are based on electrochemical processes that occur at the electrode surface. When utilizing electrochemical sensors to determine electroactive analytes, the overpotential and low anodic or cathodic current responses are considered as bottlenecks. It's interesting to note that modifying the electrodes with different conductive materials can be easily resolved. Therefore, electrode surface modification plays a crucial role in electrochemical sensor development. A modified electrode is a conducting or semiconducting material that has been coated with a monomolecular, multimolecular, ionic, or polymeric film. In electroanalysis, CMEs show improved over redox potentials, quick electron transfer kinetics, good electro-optical characteristics, and stable electrode surfaces. The other advantage of modifying the electrode is to increase the surface area and increase conductivity by decreasing resistance [58, 74, 75].

## 2.10. Electrochemical Modifiers

Electrochemical sensors have been developed from many compounds. Some of them are conducting organic polymers, metal-based nanomaterials, carbon-based nanoparticles, and transition metal complexes are among the commonly reported electrode-modifier materials that are deposited on the surface of the electrode by potentiostatic electropolymerization, and casting techniques [110].The modifier is attached to the surface of the electrode either by covalent bonding, chemisorption, or adsorption [111]. The application of modifier material is dependent on the charge-transferring properties of the modifier immobilized on the surface of the electrode [97].

## 2.11. Complex Compounds

Transition metals are well recognized for their ability to form complex ions because of their partially filled d-orbitals. When electron-rich species known as ligands surround positive metal ions and donate two electrons to transition element, complexes compounds are created. Numerous characteristics are displayed by these complexes, such as color, magnetism, a high melting point, strong electrical and thermal conductivity, and catalytic activity. In addition to their vertical commonalities, the transition metals show notable similarities in their chemistry on the horizontal plane[112].

The occurrence of numerous oxidation states is a defining characteristic of transition metals. Many transition metals can function as catalysts because of their multiple oxidation states, which enable them to lose and gain electrons in different stages of a reaction before ultimately re-forming their original ion. Many transition metals are good adsorbents. This implies that molecules in reaction can easily stick to their surface. Adsorption results in some kind of contact, such as a weakening of the bonds between the reactant molecules and the transition metal surface. This makes it possible for the response to occur. The two above-mentioned basics contribute to lowering the activation energy of the reaction and raising its rate of reaction[113, 114].

Ligands give electron pairs to transition metal ions while functioning as Lewis bases. Ligands can be uni-dentate, bi-dentate, and poly-dentate ligands. Unidentate ligands are ligands that can bind to the coordination center but only contain one binding atom. The list below contains a few examples of unidentate ligands[115].

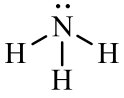
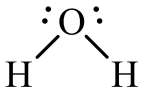
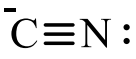
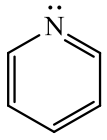

Conversely, as the illustration below illustrates, ligands that possess the capacity to attach to the central atom through two distinct donor atoms are known as bidentate ligands [116, 117].

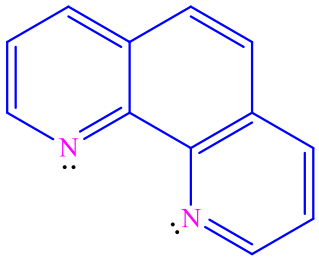

1,10- Phenanthroline

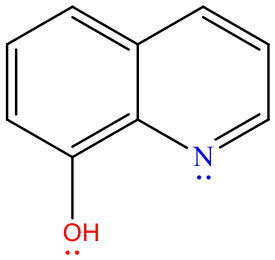

8-hydroxyl quinolone

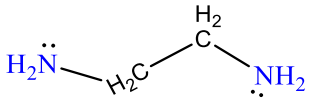

Ethylenediamine

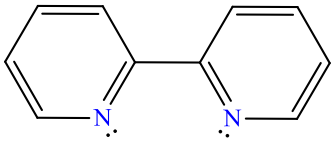

Bipyridine

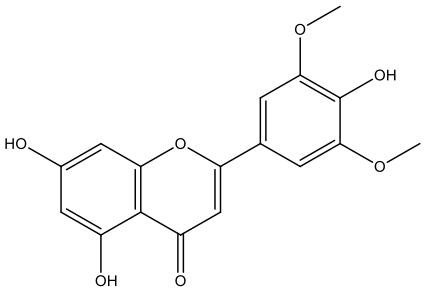

Chrysine

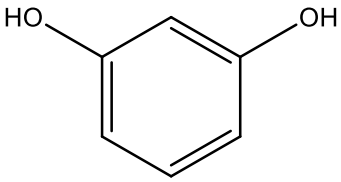

Resorcinole

Polydentate ligands are ligands with a large number of donor atoms that can bind to the coordination center. The following is an excellent illustration of polydentate ligands[118]. Because bi-dentate and poly-dentate ligands can form stable coordination complexes called chelate compounds, they are useful in a variety of applications[119].

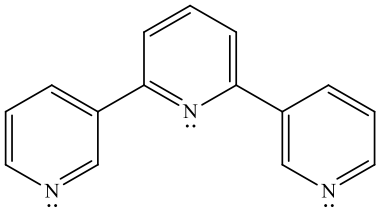

2,2,2- terpyridine

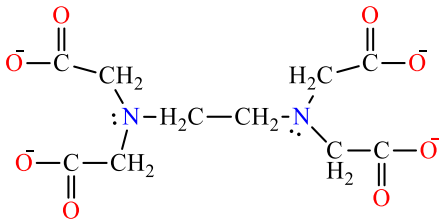

Ethylenediaminetetraacetate

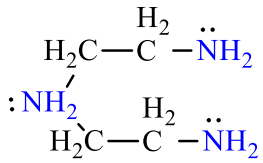

Diethyl triamine

The properties of transition metal complexes can be influenced by size and charge of the ligands, as well as the geometry of the complex [120].

**2.12. Complex Compounds as an Electrode Modifier**

The presence of metallic centers in their structure offers a redox-active behavior that is being applied in the design of solid electrodes [98]. Conductive ligands catalyze the reduction and oxidation reactions with transition metal complexes. Redox active ligand based complexes can be either supply or accept electrons in catalytic processes, thus they increase reactivity in electrochemical applications [65]. For example, Debalke, A., et al, 2022 used diaquabis(1,10-phenanthroline)copper(II)chloride complex for detection of amoxicillin in pharmaceutical and biological samples [121]. The structure of the complex used as a modifier is shown below.

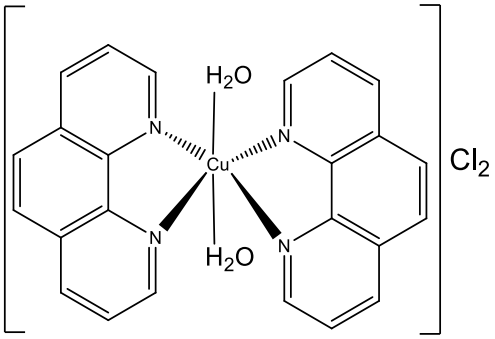


Scheme 2. 1: Chemical structural of diaquabis(1,10-phenanthroline)copper(II)chloride

This complex compound showed good electro-catalytic activities, low detection limit, wide dynamic range, and good selectivity.

Tetraruthenated porphyrin and tetramanganized porphyrin complexes have a strong electron-withdrawing effect and show electrocatilitic effects for pharmaceuticals such as

folic acid, acetaminophen, metronidazole, and tyrosine. The oxidation processes with electrochemical sensors based on those complexes do not require high oxidation potentials, and the detection limits obtained with these sensors are very low, with good sensitivities and enhanced electrocatalysts. The structure of these complexes is shown in Scheme 3 [98].

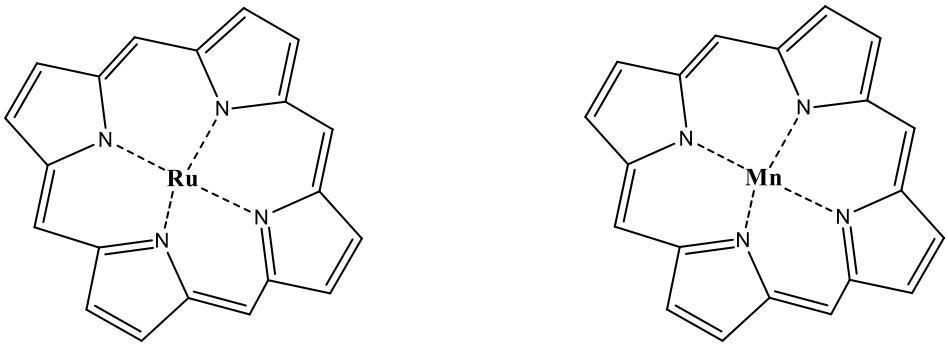


Scheme 2. 2: Molecular structure of tetraruthenated porphyrin and tetramanganied porphyrin

Chanie, G., et al, 2024 have studied the detection of tinidazole using a complex compound bis(2,2′-bipyridine)diresorcinolateruthenium(III) chloride as shown in scheme 4. The electroactivity of this modifier shows enhanced surface area, four folds current enhancement, wider linear dynamic range, excellent performance, lower LoD. They also conclude using this modifier is simple step electrode modification, relatively chip, and easily available**[122]**

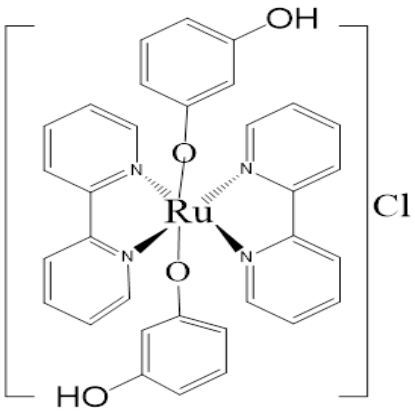


Scheme 2. 3: bis(2,2-bipyridine)diresorcinolateruthenium(III)chloride

Kassa, A., et al. (2023) determined chloroquine phosphate in real samples using a diresorcinolatebis(1,10-phenanthroline)cobalt (II) by modifying a glassy carbon electrode. The structure of this modifier is shown in Scheme 2.4. As we can see, the modifier used here is a complex compound with heteroleptic ligands called resorcinolate, 1,10-phenanthroline, and the transition metal cobalt (II). This modifier for the determination of chloroquine shows good current enhancement and is highly selective in the presence of amoxicillin, ciprofloxacillin, and paracetamol. They come up with a LoD of 0.39 nM and a linear range of 0.005–300 µM.[123].

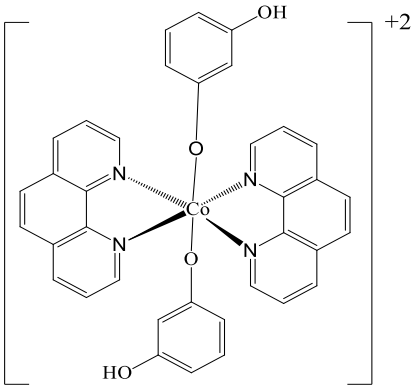


Scheme 2. 4:diresorcinolatebis(1,10-phenanthroline)cobalt(II)

### 2.13. Electrode Modification Techniques

The CME is conducted utilizing a variety of techniques, including electropolymerization, drop casing, dip coating, and spin coating from monomers [62]. A modified electrode can be used both for potentiometric and amperometric ion sensors.

#### 2.13.1. Drop Casting

Drop casting is a simple film-forming technique that does not require specific equipment. The drop of liquid containing the necessary material is deposited on a substrate without over-spillage, followed by the evaporation of the solvent. However, it is challenging to obtain a consistent layer and control its thickness. The film thickness depends on the volume of dispersion used and the particle concentration, both of which can be easily varied. Other variables that affect the film structure are the rate of evaporation and the drying process. For this approach, volatile liquids are typically preferred. The main

distinction between this approach and spin coating is that no substrate spinning is necessary [124].

### 2.13.2. Spine Coating

In comparison to drop-casting, spin-coating frequently results in more uniform film thicknesses over the substrate, and with the right equipment, it can handle considerably larger substrates. In this method, a volume of material with a known particle concentration is delivered into the middle of a substrate while it is being spun at a high RPM. The dispersion is uniformly dispersed across the substrate by centrifugal force, and the solvent is then evaporated to produce a thin particle film. The volume, rotating speed, and dispersion concentration all affect film thickness [125, 126].

### 2.13.3. Electrodeposition

Electrodeposition is a plating process in which ions in a solution migrate under the influence of an electric field and are deposited onto an electrode using a redox reaction. A thin, uniform coating is produced on the surface of the electrode when it is submerged in a solution containing a salt of the metal to be deposited by running a current through an electrochemical cell. Depending on the reaction mechanism, the procedure can be anodic electrodeposition or cathodic electrodeposition and involves electron transfer and phase change [127].

### 2.13.4. Electropolymerization

One of the most successful ways of forming redox polymers on the electrode surface is electropolymerization using cyclic voltammetry. Electropolymerization allows film thickness to be reproduced and monitored after numerous scans and layers. Films with many layers have more electroactive spots [128].

Prior to electropolymerization operations, a little amount of material is adsorbed onto the electrode surface. A monomer must have functional groups that can be reduced or oxidized using non-bonding electrons on the heteroatom or molecular orbitals in order for

it to be electropolymerized on an electrode surface. Depending on whether the initial step is oxidation or reduction, the organic molecule produces a radical cation or anion. These radical species couple at the electrode surface and proceed through redox reactions to create the thin film. Multifunctional groups on the monomer initiating polymerization reactions encourage the right orientations for the incorporation of monomer units into the growing polymer film. The modifier's lattice orientation and film thickness have an impact on the analyte's electrochemical reactivity [129, 130].

## 2.14. Characterization Methods of Modified Electrodes

Numerous electrochemical and spectroscopic methods have been used to characterize chemically modified electrodes. Techniques like CV, EIS, FTIR, and digital optical microscopy are among them.

### 2.14.1. Cyclic Voltammetry (CV)

Using $[Fe(CN)_6]^{3-/4-}$ as a probe, KCl as a supporting electrolyte, and pH 7.0, the modified and bare electrodes' voltammograms are produced and compared in order to characterize the modified electrode using CV. Five points should be taken into account while comparing CV values. These include peak current, peak current ratio, peak shape, peak-to-peak potential separation, and effective surface area. Peak-peak potential separation of the modified electrode should be less than that of the bare electrode, and current and effective surface area should be increased. Sharp redox peaks for the modified electrode indicate the modifier's catalytic property toward the probe, and the electrode has been modified [131, 132].

Cyclic voltammograms of $[Fe(CN)_6]^{3-/4-}$ at both the unmodified and modified electrodes are recorded at various scan rates to examine the impact of surface modification on the electrode surface area. In the Randles-Sevcik equation Eq, the active surface area for both electrodes is determined from the slope value of the plot of Ipa vs. $v^{1/2}$ [133].

$$Ip = 2.69 \times 10^5 n^{3/2} A D^{1/2} v^{1/2} C_o$$

If the effective surface area of the modified electrode exhibits enhancement in comparison to the effective surface area of the unmodified electrode, the electrode surface is modified by a modifier to improve the effective surface area. The increased

peak current for the probe can therefore be attributed to the modified electrode's higher active surface area [133]. kokab, T., et al conducted a research on tripeptide derivative-modified glassy carbon electrode for the detection of $Cd^{2+}$ Ions and characterize the modified electrode using CV. They compare the voltammograms of bare and the modified electrode as shown in the following figure 2.2 which illustrates a few of the points discussed above [134]:

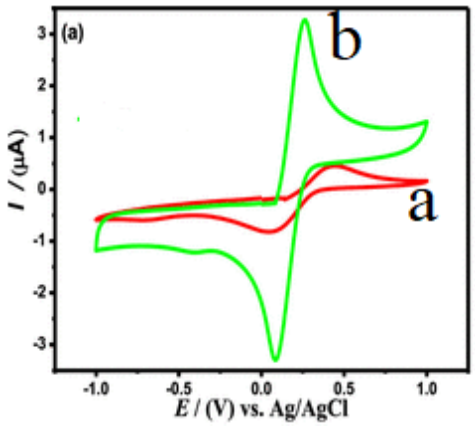


Fig. 2. 2: CVs of (a) bare, (b) modified in pH 7.0 PBS containing 5.0 mM $[Fe(CN)_6]^{3-/4-}$ and 0.1 M KCl at a scan rate of 100 mV $s^{-1}$

### 2.14.2. Electrochemical Impedance Spectroscopy (EIS)

The electrochemical impedance spectroscopic (EIS) technique is used as a tool to characterize the surface of the electrode and to investigate the conductivity of the electrode surface. Charge transfer activities at the electrode-solution interface, diffusion mass transport processes, and ionic transport have all been studied using EIS. The total impedance is the combination of resistors, capacitors, and inductors. Films characterized with EIS ideally show charge transfer resistance (Rct), which is given by a semicircle in Nyquist plots, and the semicircle intersects the real-Z' axis at high frequencies. At lower frequencies, when time is allowed for diffusion effects to be realized, Warburg impedance dominates the charge transfer process [135, 136].

Kassa, A. and M. Amare, have conducted a research on Highly selective and sensitive differential pulse voltammetric method based on poly (Alizarin)/GCE for determination

of cefadroxil in tablet and human urine samples and characterize the modified electrode using EIS as shown in fig. 2.3 below. Nyquist plots of the bare electrode (curve a) and modified electrode (curve b) in pH 7.0 PBS containing [Fe (CN) $_6$] $^{3-/4-}$ as a probe, were used to characterize the modified electrode using EIS. As shown, both the bare and modified electrodes show a semicircle of different diameter at the high frequency region and a line at about 45$^o$ at the low frequency region. The line at about 45$^o$ is attributed to diffusion of the probe from the bulk solution towards the electrode-solution interface. In contrast to the unmodified electrode, the modified electrode possessed a semi-circle with a very small diameter that showed the surface of the electrode was modified with an electroactive modifier that improved the conductivity of the electrode surface [137].

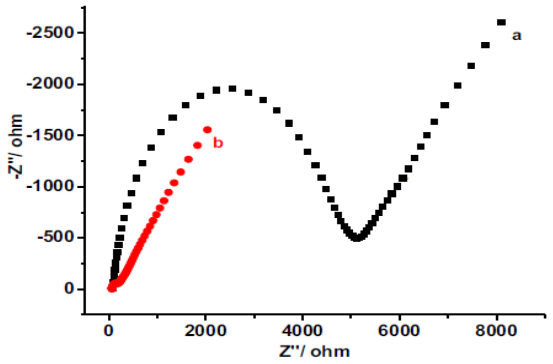


Fig. 2. 3: bare (a) and modified (b) in pH 7.0 PBS containing [Fe (CN) $_6$] $^{3-/4-}$, and 0.1 M KCl

### 2.14.3. Contact angle analyzer

Contact angel is the measure of the angle formed between liquids and solid materials. The act of spreading of a liquid over solid materials is known as wettability. The magnitude of the angle formed and wettability depends on the attraction forces like cohesion and adhesion forces [138]. In water contact angle measurements, if the value is below 90$^o$ then the solid material is considered as hydrophilic properties where as if the contact angle value is greater than 90$^o$ then the material has hydrophobic properties. As the surface chemistry changes the value of the contact angle will also changes [139].

### 2.14.4. Digital optical microscopy

Digital optical microscopy is defined as the process of imaging at high efficiency and accuracy generated through a microscope and conducts a computerized analysis primarily for clinical diagnosis [140]. The whole imaging process, image acquisition, sampling processing and data storage can be controlled via a computer. Digital optical microscopy is the extension of conventional microscopy. In this method true color information can be acquired that cannot be obtained by an electron microscope [141].

# 3. CHAPTER THREE: EXPERIMENTAL PART

## 3.1. Chemicals and Instruments

Selected fluoroquinolone pharmaceuticals were obtained from pharmaceutical shops based on their availability. $NaH_2PO_4$ and $Na_2HPO_4$ (98%, Blulux laboratories (p) Ltd), sulfuric acid (98% Loba Chemie, laboratory reagent), phosphate buffer solution (PBS), $CH_3COOH$ and $CH_3COONa$, $H_3PO_4$, $CH_3COOH$, $H_3BO_3$, Sodium hydroxide (NaOH)(Extra pure, Lab Tech Chemicals), hydrochloric acid/HCl (37 %, Fisher Scientific), Potassium hexacyanoferrate(III) and potassium hexacyanoferrate(II) (98.0%, BDH laboratories supplies, England), potassium chloride (99.5%, Blulux laboratories (p) Ltd), Sulfuric acid/$H_2SO_4$ (98% Loba Chemie, laboratory reagent), hydrated Manganese (II) chloride, Ciprofloxacin chloride, Chrysin ligand, Copper (II) chloride, resorcinol as a ligand, Norfluoxacine (99.0 %, Sigma-Aldrich) standard, and Caffeine (99%, Loba Chemi, Laboratory reagent) were used. All chemicals and reagents utilized in this investigation were analytical grade, and all solutions were prepared with double-distilled water throughout all experiments.

Some of the instruments used in this work were CH Instruments 760E potentiostat (Austin, Texas, USA), potentiostat/impedance analyzer (PalmSens4, Netherland), Deionizer (Evoqua Water Technologies, Germany), pH meter (AD8000, Adwa, Romania), UV-Vis spectrophotometer, ICP-OES, Fourier Transform IR Spectroscopy (FT-IR), Electronic balance (Nimbus, ADAM equipment, USA), Contact angle goniometer (DSA25 Drop Shape Analyzer, Krüss, Germany), Digital Optical Microscope (Andonstar, 246s, 249s), centrifuge (1020D, Centurion scientific LTD, UK), Mortar and pestle, Refrigerator, and a centrifuge were some of the device used in this work.

## 3.2. Preparation of Stock Solution and Working Solution

A stock solution of selected fluoroquinolones was prepared by dissolving an accurately measured amount of each fluoroquinolone in a suitable solvent and diluting it with an appropriate amount of a proper buffer solution with an optimum pH to obtain fluoroquinolone standard solutions in the working concentration range [142]. In this way, using 50 mL of a volumetric flask, 91.96 mg of Cpro chloride was dissolved in deionized

water to prepare a stock solution (5.0 mM) of Cpro. The working solutions were prepared from the stock solution using dilution law and serial dilution with 0.1 M ABS. 48.55 mg of Caff and 79.83 mg of Nor were dissolved in deionized water to prepare a stock solution (5.0 mM) of Nor and Caff in 50 mL separately. The working solutions were prepared from the stock solutions using the dilution law and serial dilution with 0.1 M PBS.

### 3.3. Preparation of Real Samples

A two available Cpro tablets were purchased from local drug stores in Bahir Dar city, Ethiopia. Five weighed Cpro tablets from each of the two tablet brands, including Scott-Edil Pharmacia Ltd., (Ciproscot), and Zindolin Remedica Ltd. (Zindolin), with an average tablet mass of 726.26 and 793.62 mg/tablet, respectively, were ground and homogenized using a mortar and pestle. Stock solutions (5.0 mM) of the tablet were prepared by dissolving (120.33 and 131.48 mg of Ciproscot and Zindolin, respectively) tablet powder into a 50 mL volumetric flask and filling up to the mark with deionized water. Working solutions of Cpro were further prepared from stock solutions of each brand in pH 7.5 ABS. The stock and a working solution with the required theoretical concentration were made and kept in a refrigerator at 4 ºc until analysis. Tablet samples of nominal concentration were spiked with various concentrations of standard solutions of analytes for spike and interference recovery analysis [142].

Two available Nor tablet brands were purchased from local drug stores in Bahir Dar city, Ethiopia. Five weighed Nor tablets from each of the two tablet brands, including Medochemie Ltd. Cyprus/Europe (Gyrablock) and Humanwell pharmaceutical Ethiopia PLC (Nofxin), with an average tablet mass of 525.3 and 603.6 mg/tablet, respectively, were grounded and homogenized using a mortar and pestle. Stock solutions of 5.0 mM of the tablet were prepared by dissolving 104.8 and 120.5 mg of Gyrablock and Nofxin, respectively [143]. The average tablet mass and amount of Nor per tablet marked were used for the calculation of the required mass in the preparation of nominal tablet stock solution. Working solutions of Nor were further prepared from stock solutions of each brand and the spiked solutions were prepared by mixing the required amount from stock solutions of tablet and stock solutions from standard before dilution in pH 5.5 PBS and using pH 6.0 PBS.

Urine samples were obtained ready to use from Felege Hiwot referral hospital at Bahir Dar City, which follows best practices in volunteer sample collection. The total samples obtained were centrifuged at 4000 RPM for 10.0 min. A 1.0 mL urine sample was transferred to a 25-mL volumetric flask, filled to the mark with pH 7.5 ABS. Urine samples were spiked with various concentrations of standard solutions for recovery analysis, following the same techniques as the tablet samples [144]. Similarly, a 1.0 mL urine sample was transferred to a 25 mL volumetric flask, filled to the mark with pH 6.0 PBS for the determination of Nor and Caff in the urine sample simultaneously. For a recovery analysis, known concentration of Nor and Caff was added in to a 1.0 mL urine sample in a 25 mL volumetric flask. All the prepared solutions were stored in refrigeration for further analysis.

Raw milk samples were purchased from the local market of Bahir Dar City. 5 mL of Acetonitrile was added to 50 mL of the raw milk sample to coagulate the fat and protein in the sample. The mixture was centrifuged at 4000 rpm for 20 min and filtered via Whatman filter paper. A 1.0 mL supernatant milk sample was transferred to a 25 mL volumetric flask and filled with pH 5.5 PBS for Nor analysis[144]. Likewise, 1.0 mL processed milk sample before dilution was mixed with the calculated amount of standard solution in 25 mL volumetric flask and diluted with pH 5.5 PBS for spike analysis.

### 3.4. Spectrophotometric Measurements

The measurement was conducted by measuring the blank solution and making it out of zero, flowed by measuring the spectra of Cpro in the standard solution and sample solution in the wavelength range of 200-500 nm and 1 cm optical path length quartz cuvette [145]. The blank used in this experiment was pH 7.5 (ABS) acetate buffer solutions. All measurements are conducted at room temperature.

### 3.5. Synthesis and Characterization of Modifiers

Transition metal-based complexes, which were used for the modification of the electrodes, were synthesized in three or two steps [2]. The synthesized complex compounds were characterized using physicochemical parameters, UV-Vis, and FT-IR techniques. The electronic spectra of the ligand and complexes were presented. The

disappearance and appearance of their characteristic bands have been examined. FT-IR was used to examine the appearance and/or disappearance of functional groups in the synthesized complexes compared to the ligands [2, 113, 146].

### 3.5.1. Synthesis of $[Mn(Chr)_3]Cl_2$

To a solution of MnCl2• 4H2O (1.5 mmol) in 40 mL of hot methanol, stirred in a 250 mL round-bottom reaction flask in an oil bath, Chrysin (4.5 mmol) dissolved in hot methanol was gradually added, and the mixture was allowed to continue stirring and refluxing for 3 h. A golden yellow solution was formed and allowed to cool to room temperature. The solvent was removed by rotary evaporation. A golden yellow powder was obtained and was washed three times with 10 mL methanol each and dried in open air (Yield:1.53g, 91.5%).

### 3.5.2. Synthesis of the Nucleophilic Ligand (ResoNa)

Sodium resorcinolate (ResoNa) was prepared following previous literature, with necessary adjustments [147]. NaOH solution in a 1:1 water-methanol mixture (3.6 mmol in 30 mL) was slowly added to an equal-volume aqueous solution of resorcinol (3.6 mmol in 50 mL) with stirring at room temperature. The mixture was stirred for an additional hour. The resulting yellowish solution was evaporated under reduced pressure to dryness. The brown solid that formed was dried under vacuum over $CaCl_2$, yielding 0.40 g (83.2%).

### 3.5.3. Synthesis of $Na_2[Cu(Reso)_3Cl]$

A solution of $CuCl_2 \cdot 2H_2O$ (0.5 mmol) in 20 mL of methanol was added to a methanolic solution of ResoNa (1.5 mmol) in 40 mL of methanol containing a drop of triethanolamine. The resulting mixture was stirred under reflux at 70 °C for 3 hours using an oil bath. After standing overnight and cooling to room temperature, a brown solution was obtained. The solvent was then removed under reduced pressure, and the resulting dark brown solid was washed several times with acetone and dried in air, yielding 0.20 g (83.2%) [148]. The corresponding reaction pathway is shown in Scheme 4.5.

### 3.5.4. Complex Characterization Procedures

The electrolytic conductance of 0.1 mM solution of the complex in acetonitrile was measured at room temperature. The melting point of the complex was measured by the Stuart SMP30 melting point apparatus. UV-Vis electronic spectra for a 1.0 mM solution of the ligand, salt, and complex in ethanol were recorded in the wavelength range 200–800 nm, and the FTIR spectra of approximately 1.0 mg of the complex and ligand per 200 mg KBr discs were recorded in the frequency range 4000–400 $cm^{-1}$.

10 mg of the complex was placed in a clean and dry 50 mL conical flask to which 5 mL concentrated nitric acid (15.8 M) was added, and the contents were heated gently until a few drops remained in the flask. The digestion process using nitric acid was repeated three times until all the organic portions of the complex were removed. The residue was then reconstituted into a 50 mL volumetric flask using deionized water, and the manganese and copper content was determined using ICP-OES [149].

The result confirmed that the experimental values were in very good agreement with the calculated values. This supported that the proposed structure of the complex was obtained.

Ionizable chloride content in the complex was determined thermogravimetrically by measuring the mass of AgCl precipitate obtained from the mixture of 10 mL solution of 1.0 mg of the complex in distilled water with excess $AgNO_3$ solution.

## 3.6. Electrochemical Procedures

A conventional three-electrode system was used for the electrochemical studies, with a Pt coil and Pt wire serving as the counter electrode, Ag/AgCl (3.0 M KCl) serving as the reference electrode, poly $[Mn(Chr)_3]Cl_2$/PGE, poly$[Cu(Chr)_2Cl]Cl$/PGE, and poly $[Cu(Reso)_3Cl]$/PGE or unmodified PGE serving as the working electrode [150]. Both modified and unmodified pencil working electrodes were rescanned in blank solution before each measurement until a steady voltammogram was established.

### 3.7. Modification of Working Electrodes

A measured amount of monomers of complex compounds were taken for electrode modification using electropolymerization techniques. Before electropolymerization, potential window and scan cycles were optimized using a standard solution of the analyte of interest. The electroactivity of different modifier were measured, and the more electro-active was selected as a modifier. The pencil graphite electrode was then modified using the optimized conditions and applied for the detection of analytes of interest. Freshly modified electrodes have been used in each experiment [151].

#### 3.7.1. Electrochemical Preparation of Poly $[Mn(Chr)_3]Cl_2$/PGE

The potentiodynamic electropolymerization process was used to create novel poly $[Mn(Chr)_3]Cl_2$/PGE which had not been used for electrode modification yet. 0.8 mM $[Mn(Chr)_3]Cl_2$ was electropolymerized on the PGE surface by scanning between -0.5 and +2 V for 10 cycles at a scan rate of 100 $mVs^{-1}$. The modified electrode was washed with distilled water and scanned in monomer-free 0.5 M $H_2SO_4$ between -0.8 and +0.8 V until a steady CV voltammogram was achieved [152].

#### 3.7.2. Preparation of Poly $[Cu(Chr)_2Cl]Cl$/PGE

The modified working electrode has been prepared using locally available 0.7 mm in diameter HB pencil lead rod for writing and drawing purpose. The pencil lead rod has been placed into the copper wire through rubber cup containing self-opening and sealed spring and placed inside a micropipette tip for electrical connection [153, 154]. Then the potentiodynamic electropolymerization has been used to synthesize poly $[Cu(Chr)_2Cl]Cl$/PGE. 1.0 mM $[Cu(Chr)_2Cl]Cl$ has been electropolymerized on the PGE surface by scanning between -0.4 and +1.8 V for 12 cycles at a scan rate of 100 $mVs^{-1}$[155]. The modified electrode has been washed with distilled water and scanned in monomer-free 0.5 M $H_2SO_4$ between -0.8 and +0.8 V for eight scan cycles.

### 3.7.3. Preparation of Poly [$Cu(Reso)_3Cl$]/PGE

A potentiodynamic electropolymerization was used to synthesize poly [$Cu(Reso)_3Cl$]/PGE. 1.0 mM [$Cu(Reso)_3Cl$] was electropolymerized on the PGE surface by scanning between -1.4 and +1.6 V for 10 cycles at a scan rate of 100 $mVs^{-1}$ [155, 156]. The modified electrode was washed with distilled water and scanned in monomer-free 0.5 M $H_2SO_4$ between -0.75 and +0.8 V for 6 scan cycles.

## 3.8. Modified Electrode Characterizations

The modified electrodes were characterized related to bare electrode using different characterization techniques like the electrochemical impedance spectroscopy (EIS), UV-Vis, contact angle, digital optical microscope, and cyclic voltammetry (CV). To characterize the modified electrode relative to the bare electrode, 10.0 mM $[Fe(CN)_6]^{-3/-4}$ was used as a probe and KCl as a supporting electrolyte [157]. The electrochemical behavior of Cpro at poly [$Mn(Chr)_3]Cl_2$/PGE was investigated using square wave voltammetry (SWV) and cyclic voltammetry (CV) relative to the bare electrode. The quantitative determinations of Cpro in the human urine and two brands of pharmaceutical samples were done using the SWV method of analysis [158]. The electrochemical behavior of Nor at poly [$Cu(Chr)_2Cl]Cl$/PGE and bare PGE has been investigated using adsorptive stripping square wave voltammetry (AdS-SWV) and cyclic voltammetry (CV). The quantitative determinations of Nor in milk and two brands of pharmaceutical samples were done using the AdS-SWV and UV-Vis spectrometric methods of analysis. Similarly, the electrochemical behavior of Nor and Caff simultaneously using poly [$Cu(Reso)_3Cl$]/PGE was investigated using adsorptive stripping square wave voltammetry (AdSSWV) and differential pulse voltammetry (DPV) techniques relative to the bare electrode. The quantitative determinations of Nor and Caff simultaneously in two Nor brands of pharmaceutical samples and urine samples were done using the developed AdSSWV methods of analysis.

## 3.9. Assembling of Working Pencil Graphite Electrode

A working pencil graphite electrode was prepared by first connecting copper wire with an opening and a self-tightening spring in one end [159]. The combination of copper wire and spring was placed into the micropipette tip. On the narrower side of the micropipette

tip, a plastic tube was inserted for length adjustment and to insulate the pencil [153]. A syringe rubber cup was used to seal the other side of the plastic tube tip. The center of the syringe rubber cup was penetrated with a needle, and the pencil was put into the copper wire through this opening. The spring inside the micropipette could open and connect the pencil to the copper wire. A fresh pencil lead was used for each analysis [160].

### 3.10. UV-Vis Spectroscopy Procedures

UV-Vis spectrophotometry was used to measure the analyte by scanning the wavelength from 800 nm to 200 nm. A series of standard solutions was used to calibrate the instrument. The blank solution and untreated FTO were used to remove the baseline. The sample solution and the treated FTO were then scanned over the wavelength range. The sample solution was inserted into the instrument using a quartz cuvette sample holder [161].

### 3.11. Method Validation

In order to show the validity of the proposed method, the analytical features of the method, such as linearity, limit of detection, reproducibility, repeatability, and selectivity of the developed electrode towards potential interferences, were examined. In addition, to verify the validity of the developed method for the determination of the selected fluoroquinolones in real samples, the standard addition method was applied by spiking tablet, urine, and milk samples with different concentrations of standard solutions. A percentage of recovery was calculated for real-sample analysis. Finally, the result was compared with literature values [162, 163].

# 4. CHAPTER FOUR: RESULT AND DISCUSSION

In the result and discussion part, the results obtained from the four separate works were discussed separately. These are synthesis, characterization, and application of a novel electrochemical sensor based on poly $[Mn(Chr)_3]Cl_2$/PGE for the determination of ciprofloxacin in pharmaceuticals and urine samples, comparison of methods for detecting ciprofloxacin in pharmaceuticals and urine samples: UV-Vis spectrophotometry vs. poly ($[Mn(Chr)_3]Cl_2$)/PGE voltammetry, synthesis, characterization, and application of poly $[Cu(Chr)_2Cl]Cl$/PGE based electrochemical sensor for the determination of norfloxacin in pharmaceuticals and milk samples, and Poly $[Cu(Reso)_3Cl]$/PGE based electrochemical sensor for the simultaneous determination of norfloxacin and caffeine in pharmaceuticals and urine samples.

## 4.1. Characterization, and application of a novel electrochemical sensor based on poly $[Mn(Chr)_3]Cl_2$/PGE for the Determination of Ciprofloxacin in pharmaceuticals and urine samples

### 4.1.1. Characterization of the Complex

The synthesized complex was analyzed using physicochemical techniques such as solubility, melting point determination, ionic conductivity measurements, chloride estimation, and manganese determination. It was also investigated spectroscopically using FT-IR and UV-Vis spectroscopy techniques. Observations included alterations in peak intensity and the emergence or vanishing of specific peaks, which were pivotal indicators signaling the formation of a novel complex through the synthesis process. These changes in the spectral data provided crucial evidence supporting the successful preparation of the new complex.

#### 4.1.1.1.Physico-Chemical Characterizations

The results of the studied physicochemical properties of the synthesized complex are summarized in Table 4.1. The complex demonstrates solubility in low-polarity solvents like acetonitrile and dimethylsulfoxide despite its ionic nature (Table 4.1). This solubility can be attributed to the non-polar and bulky nature of the ligand, which constitutes a

significant portion of the complex and influences its dissolution characteristics. Analysis of its thermal behavior reveals instability beyond 320°C. The complex's electrolytic conductivity confirms the presence of ionizable chloride ions outside the coordination sphere, aligning with results from chloride estimation experiments [164]. However, the observed conductivity value is lower than anticipated for a 1:2 ionic ratio as shown in Table 4.1. This discrepancy is attributed to the substantial mass and surface area of the complex's cation, factors that notably reduce the speed of ion motion within the system.

Table 4. 1: Studied physicochemical properties of $[Mn(C_{51}H_{42}O_{21}]Cl_2$

| **physical property** | **$[Mn(Chr)_3]Cl_2$** |
|---|---|
| Color | Golden yellow |
| Melting point ($^0$C) | 320 (decomposed) |
| Solubility | Soluble in $CH_3CN$, DMSO |
| Stability at room temperature | Stable |
| Conductivity (S cm$^2$ mol$^{-1}$) | 50.8 |
| Mn content, %(Calculated/Experimental) | 4.92/4.86 |
| Chloride content,%(Calculated/Experimental) | 6.35/5.99 |

The easy synthesis of the complex is attributed to the acquisition of thermodynamic (hard $Mn^{2+}$ acid with hard 'O' donor ligand) and kinetic stability due to the classic chelating bidentate ligand properties of Chr, supplemented by the formation of an octahedral geometry with six-membered rings. This is a consequence of the cooperative contributions of its ideally placed hydric phenol and carbonyl oxygen atoms, its rigid planar structure, and $\pi$-acidic properties through the carbonyl oxygen [165]. As a result of this, the electronic configuration in the *d* orbitals of the metal center is changed to $t_{2g}^5 e_g^0$ (in the complex) from $t_{2g}^3 e_g^2$ (in the salt). The composition was confirmed from gravimetric halide estimation and metal content determination using ICP-OES (Table 4.1). Furthermore, the high measured conductance of the as-synthesized complex in an aqueous solution (Table 4.1) might account for the presence of chloride as counter anions.

### 4.1.1.2. UV-Vis Characterization

The 287 nm band in the salt spectrum ($MnCl_2.4H_2O$) (Fig. 4.1A), corresponding to ligand-to-metal charge transfer (LMCT), vanished. Concurrently, the 291 nm and 312 nm bands (Fig. 4.1B), associated with π→π* and n→π* transitions in the free ligand, shifted to 267 nm and 307 nm (Fig. 4.1C), respectively, upon coordination with $Mn^{2+}$. The absorption band at 291 nm in the free ligand's spectrum shifted to a shorter wavelength of 267 nm after coordination with the $Mn^{2+}$ ion. This shift indicates that the energy required for the electronic transition associated with this absorption band has increased, causing the absorption to occur at a shorter wavelength. This shift suggests that the energy gap between the π and π* of the ligand is increased. This happened due to the flow of electrons from the $t_2g$ orbital of the metal center to the bonding ligand π orbital. Additionally, a new band emerged at 211 nm in the complex spectrum, signifying metal-to-ligand charge transfer (MLCT). Collectively, these findings strongly support the idea that the ligand has coordinated with the metal center, culminating in the formation of the desired complex.

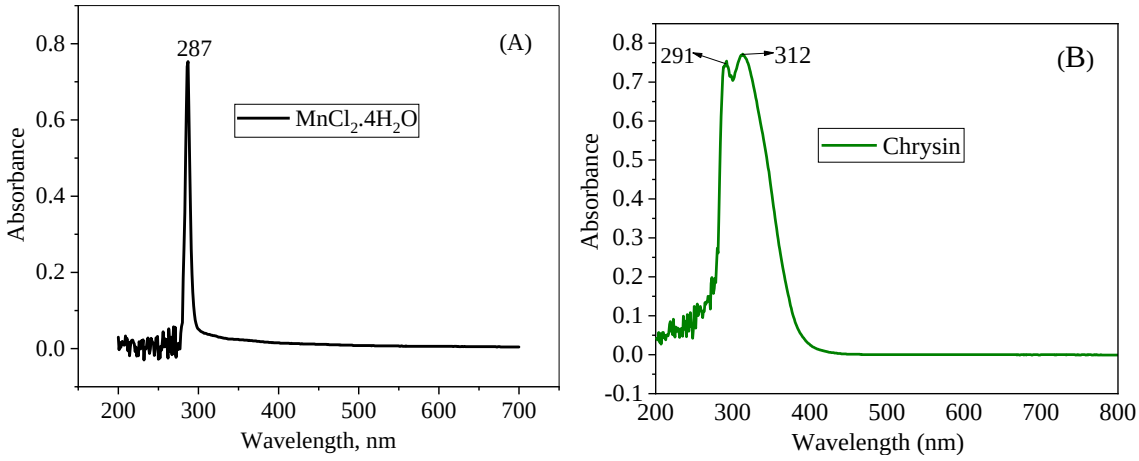

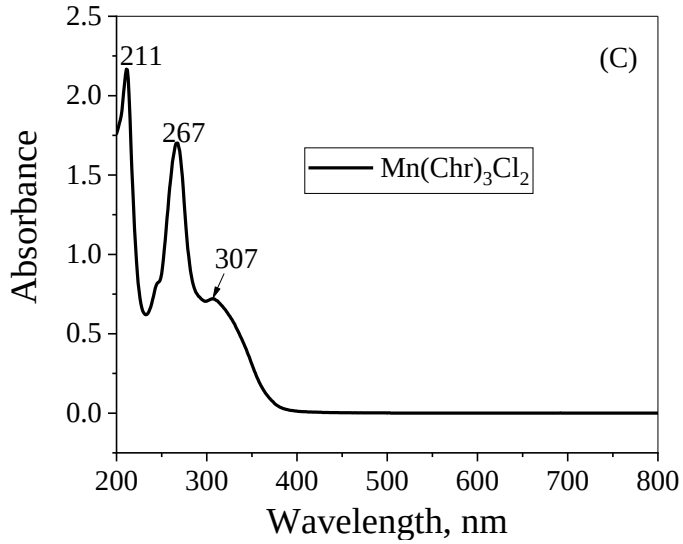


Fig. 4. 1: Electronic spectra of A) $MnCl_2.4H_2O$, B) Chrysin, C) $[Mn(Chr)_3]Cl_2$

#### 4.1.1.3. FT-IR Spectroscopy Characterization

In the spectrum of the free ligand (Chr) (Fig. 4.2A), a strong and broad absorption peak at 3084 $cm^{-1}$ corresponding to the νO-H stretching vibration is observed. Upon coordination with the metal center, this peak undergoes a shift and splits into two distinct bands at 3407 $cm^{-1}$ and 3215 $cm^{-1}$. The band at 3407 $cm^{-1}$ represents the νO-H vibration of the hydroxyl group directly coordinated with the metal, while the band at 3215 $cm^{-1}$ corresponds to the νO-H vibration of the ring containing the alcoholic and ketonic oxygens involved in coordination. Additionally, the band at 3097 $cm^{-1}$ corresponds to the νO-H vibration of the alcohol hydroxyl in the ring farther from the coordination center.

Furthermore, the absorption bands at 1652 $cm^{-1}$ and 1607 $cm^{-1}$ in the free ligand spectrum, associated with the νC=O and aromatic νC=C vibrations, were shifted to 1653 $cm^{-1}$ and 1614 $cm^{-1}$, respectively, after coordination with the metal center (Fig. 4.2B). This shift indicates an increase in bond order due to electron flow from the metal center to the ligand through a phenomenon known as π back bonding.

Collectively, these spectral changes provided compelling evidence supporting the hypothesis that the ligand has coordinated with the metal, forming the intended complex structure.

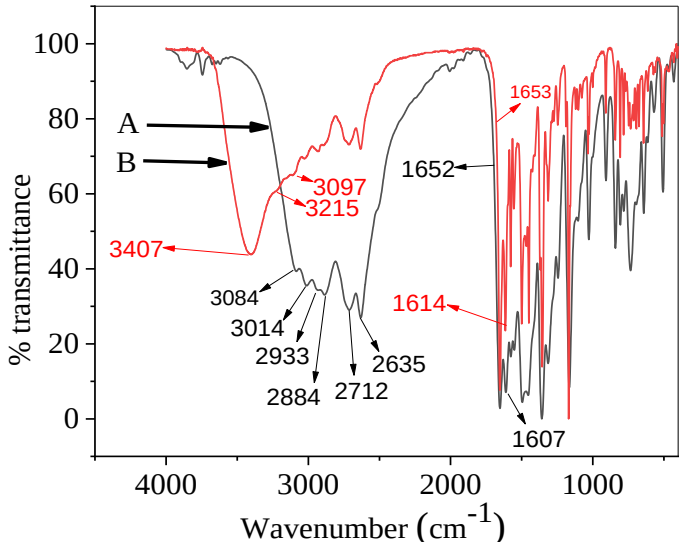


Fig. 4. 2: FT IR spectra of Chrysin (A) and $[Mn(Chr)_3]Cl_2$ (B)

Based on the results, the proposed reaction path of the complex is shown in (eq. (4.1)) and (Scheme 4.1).

$MnCl_2.4H_2O + 3C_{17}H_{14}O_7 \rightarrow [Mn(C_{17}H_{14}O_7)_3]Cl_2$ or $([Mn(C_{51}O_{24}O_{21})]Cl_2)$ ……..(4.1)

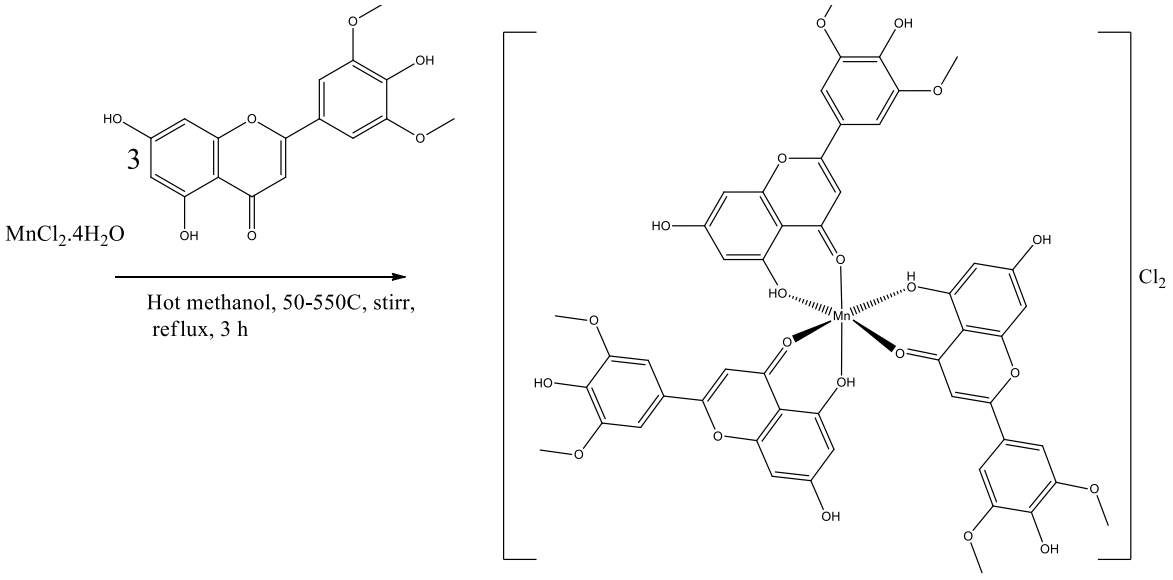


Scheme 4. 1: The proposed reaction path of the complex

### 4.1.2. Assembled Working Pencil Graphite Electrode

The assembled working pencil graphite electrode used in this work was shown in Fig 4.3. The length of the pencil height to be inserted in a solution was determined to be 4 mm to co-relate the area with area of glassy carbon electrode using the equation (area = $\pi r^2$ + $2\pi rh$) Where r = radius, h = height and $\pi$ =3.14. Fig 4.3A showed the zoomed part of Fig 4.3B. As we can see in the Fig. 4.3C, all the four pencil graphite electrodes which are modified on one end are nearly equal in length. Being equal in length inserted and modified by a modifier confirms the technique used to seal the plastic tube tip, can effectively protected the solution from leakage.

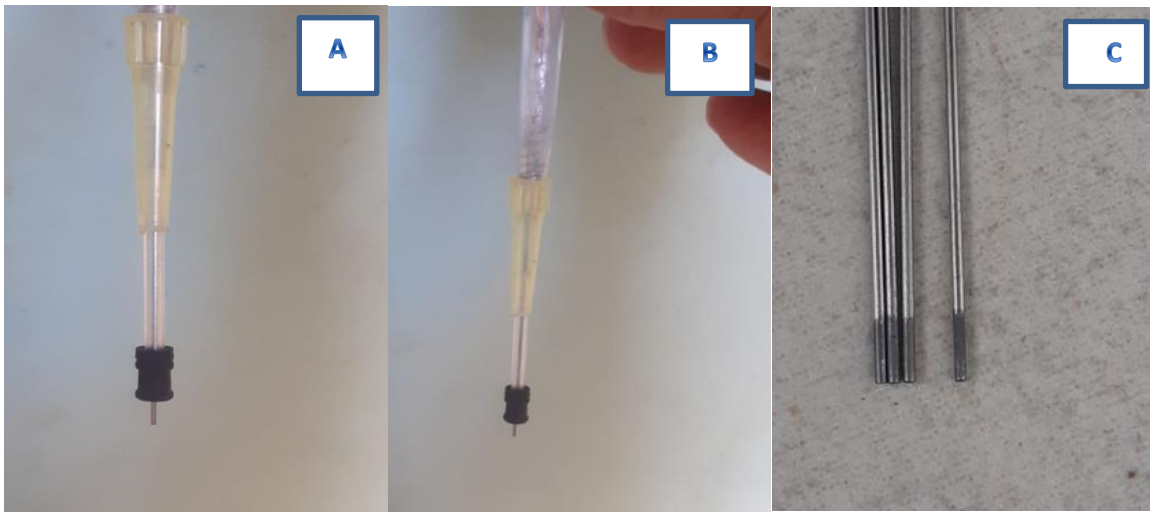


Fig. 4. 3: Assembled pencil graphite working electrode (A) and (B) the tip of the pencil graphite working electrode used as a working electrode (C)

### 4.1.3. Selection of Supporting Electrolyte

The electrochemical characteristics of species are dependent on an electrolyte used as a supporting electrolyte. 0.1M of phosphate buffer solution (PBS), acetate buffer solution (ABS), and Britton-Robinson buffer solution (BRS) were the supporting electrolytes that have been studied in this work. The supporting electrolyte for this study was selected using the CV voltammograms of 0.5 mM Cpro, which were prepared in the three different buffer solutions. As shown in Fig. 4.4, the voltammogram of 0.5 mM Cpro

prepared in ABS showed the most intense peak. This is because the oxidation peak of 0.5 mM Cpro in the acetate buffer solution produces an improved peak current. Zoubir and his co-authors [166] showed similar results. As a result, ABS was selected as a supporting electrolyte for the analysis of Cpro in this work.

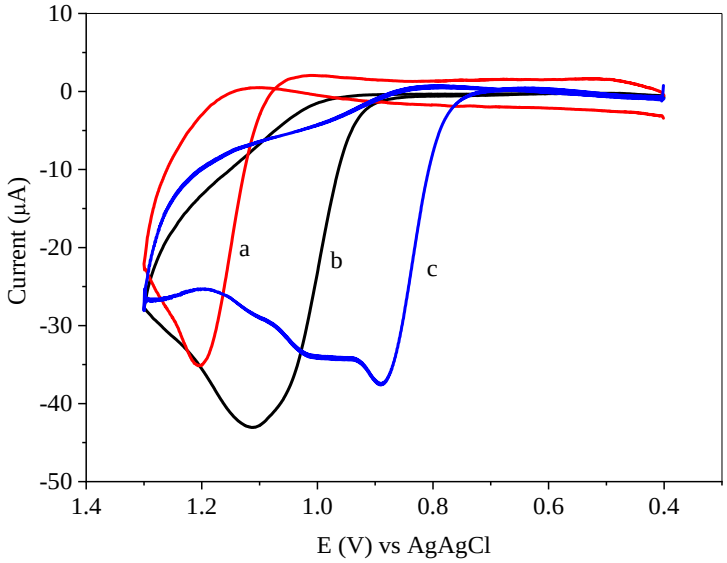


Fig. 4. 4: CVs of 0.5 mM Cpro in different buffer solutions with 0.1M of (a) Britton-Robinson buffer solution, (b) acetate buffer solution, and (c) phosphate buffer solution at 100 $mVs^{-1}$ scan rate and using poly $[Mn(Chr)_3]Cl_2$/PGE.

### 4.1.4. Optimization of Potential Window

The potential window for electropolymerization of 0.8 mM $[Mn(Chr)_3]Cl_2$ on the surface of PGE was optimized using a constant scan cycle at 15 and varying potential windows. These various potential windows were -0.5 to +2.0 V, -1.0 to +2.0 V, -1.5 to +2.0 V, and -2.0 to +2.0 V. As shown in Fig. 4.5, the potentiodynamic polymerization potential window of -0.5 to +2.0 V peak B(d) provides a maximum oxidative peak current of 0.5 mM Cpro. As a result, the potential window between -0.5 and +2.0 was optimized for the electropolymerization of $[Mn(Chr)_3]Cl_2$ at PGE [167].

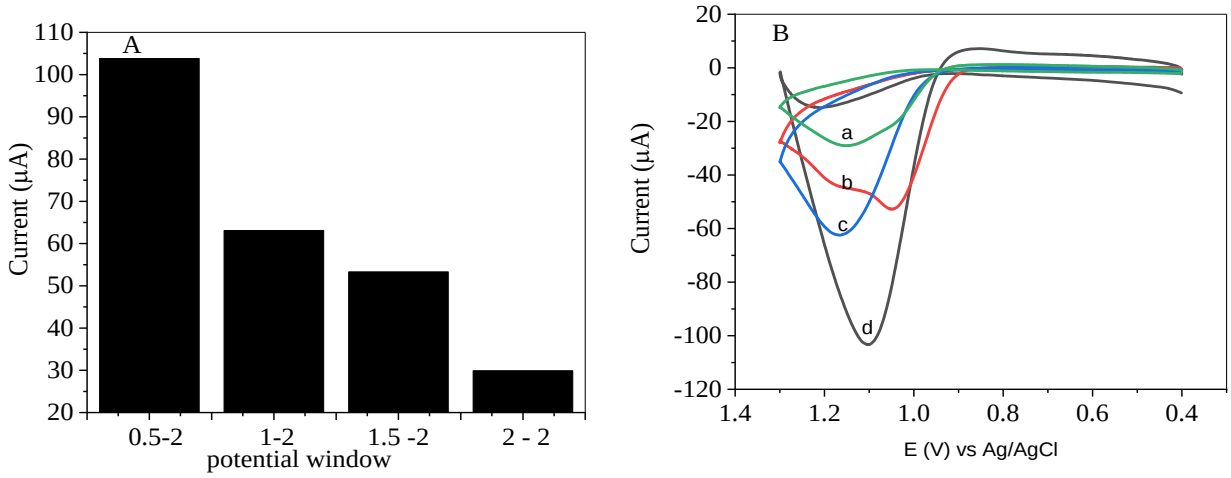


Fig. 4. 5: CVs of 0.5 mM Cpro in pH 4.7 ABS (A) a plot of peak current vs. potential window and (B) plots at poly $[Mn(Chr)_3]Cl_2$/PGE synthesized by scanning the potential window between (a) -2 &+2 V, (b) -1.5 & +2 V, (c) -1 &+2 V, and (d) - 0.5 & +2 V using 100 $mVs^{-1}$ for 15 scan cycles.

### 4.1.5. Optimization of Film Thickness

The film thickness of the modified electrode was optimized by polymerizing the electrode at various polymerization scan cycles and evaluating the performance of the modified electrode on the oxidation of Cpro. The CVs of 0.5 mM Cpro using the electrode polymerized at 5, 8, 10, 13, and 15 scan cycles are shown in Fig. 4.6. The oxidative peak current slightly increased from 5 to 10 scan cycles, and then it decreased from 10 to 15 scan cycles. This tells us that the electroactive polymer film thickness was formed at 10 scan cycles. Therefore, 10 scan cycles were chosen as the optimum film thickness [168].

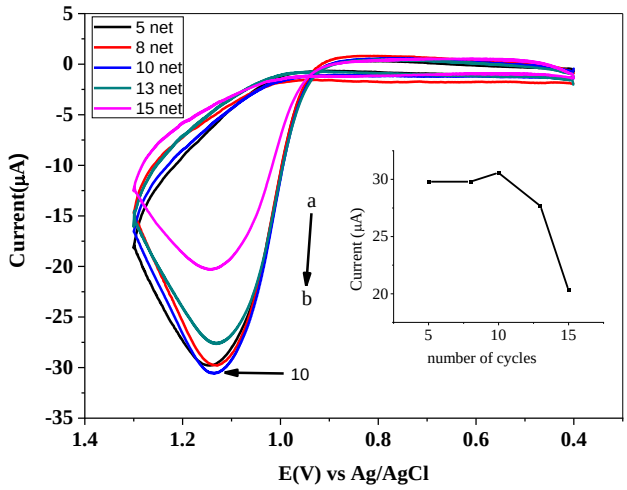


Fig. 4. 6: CVs of 0.5 mM CPro in pH 4.7 ABS at poly $[Mn(Chr)_3]Cl_2$/PGE synthesized in different numbers of scan cycles (5, 8, 10, 13, and 15) at 100 $mVs^{-1}$ scan rate, in (-0.5 to +2 V) potential window, and using 0.8 mM $[Mn(Chr)_3]Cl_2$: Inset plot of absolute value of current vs. number of scan cycles.

### 4.1.6. Polymerization voltammograms of Poly $[Mn(Chr)_3]Cl_2$/PGE

The PGE electrode was modified using 0.8 mM $[Mn(Chr)_3]Cl_2$ monomer and optimized parameters like film thickness, supporting electrolyte, and potential window. Fig. 4.7 shows the $[Mn(Chr)_3]Cl_2$ monomer polymerization CV voltammograms. As shown in Fig 4.6, the cathodic peak raised with increased scan cycles, signifying the growth of electroactive film deposition on the PGE electrode surface [169].

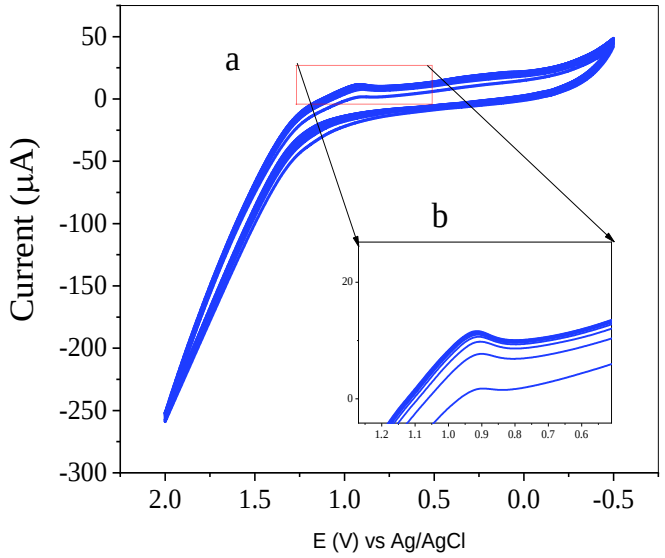


Fig. 4. 7: CVs of 0.8 mM $[Mn(Chr)_3]Cl_2$ scanned between -0.5 to +2.0 V at 100 mV/s for 10 scan cycles (a) and (b) is the zoom of (a), which shows the peak enhancement.

### 4.1.7. Characterization of the Poly $[Mn(Chr)_3]Cl_2$/PGE

#### 4.1.7.1. Cyclic Voltammetry Characterization of Poly $[Mn(Chr)_3]Cl_2$/PGE

The modified electrode was characterized using cyclic voltammetry and 10.0 mM $[Fe(CN)_6]^{-3/-4}$ solution as a probe in 0.1 M KCl. Fig. 4.8 shows that both cathodic and anodic peak currents were increased relative to the bare PGE electrode. At poly $[Mn(Chr)_3]Cl_2$/PGE, the anodic peak current of $[Fe\ (CN)_6]^{-3/-4}$ was 2.36 times higher than the current at the bare PGE. The poly $[Mn(Chr)_3]Cl_2$/PGE modified electrode has a peak-to-peak separation of (140.58 mV), which is less than that of the bare PGE (178.65 mV). This might be the result of increased electroactive surface area and/or quicker electron transport between the modified electrode and the analyte relative to bare PGE [170].

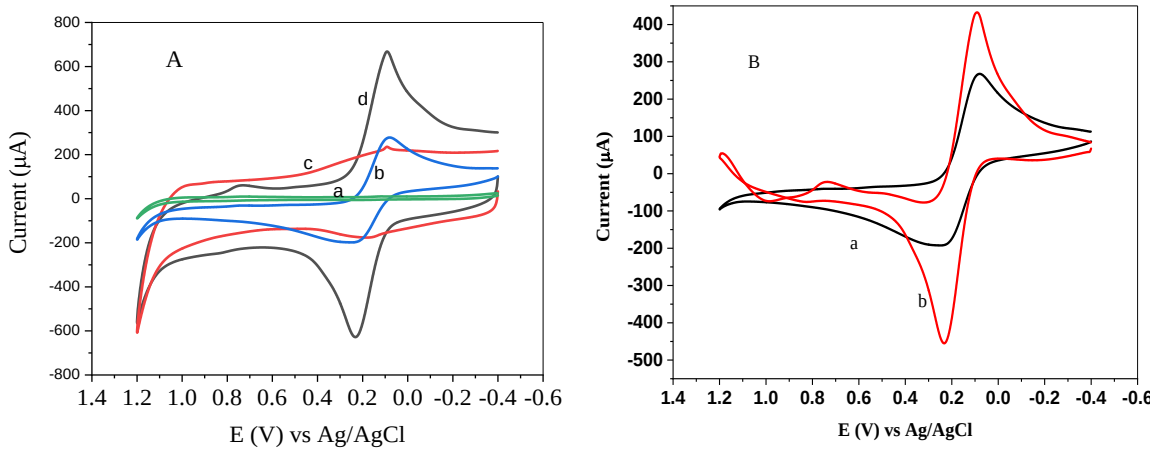


Fig. 4. 8: CVs of (A) absence (a and c) and presence (b and d) of 10.0 mM $[Fe(CN)_6]^{-3/-4}$ in 0.1 M KCl; (b) unmodified PGE; (d) poly $[Mn(Chr)_3]Cl_2$/PGE modified electrode; and (B) CVs of blank subtracted (a) bare PGE and (b) $[Mn(Chr)_3]Cl_2$/PGE modified electrode at 100 $mVs^{-1}$.

The anodic peak current of poly $[Mn(Chr)_3]Cl_2$/PGE scanned in 0.5 M $H_2SO_4$ between -0.8 and +0.8 V is significantly increased from -10.8 to -164.1 µA relative to bare PGE. This current enhancement can confirm the effective modification of the PGE by electroactive modifier. Fig. 4.9 shows the overlay of the two voltammograms of bare PGE (a) and poly $[Mn(Chr)_3]Cl_2$/PGE (b).

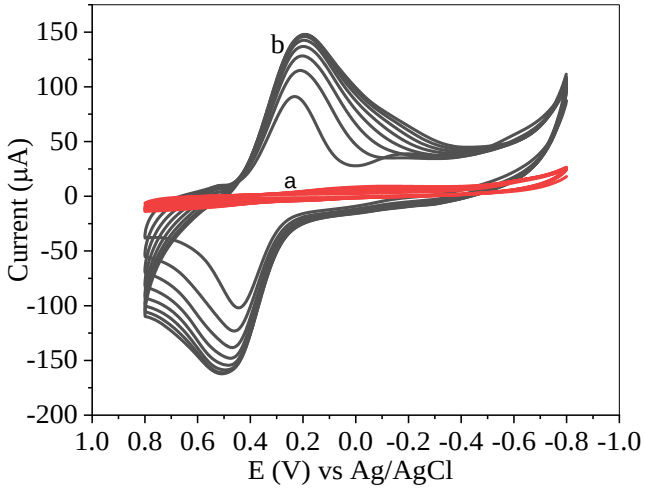


Fig. 4. 9: CVs of 0.5 M $H_2SO_4$ (a) bare PGE and (b) poly $[Mn(Chr)_3]Cl_2$/PGE scanned between -0.8 and +0.8 V with 100 $mVs^{-1}$ scan rate and for 8 scan cycles.

Cyclic voltammetric measurements of 10.0 mM $[Fe(CN)_6]^{-3/-4}$ in 0.1 M KCl at various scan rates (10-300 mV/s) were carried out to examine the effective electroactive surface area of the bare and modified electrode. Using the Randles–Ševčik equation shown in equation 4.2, the effective electroactive surface area of the bare and modified electrodes was determined from the slope value of the plots of current versus square root of scan rate as shown in Fig. 4.10 (i and ii) [171].

$$I_{pa} = 2.69 \times 10^5 \times n^{3/2} A D^{1/2} V^{1/2} C_o \quad \text{..... (4.2)}$$

Where n = number of electrons involved during redox reaction for $[Fe(CN)_6]^{-3/-4}$(n = 1), $I_{pa}$ is the peak current, A is the effective surface area, D is the diffusion coefficient of $[Fe(CN)_6]^{-3/-4}$ (D = 7.6 x $10^{-6}$ $cm^2s^{-1}$), *v* is the scan rate, and $C_o$ is the concentration of $[Fe(CN)_6]^{-3/-4}$ (10.0 mM).

The effective electroactive surface area of the unmodified PGE electrode is calculated to be 0.38 $cm^2$ (Fig. 4.10A), and the effective electroactive surface area of the poly $[Mn(Chr)_3]Cl_2$/PGE electrode was calculated to be 1.07 $cm^2$ (Fig. 4.10B), which is roughly 3.0 times higher than that of the unmodified PGE surface area. This considerable effective electroactive surface area enhancement confirms the modification of PGE. The formation of electrochemically active sites on the surface of PGE in the modified electrode can offer more surfaces for detecting of Cpro.

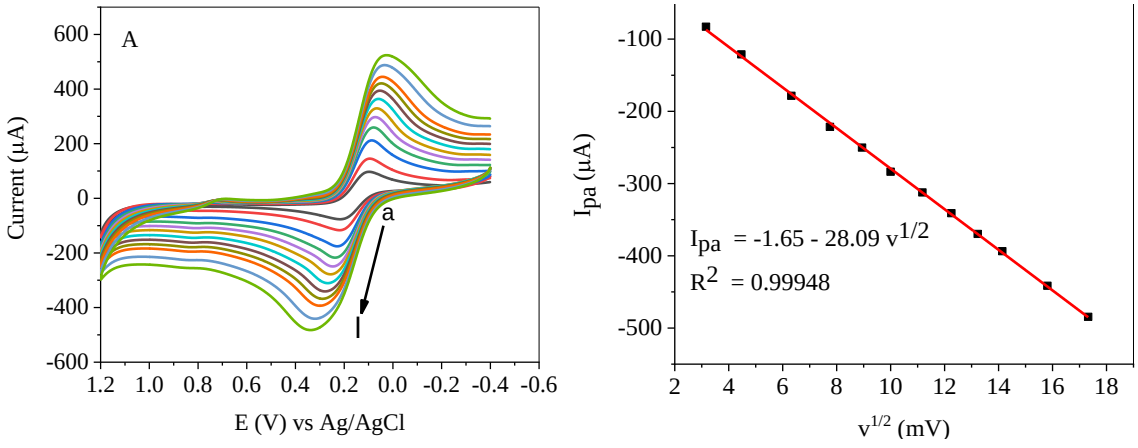

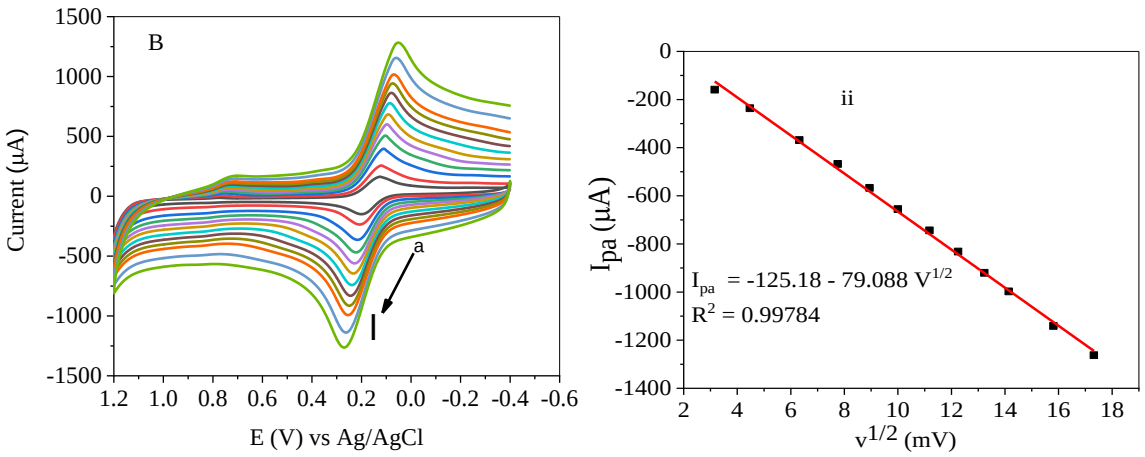


Fig. 4. 10: CVs of 10.0 mM $[Fe(CN)_6]^{-3/-4}$ in 0.1 M KCl (A) bare PGE and (B) poly $[Mn(Chr)_3]Cl_2$/PGE at different scan rates (10, 20, 40, 60, 80, 100, 125, 150, 175, 200, 250, and 300 $mVs^{-1}$) and (i and ii) are plots of $I_{pa}$ vs. $V^{½}$ of (A) and (B), respectively.

### 4.1.7.2. Electrochemical Behavior of Cpro at Poly $[Mn(Chr)_3]Cl_2$/PGE

CV was used to investigate the electrochemical behavior of 0.5 mM Cpro in pH 4.7 ABS at poly $[Mn(Chr)_3]Cl_2$/PGE and bare PGE, as illustrated in Fig. 4.11(i). As shown in Fig. 4.11(i), oxidation peak currents of Cpro increased from 5.2 to 43.4 with a single irreversible oxidation peak using bare PGE (Fig. 4.11ia) and poly $[Mn(Chr)_3]Cl_2$/PGE(Fig. 4.11ib), respectively. Poly $[Mn(Chr)_3]Cl_2$/PGE shows 8.4-fold current enhancement, and this confirms that poly $[Mn(Chr)_3]Cl_2$/PGE has a catalytic effect on Cpro oxidation. In both bare and modified PGE, the irreversible oxidation of Cpro is indicated by the absence of a reduction peak on the reverse scan of the cyclic voltammogram [172].

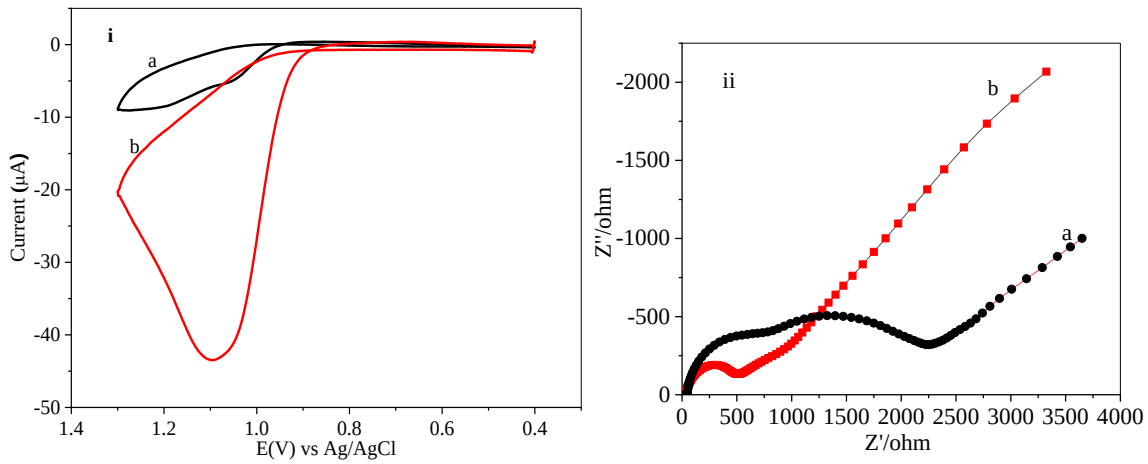


Fig. 4. 11: CVs of blank subtracted 0.5 mM Cpro in pH 4.7 of bare PGE i(a) and poly $[Mn(Chr)_3]Cl_2$/PGE i(b) at a scan rate of 100 mV/s and (ii) Nyquist plot of 10.0 mM $[Fe(CN)_6]^{3-/4-}$ in 0.1 M KCl at PGE ii(a) and poly $[Mn(Chr)_3]Cl_2$/PGE ii(b) in the frequency range: 0.01-10,000 Hz, amplitude 0.01 V, and potential 0.23 V.

### 4.1.7.3. Electrochemical Impedance Spectroscopy Characterization

The measurement of electrochemical impedance spectroscopy (EIS) was carried out in 0.1 M KCl containing 10.0 mM [Fe (CN) 6]$^{3-/4-}$, using the frequency range of 0.01–10,000 Hz. The semicircle and linear parts of the Nyquist plot of poly $[Mn(Chr)_3]Cl_2$/PGE and PGE are shown in Fig. 4.11(ii). The charge transfer resistance is shown by the diameter of the semicircle, and the diffusion of electroactive species towards the electrode interface is shown by the linear part of the Nyquist plot. The $R_{ct}$ value of poly $[Mn(Chr)_3]Cl_2$/PGE (Fig. 11(iib)), is 491.1Ω, which is smaller than the $R_{ct}$ value of bare PGE (Fig. 11 (iia)), which is 2206.2Ω, confirming that the rate of electron transfer between the modified electrode and the probe was increased [173]. The value of $C_{dl}$ was calculated using equation 4.3. All the values are listed in Table 4.2.

$$C_{dl} = \frac{1}{2\pi R_{ct} f} \text{----------(4.3)}$$

Where: $R_{ct}$–charge transfer resistance, $C_{dl}$ - double layer capacitance, and f-frequency corresponding to the maximum imaginary impedance

Table 4. 2: Calculated and measured values of EIS from Nyquist plot

| Electrode | Rs ($\Omega$ $cm^2$) | $R_{ct}$ ($\Omega$ $cm^2$) | $C_{dl}$ (F) | f (Hz) |
|---|---|---|---|---|
| **PGE (curve ii a)** | 44.3 | 2206.2 | $4.9 \times 10^{-6}$ | 14.68 |
| **Poly $[Mn(Chr)_3]Cl_2$/ PGE (curve ii b)** | 35.7 | 491.1 | $1.3 \times 10^{-6}$ | 258.8 |

#### 4.1.7.4. UV-Vis and Digital Optical Microscopy Characterization

The properties of polymerized $[Mn(Chr)_3]Cl_2$ have been studied by using UV-Vis and digital optical microscope methods and fluorine-doped tin oxide (FTO) as a substrate. FTO has been electropolymerized using a similar electropolymerization procedure optimized in pencil graphite electrode. The UV-Vis absorption spectra and digital optical microscope images were taken from bare and polymerized $[Mn(Chr)_3]Cl_2$ using FTO as a substrate, and the results are shown in Fig. 4.12. The absorption band intensity enhancement and the appearance of a new absorption band in the UV-Vis spectrum (Fig. 4.12Ab) compared to the bare FTO (Fig. 4.12Aa) confirm the modification of the surface of FTO. The number of absorption bands discussed in the complex characterization section (Fig. 4.1) is reduced to two with redshift. The band number reduction and peak shift relative to the monomer ($[Mn(Chr)_3]Cl_2$), confirm the formation of poly ($[Mn(Chr)_3]Cl_2$)/FTO.

The images of the surface of FTO before and after deposition of the polymer were taken using a digital optical microscope at 5 mm distance and 1800x magnification scale. The surface of FTO before modification was shown in Figure 4.12B; after modification but before washing with $H_2SO_4$ was shown in Figure 4.12C; and after modification and washing by $H_2SO_4$ was shown in Figure 4.12D. The polymerized FTO before washing with $H_2SO_4$ is yellow colored due to the adsorbed monomers but after washing with $H_2SO_4$ the color was removed due to removal of the monomers. The surface of unmodified FTO is smooth (Fig. 4.12B), but the surface of the modified FTO is rough (Fig. 4.12D). The change of surface of FTO from smooth to roughness due to electropolymerization confirms the deposition of the polymer on the surface of FTO.

Since an identical electropolymerization procedure was followed, a similar deposition and distribution of the polymer on the surface of the pencil graphite electrode was assumed.

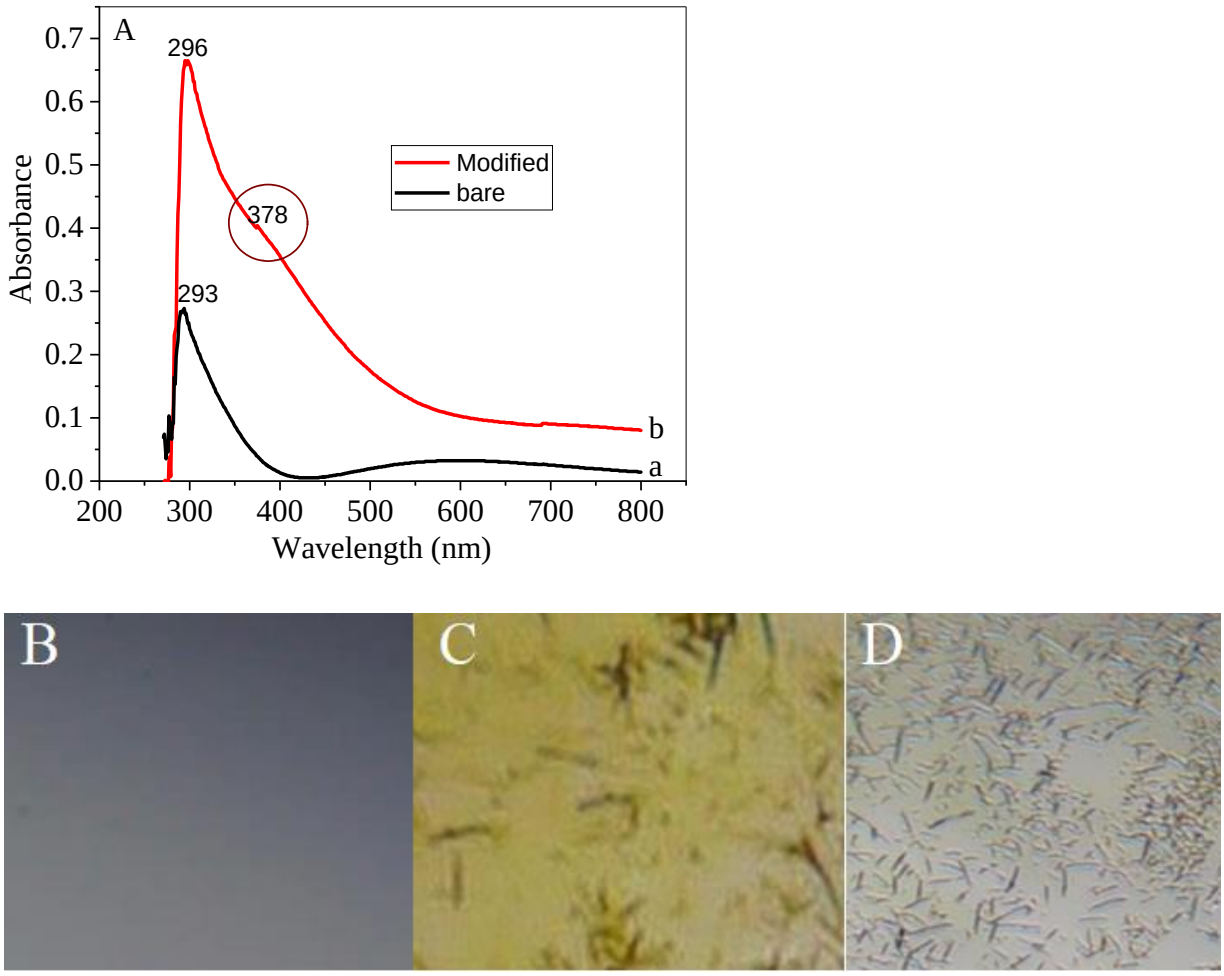


Fig. 4. 12: UV-Vis spectra of poly $[Mn(Chr)_3]Cl_2$ on the surface of FTO (A) and digital optical microscopy images at 5 mm distance and 1800x magnification scale (B, C, and D);(A(a) and B) are using bare FTO and (A(b), C, and D) are using modified FTO.

### 4.1.8. Effect of Scan Rate on $E_{pa}$ and $I_{pa}$ of Cpro

The effect of scan rate on the peak potential and peak current of Cpro in ABS of pH 4.7 solution was investigated using CV. The scan rate was varied from 10 to 300 $mVs^{-1}$ and the voltammogram is shown in Fig. 4.13. The voltammograms indicate that when the scan rate was raised, the peak current increased, and there was a potential shift to the more positive potential, indicating that Cpro was undergoing an irreversible oxidation reaction [172]. Plots of the oxidative peak current vs. scan rate and peak current vs. square roots of scan rate have been made (Fig. 4.14). The oxidation reaction of Cpro was likely mass transport-controlled, as indicated by the greater value of the correlation coefficient ($R^2$ = 0.9887) of the plot of peak current against the square root of the scan rate.

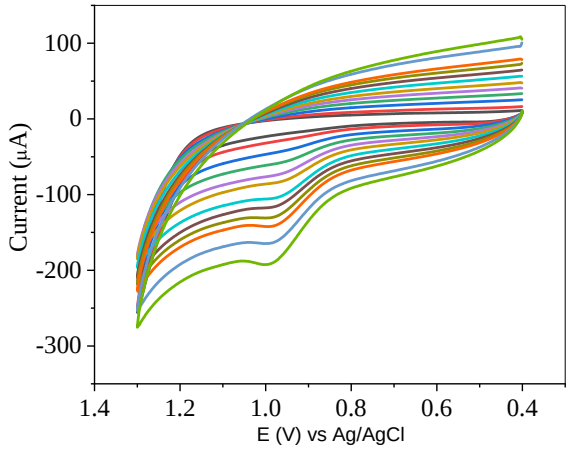


Fig. 4. 13: CVs of 0.5 mM Cpro in pH 7.5 at different scan rates from 10, 20, 40, 60, 80, 100, 125, 150, 175, 200, 250, and 300.

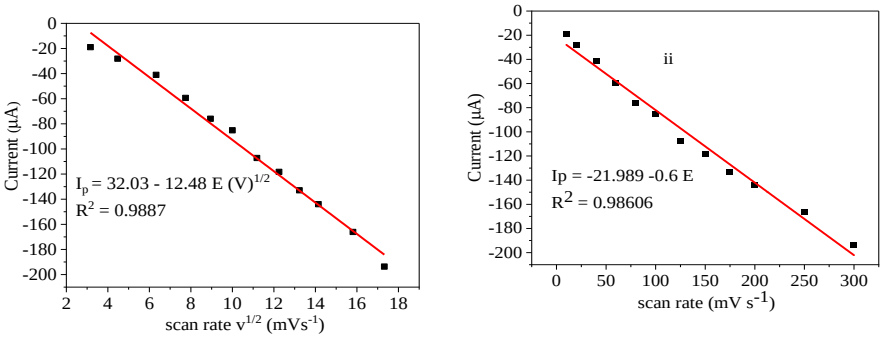


Fig. 4. 14: plot of $I_{pa}$ vs. $v^{1/2}$ (i) and plot of $I_{pa}$ vs. V (ii).

The number of electrons transferred during the oxidation of Cpro was calculated using the following equation 4.4.

$$E_p - E_{p1/2} = \frac{48}{\alpha n} \quad \text{---------- (4.4)}$$

The values of $E_p$ and $E_{p1/2}$ obtained from the cyclic voltammogram of Cpro Fig. 4.11(i) at a scan rate of 100 $mVs^{-1}$ were 1072 and 1010 mV, respectively, and their difference is 62. The value of αn was calculated to be 0.774, and the value of α for a totally irreversible process is 0.5. As a result, the calculated value of n was 1.55, which is closer to 2 and in agreement with the reported literature value [174].

### 4.1.9. Effect of pH on the Oxidation of Cpro

The influence of pH on the oxidation peak current and oxidation peak potential of Cpro was investigated in order to observe the participation of protons and the proton-to-electron ratio. Figs. 4.15A and 15B (a) illustrate how the oxidation peak current of Cpro at poly $[Mn(Chr)_3]Cl_2$/PGE increased from pH 3.0 to 7.5 and then declined. Therefore, pH value of 7.5 was optimized for further analysis.

As the pH value increased from 3.0 to 8.0, the oxidation peak potential shifted in the negative direction, showing that protons were involved in the redox reaction [175]. Plotting Cpro oxidation peak potential against ABS pH (Fig. 4.15B (b)) shows a slope of 0.053, which is very close to the ideal Nernst value of 0.0592V/pH. The slope value is closer to the ideal value, indicating that protons and electrons participated in the oxidation reaction process in a 1:1 ratio [176, 177].

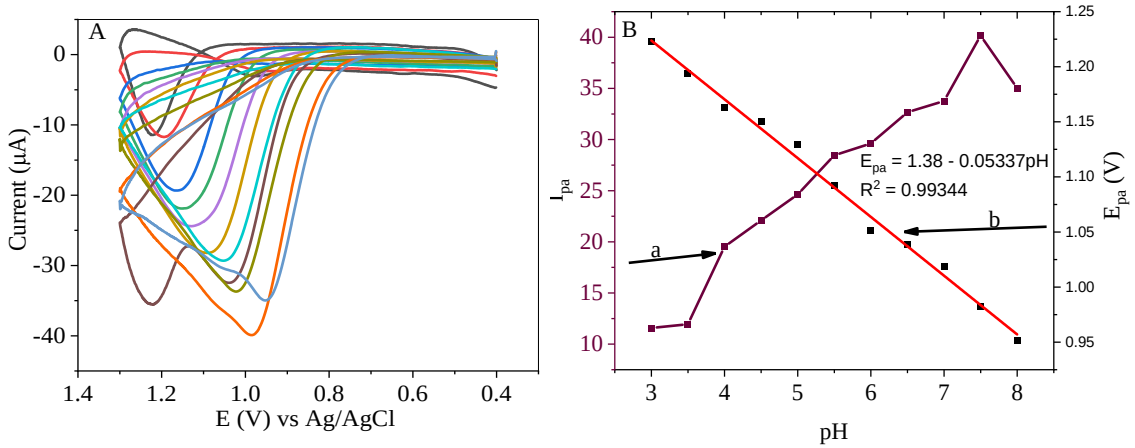


Fig. 4. 15: CVs of 0.5 mM Cpro in ABS at different pH values (3.0, 3.5, 4.0, 4.5, 5.0, 5.5, 6.0, 6.5, 7.0, 7.5, and 8.0) using poly $[Mn(Chr)_3]Cl_2$/PGE at a scan rate of 100 $mVs^{-1}$ (A) and plotting of peak current vs. pH B(a) and peak current vs. peak potential B(b).

Scheme 4.2 shows the proposed reaction mechanism of the oxidation of ciprofloxacin in the modified electrode

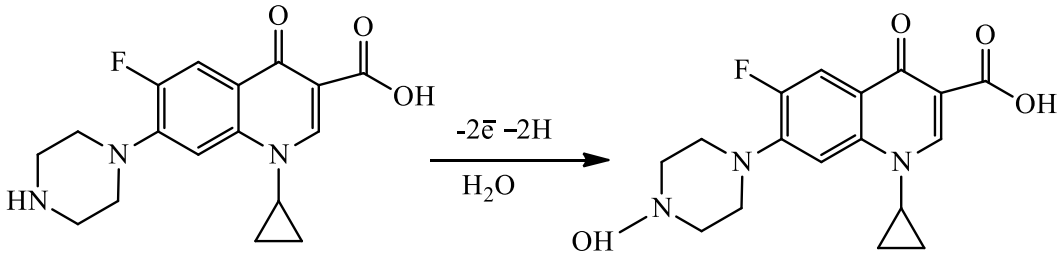


Scheme 4. 2: The proposed reaction mechanism of ciprofloxacin

### 4.1.10. Square Wave Voltammetric Parameter Optimization

SWV determination of Cpro using poly $[Mn(Chr)_3]Cl_2$/PGE was affected by step potential, amplitude, and frequency [178]. Therefore, by changing one of these parameters while maintaining the others constant, these factors were optimized using 0.5 mM Cpro. Step potential was varied starting from 2 to 12 $mVs^{-1}$ and optimized at 6 $mVs^{-1}$; amplitude was varied from 10 to 50 mV and optimized at 35 mV; and frequency was varied between 10 and 50 Hz and optimized at 30 Hz. The voltammograms of step potential, amplitude, and frequency were plotted and shown in Fig. 4.16, Fig. 4.17, and Fig. 4.18, respectively [179, 180].

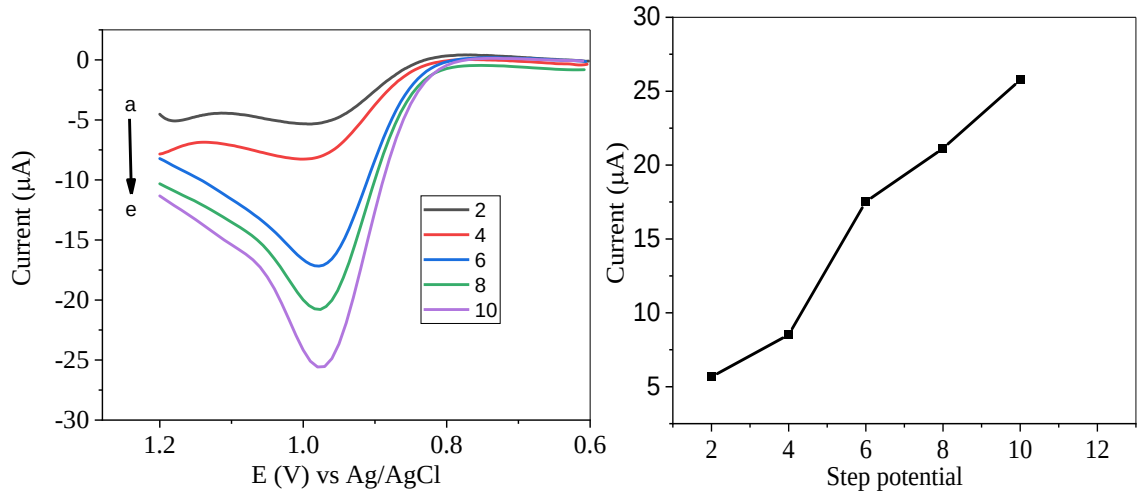


Fig. 4. 16: SWVs of pH 7.5 ABS containing 0.5 mM Cpro at various step potentials (2, 4, 6, 8, and 10 $mVs^{-1}$) at 25 mV amplitude and 15 Hz frequency using poly $[Mn(Chr)_3]Cl_2$/PGE.

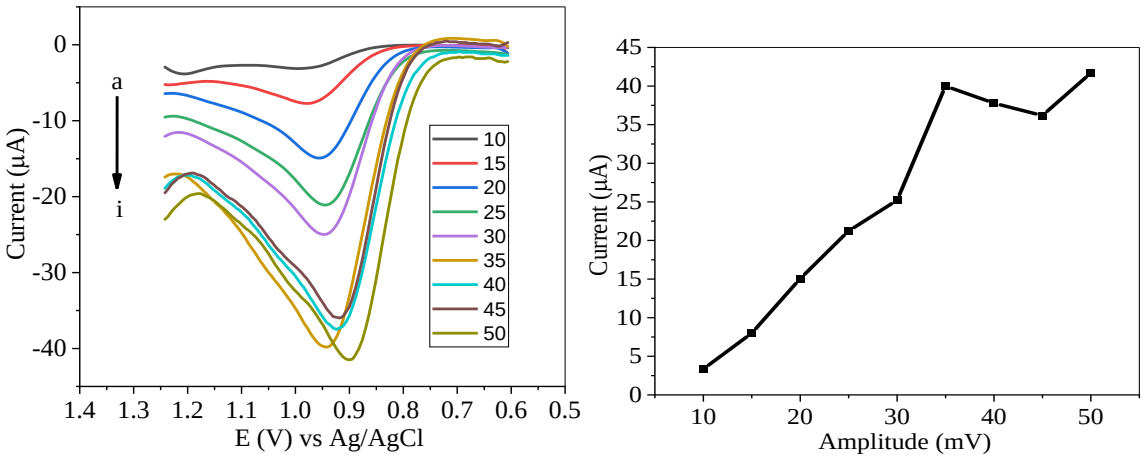


Fig. 4. 17: SWVs of pH 7.5 ABS containing 0.5 mM Cpro at various amplitudes (a-i; 10, 15, 20, 25, 30, 35, 40, 45, 50 mV) at 6 $mVs^{-1}$ step potentials and 15 Hz frequency using poly $[Mn(Chr)_3]Cl_2$/PGE.

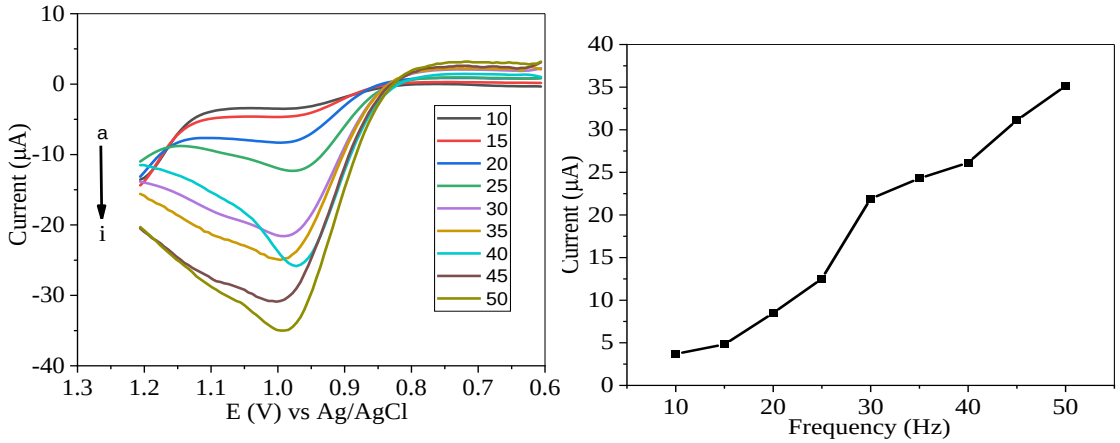


Fig. 4. 18: SWVs of pH 7.5 ABS containing 0.5 mM Cpro at various frequencies (10, 15, 20, 25, 30, 35, 40, 45, and 50) at 6 $mVs^{-1}$ step potentials and 35 mV amplitude using poly $[Mn(Chr)_3]Cl_2$/PGE.

### 4.1.11. SWV Activity of Cpro

The electroactivity of ciprofloxacin in SWV using bare PGE and poly $[Mn(Chr)_3]Cl_2$/PGE was studied. As shown in Fig. 4.19, the peak current of poly $[Mn(Chr)_3]Cl_2$/PGE of 0.5 mM Cpro at the optimized parameters was -51.28 µA, and the peak potential was 0.9701 V. But using bare PGE, the peak current of 0.5 mM Cpro was -16.54 µA, and the peak potential was 1.0216 V. The oxidative peak of Cpro at poly $[Mn(Chr)_3]Cl_2$/PGE (Fig. 4.19b) was about threefold in current enhancement and reduced potential compared to the oxidative peak at bare PGE (Fig. 4.19a). This indicates poly $[Mn(Chr)_3]Cl_2$ film has a catalytic role in the oxidation of Cpro.

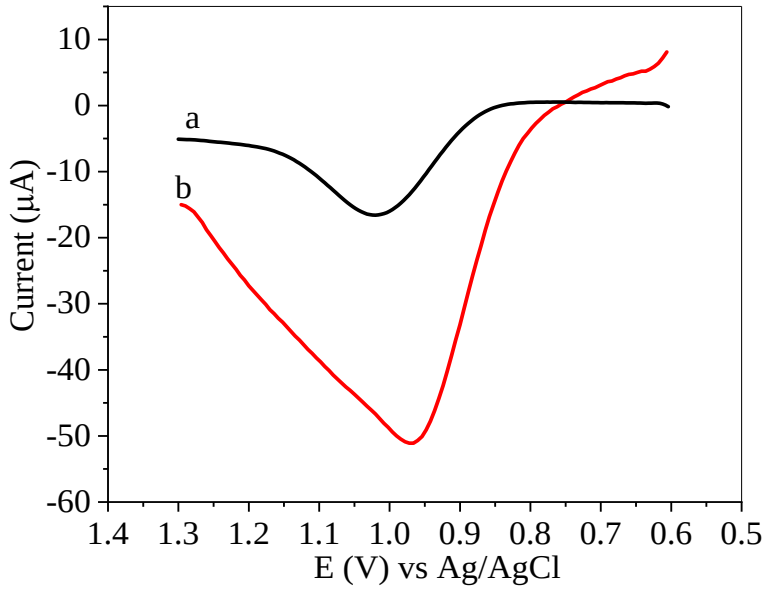


Fig. 4. 19: SWVs of pH 7.5 ABS containing 0.5 mM Cpro at step potential 6 $mVs^{-1}$, amplitude 35 mV, and frequency 30 Hz of bare PGE electrode (a) and poly $[Mn(Chr)_3]Cl_2$/PGE (b).

### 4.1.12. Method Calibration

The SWV method using the developed $[Mn(Chr)_3]Cl_2$/PGE modified electrode was calibrated by preparing a standard solution of Cpro with different concentration ranges of Cpro from 1.0 µM to 250 µM in order to determine Cpro in real samples [181]. Fig. 4.20 illustrates how the current peak of the SWV voltammograms using the modified pencil graphite electrode increased in the concentration range in line with increasing Cpro concentration. The plot of the calibration curve provides a slope value of -0.161, which is related to the method sensitivity.

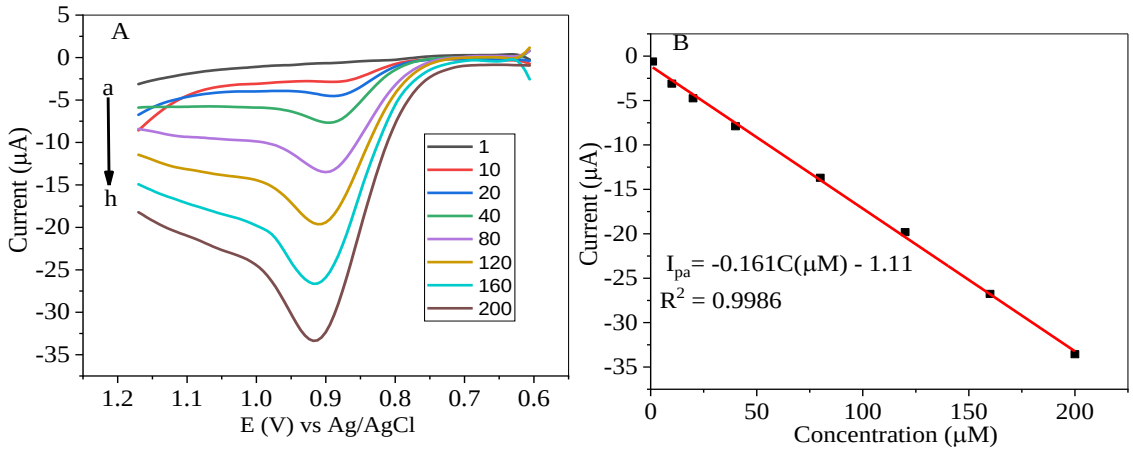


Fig. 4. 20: Blank corrected SWVs of pH 7.5 containing various concentrations of Cpro (1.0, 10.0, 20.0, 40.0, 80.0, 120.0, 160.0, and 200.0 µM) at poly $[Mn(Chr)_3]Cl_2$/PGE (A) and its plot of current vs. concentration (B) at step potential 6 $mVs^{-1}$, amplitude 35 mV, and frequency 30 Hz.

### 4.1.13. Real Sample Analysis

#### 4.1.13.1. Human Urine Sample Analysis

Human urine sample analysis was conducted using the spiked method. The urine sample was spiked with 20 µM, 40 µM, and 60 µM of Cpro, and analysis was made using the SWV technique. As shown in Fig. 4.21, the SWV voltammograms confirm the presence of characteristic peaks of uric acid (Fig. 4.21c) and Cpro (Fig. 4.21a) separately in the spiked urine sample [182]. Peak (a), the typical peak of Cpro, increased with its concentration. Peak current variations of peak 'b' and 'c' are irrespective of concentrations of Cpro. This confirms that the matrices in the urine samples have no effect on Cpro, and Cpro itself has no effect on uric acid in urine samples [183]. Therefore, the developed method can simultaneously analyze Cpro in urine samples without interfering with each other. The recovery of the spiked urine samples was 92.8 % to 114.9 %, as listed in Table 4.3.

Table 4. 3: Recovery results of Cpro in human urine samples.

| Un-spiked | Added (µM) | Cpro | Found (µM) | % Recovery |
|---|---|---|---|---|
| **ND** | 20.0 | | 23.0 ± 0.6 | 114.9 |
| **ND** | 40.0 | | 38.9 ± 0.8 | 97.4 |
| **ND** | 60.0 | | 55.7 ± 1.0 | 92.8 |
| **ND: not detected** | | | | |

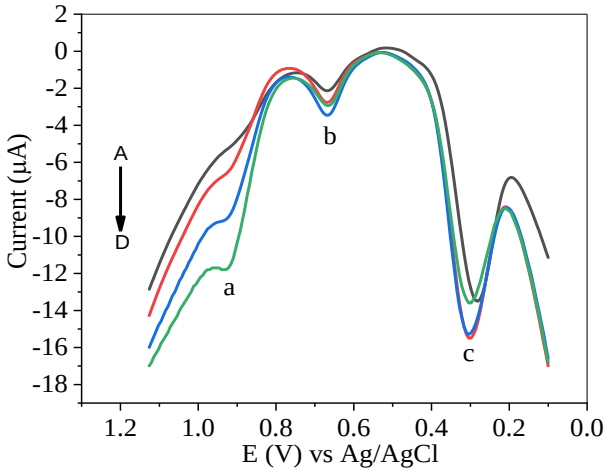


Fig. 4. 21: Background corrected SWVs of pH 7.5 ABS containing (A) un-spiked urine sample, (B) (A + 20 µM), (C) (A + 40 µM), and (D) (A + 60 µM), and peak a, b, and c represents Cpro, creatinine, and uric acid, respectively at step potential 6 $mVs^{-1}$, amplitude 35 mV, and frequency 30 Hz using poly $[Mn(Chr)_3]Cl_2$/PGE

### 4.1.13.2. Tablet Samples from Two Brands

Determination of the concentration of Cpro in tablet samples and recovery analysis using poly $[Mn(Chr)_3]Cl_2$/PGE were conducted to test the developed method's validity. 80.0 µM concentrations of Ciproscot and Zindolin brand samples were spiked with 40.0 µM, 80.0 µM, and 120.0 µM Cpro standard solutions in order to perform the validity of the developed method. The results are presented in Table 4.4 and Fig. 4.22 (A) and (B). As shown in Table 4.4, the recovery results were in the ranges of 84.5–114.3, which is in the accepted range, suggesting that the proposed method can be used to determine Cpro in pharmaceutical samples in an efficient manner.

Table 4. 4: Recovery results of Cpro in each tablet brand samples.

| Brand tablets | Un-spike (µM) | Added amount (µM) | Measured amount (µM) | % Recovery |
|---|---|---|---|---|
| **Ciproscot** | 80.0 | 0.0 | 67.6 ± 1.3 | 84.5 |
| | 80.0 | 40.0 | 134.7 ± 2.2 | 112.2 |
| | 80.0 | 80.0 | 170.1 ± 2.1 | 106.3 |
| | 80.0 | 120.0 | 217.9 ± 1.3 | 108.9 |
| **Zindolin** | 80.0 | 0.0 | 73.8 ± 1.7 | 92.3 |
| | 80.0 | 40.0 | 124.2 ± 2.3 | 103.5 |
| | 80.0 | 80.0 | 163.3 ± 1.5 | 102.1 |
| | 80.0 | 120.0 | 228.5 ± 2.6 | 114.3 |

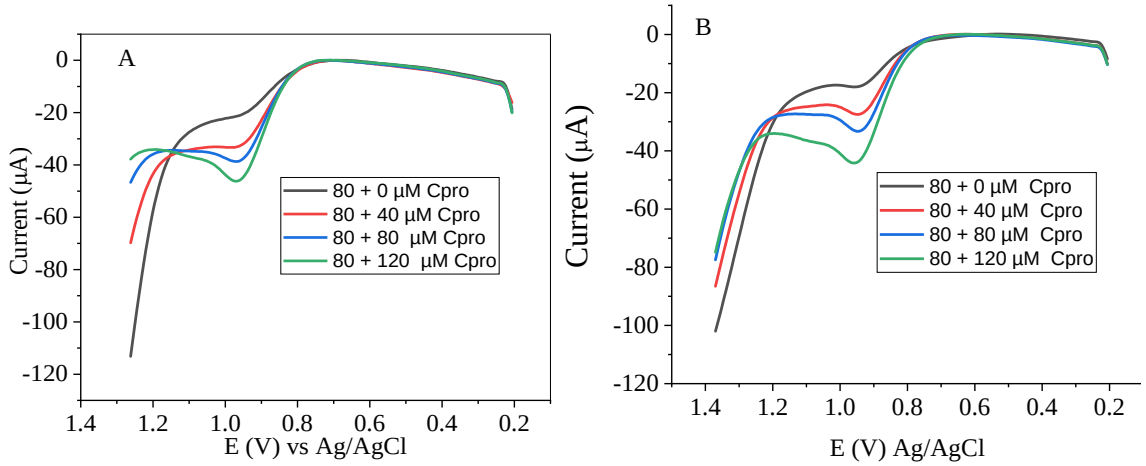


Fig. 4. 22: Background corrected SWVs of Ciproscot (A) and Zindolin (B) brand pharmaceutical samples spiked with various concentrations of standards Cpro (0.0 +80.0, 80.0 +40.0, 80.0 +80.0, and 80.0 +120.0) at a poly $[Mn(Chr)_3]Cl_2$/PGE in ABS of pH 7.5 at step potential 6 $mVs^{-1}$, amplitude 35 mV, and frequency 30 Hz.

### 4.1.14. Selectivity Study

The selectivity of the proposed method has been evaluated in the presence of paracetamol and uric acid. The impact was investigated at different concentrations of paracetamol and uric acid. The characteristic peaks of uric acid and paracetamol appear separately from the characteristic peaks of Cpro, as shown in Figs. 4.23(a and b) and 24(a and b), respectively. Uric acid and paracetamol have no signal at the characteristic peak of Cpro. The characteristic peak of Cpro remains constant as the interference concentration rises.

This constant peak of Cpro confirms that the developed method can analyze Cpro selectively in the presence of uric acid and paracetamol.

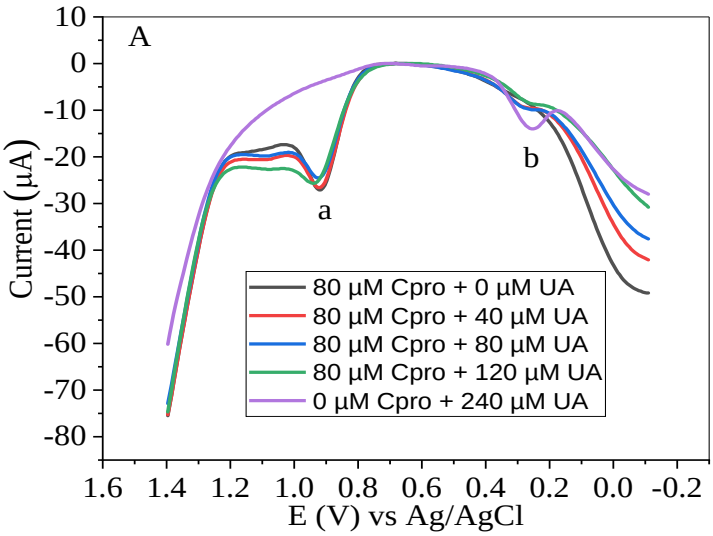


Fig. 4. 23:Background corrected SWVs of pH 7.5 ABS containing (0 + 80 µM Cpro), (40 µM Urine + 80 µM Cpro), (80 µM Urine + 80 µM Cpro), (120 µM Urine + 80 µM Cpro), and (240 µM Urine + 80 µM Cpro); peak (a), Cpro, and (b), uric acid at step potential 6 $mVs^{-1}$, amplitude 35 mV, and frequency 30 Hz using poly $[Mn(Chr)_3]Cl_2$/PGE.

Table 4.5 presents the recovery values of the measurements of 80 µM Cpro in the presence of different concentrations of paracetamol. The recovery values were in the range of 93.09 to 104.9, which is in the acceptable range.

Table 4. 5: The added, measured, and recovery of Cpro in the presence of different concentrations of paracetamol

| Cpro (µM) | Added paracetamol (µM) | Measured Cpro (µM) | % recovery |
|---|---|---|---|
| **0.0** | 80.0 | ----- | -------- |
| **80.0** | 40.0 | 74.7 | 93.1 |
| **80.0** | 160.0 | 80.7 | 100.9 |
| **80.0** | 240.0 | 84.0 | 104.9 |

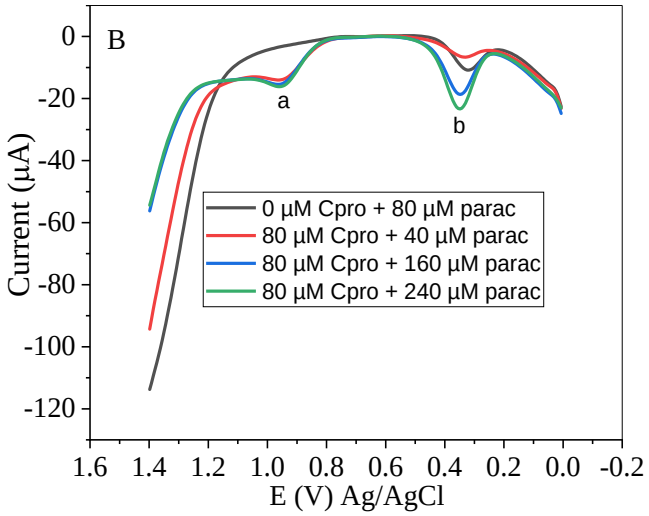


Fig. 4. 24: Background corrected SWVs of pH 7.5 ABS containing (80 µM Cpro + 0 parac), (80 µM Cpro + 40 µM parac), (80 µM Cpro + 160 µM parac), and (80 µM Cpro + 240 µM parac); peak (a) is Cpro, and peak (b) is paracetamol at step potential 6 $mVs^{-1}$, amplitude 35 mV, and frequency 30 Hz using poly $[Mn(Chr)_3]Cl_2$/PGE.

### 4.1.15. Repeatability

In order to test the developed method repeatability, 0.5 mM Cpro has been measured six times using $[Mn(Chr)_3]Cl_2$/PGE, and the result is shown in Fig. 4.25. The standard deviation of the repeatability of $[Mn(Chr)_3]Cl_2$/PGE was 0.767, and the relative standard deviation was calculated to be 1.66 %. This result shows the developed method was repeatable for measuring Cpro with high precision.

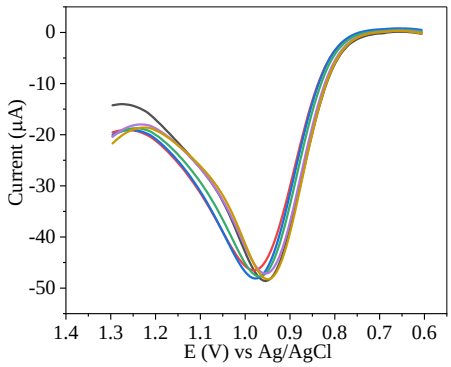


Fig.4.25: reputability of the developed method using 0.5 mM Cpro and $[Mn(Chr)_3]Cl_2$/PGE at step potential 6 $mVs^{-1}$, amplitude 35 mV, and frequency 30 Hz.

### 4.1.16. Comparison with Literature Values

The performance of the developed method with the new modifier for the determination of Cpro has been compared with previously reported literature in terms of the modifier used, dynamic range, limit of detection, and type of electrode used. As seen in Table 6, the present method has a relatively wider dynamic range and lower detection limit. Therefore, the developed method is promising for the determination of ciprofloxacin in pharmaceuticals and biological samples.

Table 4. 6: Comparison of different literature values reported for the determination of Cpro

| Electrode used | Technique | Modifier | Dynamic range (µM) | LoD (µM) | Reference |
|---|---|---|---|---|---|
| **GCE** | DPV | eCNF/CNT/NiCo/GCE | 0.025-0.3 | 6.0 | **[184]** |
| **BDD** | SWV | Pretreated BDD | 2.5-50 | 2.46 | [185] |
| **PGE** | DPV | MIP/ppy/PGE | 50-5000 | 11.2 | [186] |
| **PGE** | SWV | Bare PGE | 12-55 | 5.6 | [53] |
| **PGE** | SWV | $[Mn(Chr)_3]Cl_2$/PGE | 1-200 | 0.536 | This work |

## 4.2. Comparison of Methods for Detecting Ciprofloxacin in Pharmaceuticals and Urine Samples: UV-Vis Spectrophotometry vs. Poly ($[Mn(Chr)_3]Cl_2$)/PGE Voltammetry

Different scholars state that, 'electrochemistry with modified working electrode has better performance than UV-Vis spectrophotometry [187]. However, none of them conducted analysis of Cpro using electrochemical techniques and made a comparative study with UV-Vis spectrophotometric techniques by using same samples and standard solutions.

In this work, Cpro has been determined in pharmaceutical formulations and urine samples using poly (manganese (II)-chrysin complex ($[Mn(Chr)_3]Cl_2$) modified pencil graphite electrode based square wave voltametric (SWV) electrochemical method and UV-Vis spectrophotometric method. The performance of poly($[Mn(Chr)_3Cl_2$)/PGE based developed electrochemical method was tested using $[Fe(CN)6]^{-3/-4}$ and Cpro as a probe and the result was discussed as follows.

### 4.2.1. Performance of the Developed Method Using $[Fe(CN)6]^{-3/-4}$ as a Probe

The electro-activity of poly ($[Mn(Chr)_3]Cl_2$)/PGE modified working electrode with reference to the bare pencil graphite working electrode were examined in terms of electro-active surface area at different scan rate and peak current enhancement. The effective surface area of the modified working electrode showed approximately 3.0 times higher than that of the unmodified PGE electrode [154]. The current enhancement of poly ($[Mn(Chr)_3]Cl_2$)/PGE modified pencil working electrode using 10.0 mM $[Fe\ (CN)\ _6]^{-3/-4}$ as a probe and 0.1 M KCl solution as supporting electrolyte was observed as shown in Fig. 4.26 as compared to the bare electrode. The anodic peak current of the modified electrode was 2.3 times higher than the current of the unmodified pencil electrode. The current enhancement confirms the performance of the modified electrode was increased.

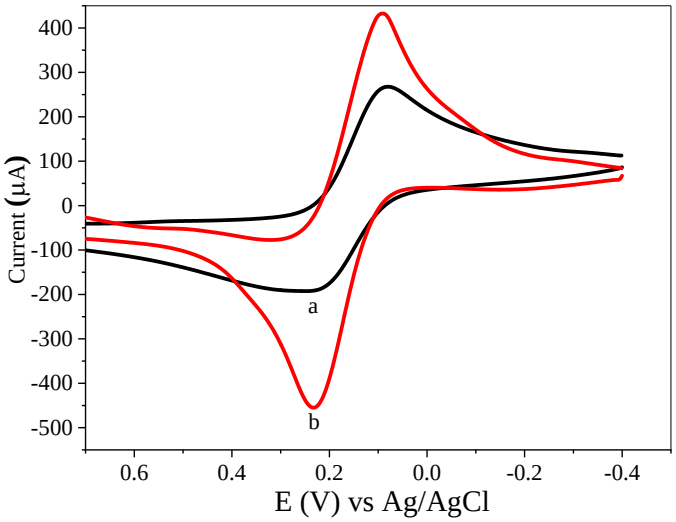


Fig. 4. 26: CV of blank subtracted 10.0 mM $[Fe(CN)_6]^{-3/-4}$ in 0.1 M KCl (a) bare PGE and (b) poly $([Mn(Chr)_3]Cl_2)$/PGE at scan rate 100 $mVs^{-1}$

### 4.2.2. Performance of the Developed Method using Cpro as a Probe

The electro-activity of Cpro at the poly $([Mn(Chr)_3]Cl_2)$/PGE modified pencil working electrode and bare pencil working electrode has been tested using CV and SWV techniques. The oxidative peak of Cpro at poly $([Mn(Chr)_3]Cl_2)$/PGE (Fig. 4.27A) is about eightfold in CV and about threefold of current enhancement in SWV (Fig. 4.27B) compared to bare electrode. The significant current enhancement and reduced potential compared to the oxidative peak at bare PGE (Fig. 4.27B) indicates poly $([Mn(Chr)_3]Cl_2)$/PGE film has a catalytic role in the oxidation of Cpro and has good electro-activity towards oxidation of Cpro.

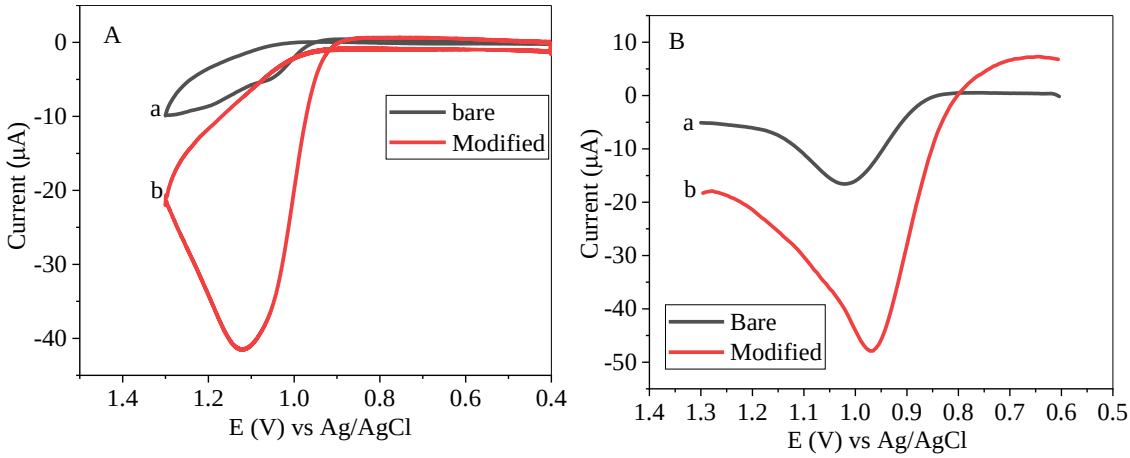


Fig. 4. 27: The CV (A) and SWV (B) of (a) bare PGE and (b) poly ($[Mn(Chr)_3]Cl_2$)/PGE containing 0.5 mM Cpro in pH 7.5 ABS

### 4.2.3. Calibration Curve of UV-Vis Spectrophotometry and SWV

In order to determine Cpro in real samples, the developed poly ($[Mn(Chr)_3]Cl_2$)/PGE modified working electrode method and UV-Vis spectrophotometric methods were calibrated using standard solution of Cpro in the concentration range of 1-250 µM. As shown in Fig. 4.28, as the concentration increases the voltammogram of SWV (Fig. 4.28i) using the modified pencil electrode is also increasing in the concentration range and has a single (one) peak. However, the characteristic peak of Cpro in the absorption band of UV-Vis appeared three peaks as shown in Fig. Fig. 4.28 (ii) (peakA, B, and C) and this is supported by [188]. As shown in Fig. 4.28(ii) peak (A) is not further increasing beyond the concentration of 160 µM. But the absorption band for peak (B) and peak (C) are increased in the concentration range as shown in Fig. 4.28(ii).

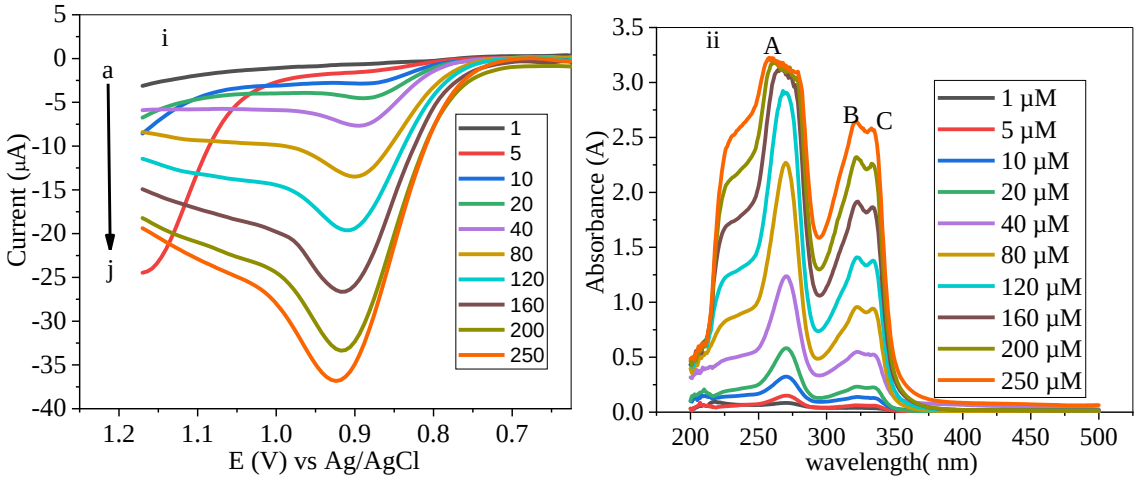


Fig. 4. 28: Voltammogram of the calibration curve of Cpro at various concentration (i) and UV-Vis absorption band (ii) of the same concentration

As shows in Fig. 4.29, the plot of absorbance vs concentration for the three peaks of Fig. 4.29(ii) (A, B, and C) in the absorption band of UV-Vis spectra. Peak A is linearly increased in the range from 1-120 μM and lost its linearity beyond 120 μM. However, peak B and C are linear in the concentration range of 1 μM -250 μM. All the three peaks, the calibration curve is commonly linear in the concentration range of 1-120 μM.

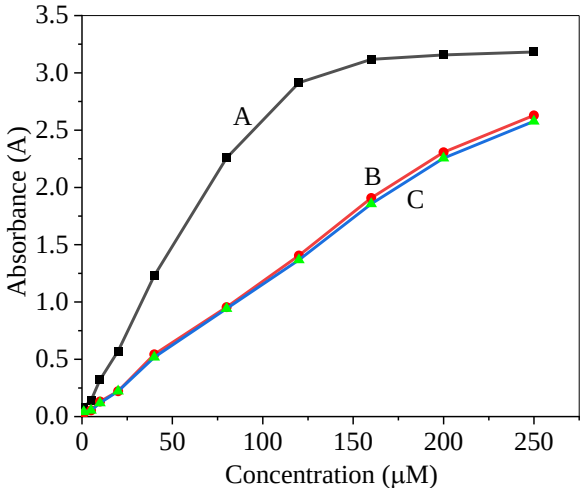


Fig. 4. 29: the plot of absorbance vs concentration for the three peaks in the absorption band of UV-Vis spectara

Fig: 30 show the absorption band of Cpro in its linear range from 1-120 μM. As shown, all the three absorption bands are increasing in the concentration range. Therefore, the

absorption band in the concentration range of 1-120 µM was set as the calibration of UV-Vis for the determination of Cpro in human urine and pharmaceutical tablet samples.

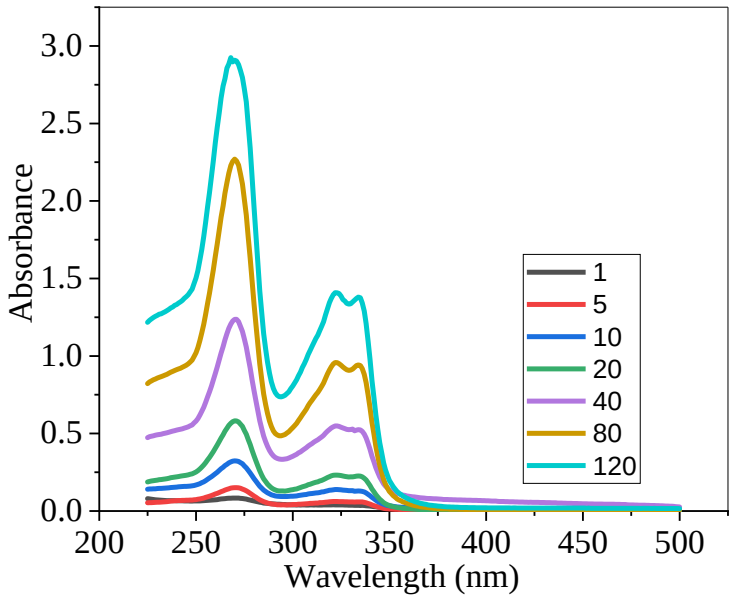


Fig. 4. 30: the absorption band of Cpro in the concentration range of 1-120 µM in ABS at pH 7.5

The calibration curve of Cpro using SWV with poly ($[Mn(Chr)_3]Cl_2$)/PGE modified electrode Fig. 4.28(i) and UV-Vis Fig. 4.28(ii) (A (1-120 µM), B, and C) in ABS at pH 7.5 is shown in Fig. 4.31. As shown, the slope of the calibration curve (i), ii (A), ii (B), and ii (C) were -0.148, 0.02479, 0.0109, and 0.01071, respectively. The slope value of the calibration curve is related to the sensitivity of the method. Therefore, 0.148 greater than from other UV-Vis slopes. The ratio of slope of (i) which is the slope of SWV of poly ($[Mn(Chr)_3]Cl_2$)/PGE to the slope of Cpro in UV-Vis spectrum ii(A) was closer to 6. The value of the ratio confirms poly ($[Mn(Chr)_3]Cl_2$)/PGE based developed square wave voltammetric electrochemical method was 6 times more sensitive than the UV-Vis spectrophotometry for the determination of Cpro in real samples.

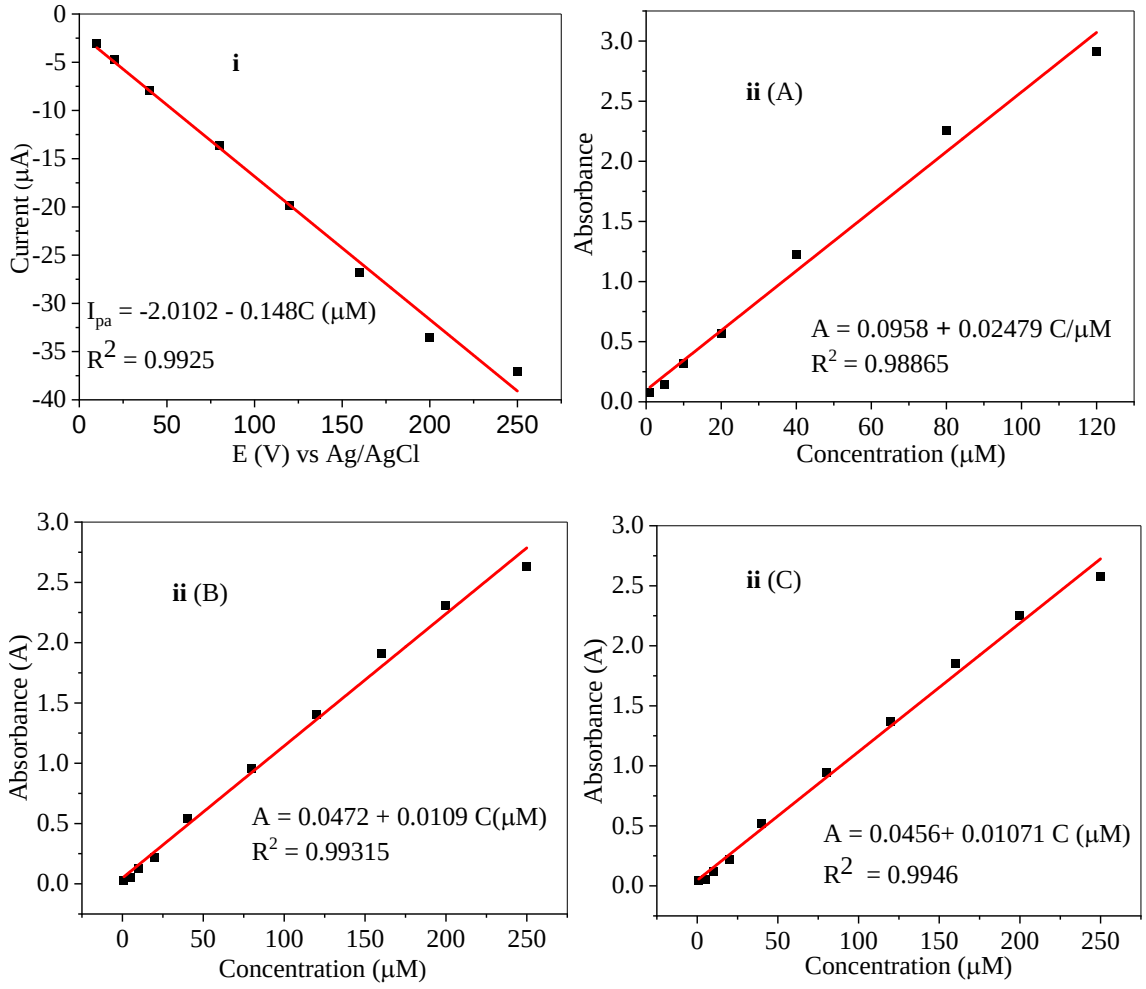


Fig. 4. 31: The plot of the calibration curve of Cpro using SWV with ($[Mn(Chr)_3]Cl_2$) (i) and UV-Vis ii (A, B, and C) in ABS at pH 7.5

### 4.2.4. Real Sample Analysis

#### 4.2.4.1.Human Urine Sample Analysis

Human urine sample analysis was carried out by taking un-spiked and spiked with 20 μM, 40 μM, and 60 μM of Cpro and the result was plotted as shown in Fig. 4.32. Poly ($[Mn(Chr)_3]Cl_2$)/PGE based SWV shown at Fig. 4.32(ii) confirms the presence of characteristic peaks of Cpro and Uric acid in the spiked urine sample. The developed method was able to analysis Cpro in urine sample matrix selectively. In Fig. 4.32(ii) peak 'a' which is the characteristic peak of Cpro increases with concentration of Cpro but peak 'b' and peak 'c' is not increasing with concentration of Cpro which conform, Cpro is not

affected by the urine sample matrices and uric acid is not affected by the presence of Cpro. Therefore the developed method can selectively detect Cpro in urine sample. The same human urine sample solution and with same treatment was analyzed using UV-Vis spectrophotometric method of analysis and the resulting spectra is shown in Fig. 4.32(i). There was no well peak separation between characteristic peak of uric acid and Cpro. But the third peak of Cpro at the wavelength 334 nm can help to predict the concentration of Cpro.

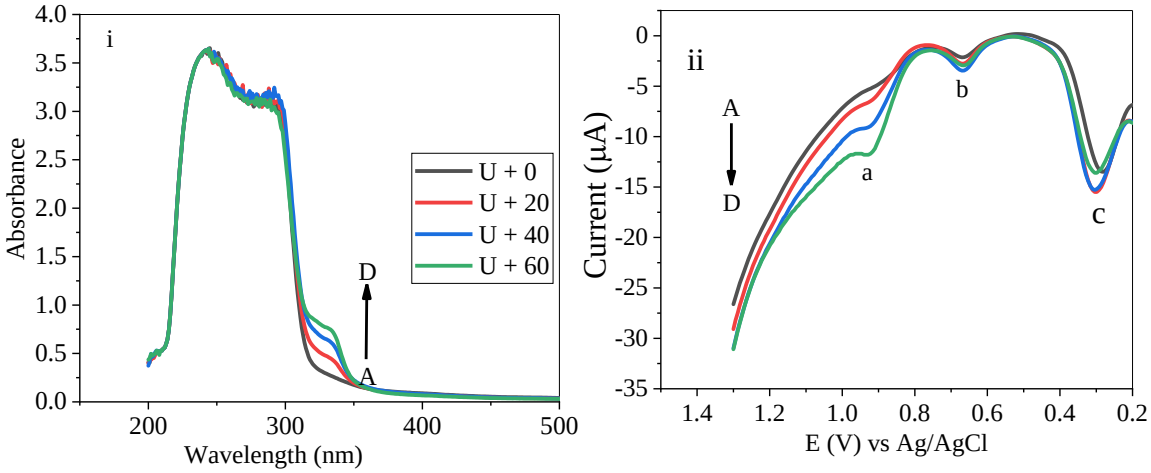


Fig. 4. 32: Background corrected UV-Vis spectra (i) and SWVs of pH 7.5 ABS (ii) containing (A) un-spiked urine sample, (B) (urine + 20 µM), (C) (urine + 40 µM), and (D) (urine + 60 µM); peak a, b, and c of (ii) represents Cpro, creatinine and Uric acid respectively.

Table 4.7 presents the measured and recovery results of SWV using poly ($[Mn(Chr)_3]Cl_2$)/PGE and UV-Vis spectrophotometry methods in urine sample. The range of the recovery of SWV and UV-Vis were from 92.83–114.9 and 86.12-111.75, respectively. The range of the recovery results were in the acceptable range, suggesting that the proposed method can be used to determine Cpro in urine samples in an efficient manner.

Table 4. 7: Recovery results of Cpro in human urine samples using poly ($[Mn(Chr)_3]Cl_2$)/PGE based SWV and UV-Vis spectrophotometry

| Un-spiked | Added Cpro (µM) | Found (µM) | | % recovery | |
|---|---|---|---|---|---|
| | | SWV | UV-Vis | SWV | UV-Vis |
| ND | 20.0 | 23.0 ± 0.6 | 22.35 ± 0.2 | 115.0 | 111.75 |
| ND | 40.0 | 38.9 ± 0.8 | 39.35 ± 0.6 | 97.4 | 98.38 |
| ND | 60.0 | 55.7 ± 1.02 | 51.67 ± 0.3 | 92.8 | 86.12 |
| ND: not detected | | | | | |

### 4.2.4.2.Tablet Sample from Two Brands

Cpro was determined in the pharmaceutical tablets of two brands available in the local market sing poly ($[Mn(Chr)_3]Cl_2$)/PGE modified pencil electrode based SWV technique and UV-Vis spectrophotometric method. To examine the validity of the developed method for the determination of Cpro in pharmaceutical formulation samples and UV-Vis spectrophotometric method, recovery analysis was conducted. The recovery was conducted by spiking 40.0 µM, 80.0 µM, and 120.0 µM Cpro standard solution in nominal concentration of 80.0 µM Ciproscot and Zindolin brand samples. The resulting peak current and absorption band is shown in Fig. 4.33(A, B, A', and B').

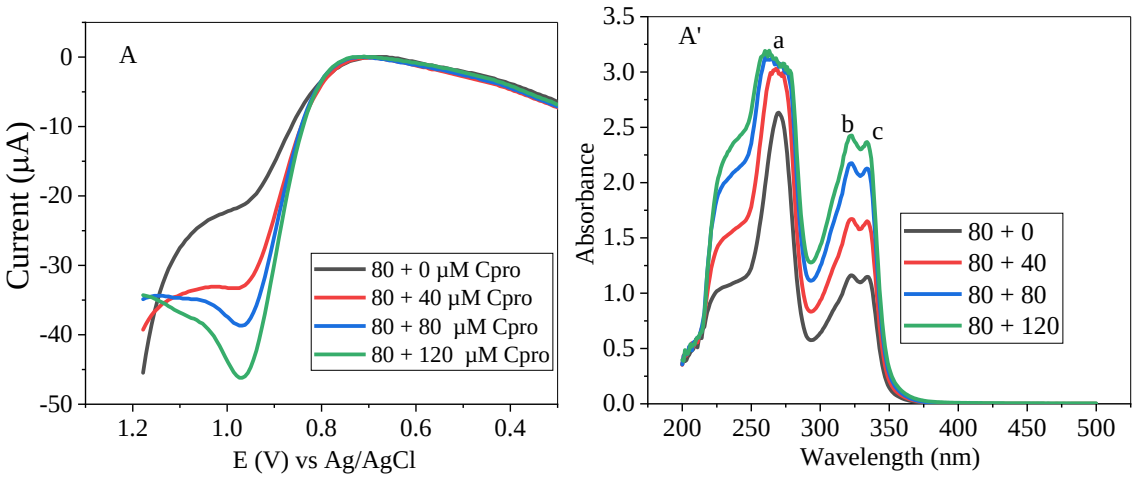

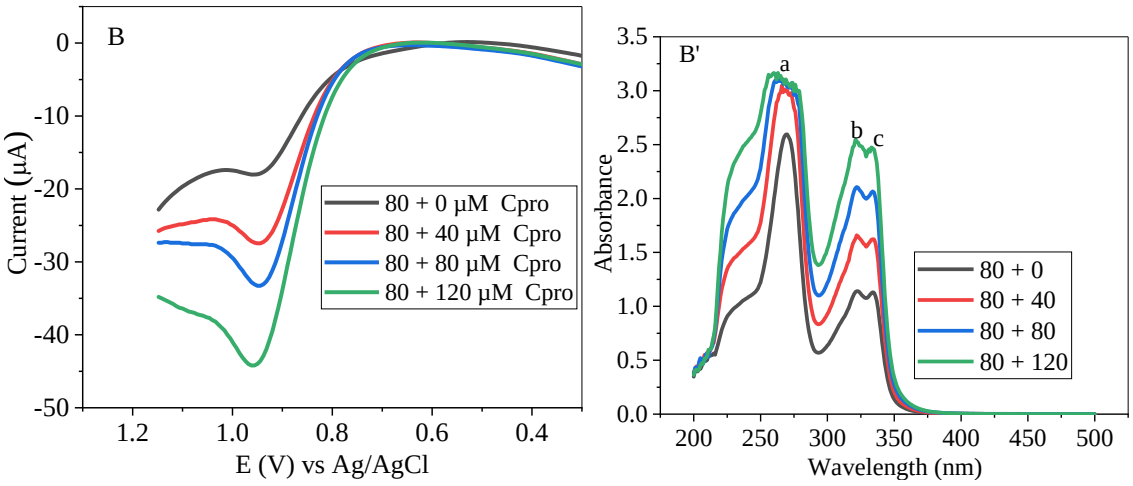


Fig. 4. 33: Background corrected poly ($[Mn(Chr)_3]Cl_2$)/PGE based SWV of Ciproscot (A) and Zindolin (B) brand pharmaceutical tablet samples and their corresponding UV-Vis absorption band A' and B' respectively spiked with various concentrations of standard Cpro ((80.0 +0.0), (80.0 + 40.0), (80.0 + 80.0), and (80.0 + 120.0)) in ABS at pH 7.5

To predict the measured value in UV-Vis spectrophotometric method, Fig. 4.33B' peak (b) was used in both Fig. 4.33A' and B' and the results were presented in Table 4.8. The recovery results of SWV using poly ($[Mn(Chr)_3]Cl_2$)/PGE and UV-Vis spectrophotometric methods were in the range of 84.5–114.25 and 103.8-115.3, respectively. The range of the recovery results were in the acceptable range, suggesting that the proposed method can be used to determine Cpro in pharmaceutical samples in an efficient manner.

Table 4. 8: Recovery results of Cpro in each tablet brand samples using both SWV using poly ($[Mn(Chr)_3]Cl_2$)/PGE and UV-Vis spectrophotometry methods (mean ± %R ).

| Brand tablets | Un - spike (µM) | Amount in (µM) | | Measured amount (µM) | | % recovery | |
|---|---|---|---|---|---|---|---|
| | | Added | Expected | SWV | UV-Vis | SWV | UV-Vis |
| Ciproscot | 80 | 0.0 | 80 | 67.6 ± 1.3 | 91.5 ± 0.2 | 84.5 | 114.3 |
| | 80 | 40 | 120 | 135.0 ± 2.2 | 138.2 ± 0.2 | 112.2 | 115.2 |
| | 80 | 80 | 160 | 170.1 ± 2.1 | 184.4 ± 0.1 | 106.3 | 115.3 |
| | 80 | 120 | 200 | 218.0 ± 1.3 | 207.7 ± 0.5 | 108.9 | 103.8 |

| | | | | | | | |
|---|---|---|---|---|---|---|---|
| Zindolin | 80 | 0.0 | 80 | 73.9 ± 1.7 | 90.1 ± 0.4 | 92.3 | 112.6 |
| | 80 | 40 | 120 | 124.2 ± 2.3 | 136.7 ± 0.3 | 103.5 | 113.9 |
| | 80 | 80 | 160 | 163.3 ± 1.5 | 178.2 ± 0.1 | 102.1 | 111.4 |
| | 80 | 120 | 200 | 228.5 ± 2.6 | 218.2 ± 0.6 | 114.3 | 109.1 |

### 4.2.4.3.Selectivity of the Method

The selectivity of the developed poly ($[Mn(Chr)_3]Cl_2$)/PGE based SWV method and UV-Vis spectrophotometric method has been evaluated in the presence of paracetamol. The impact was investigated at different concentrations of paracetamol by maintaining concentration of Cpro constant at 80 µM. The characteristic peak of Cpro and paracetamol appear separately in the developed poly ($[Mn(Chr)_3]Cl_2$)/PGE based SWV method as shown in Fig. 4.34(i) peak (a) and (b). Characteristic peak of Cpro remains constant with some variation as the concentration of paracetamol rises indicated in Fig. 4.34(i) peak (a). Whereas the characteristic peak of paracetamol increases as the concentration of paracetamol increases as shown in Fig. 4.34(i) peak (b). Therefore, the newly developed method can determine Cpro selectively in the presence of paracetamol. However, in the case of UV-Vis spectrophotometric method, the characteristic peak of Cpro and characteristic peak of paracetamol was not resolved well. The characteristic peak of Cpro rises as the concentration of paracetamol increases as shown in Fig. 4.34(ii) peak (b). Therefore using UV-Vis spectrophotometric method, it is difficult to determine Cpro selectively in the presence of paracetamol.

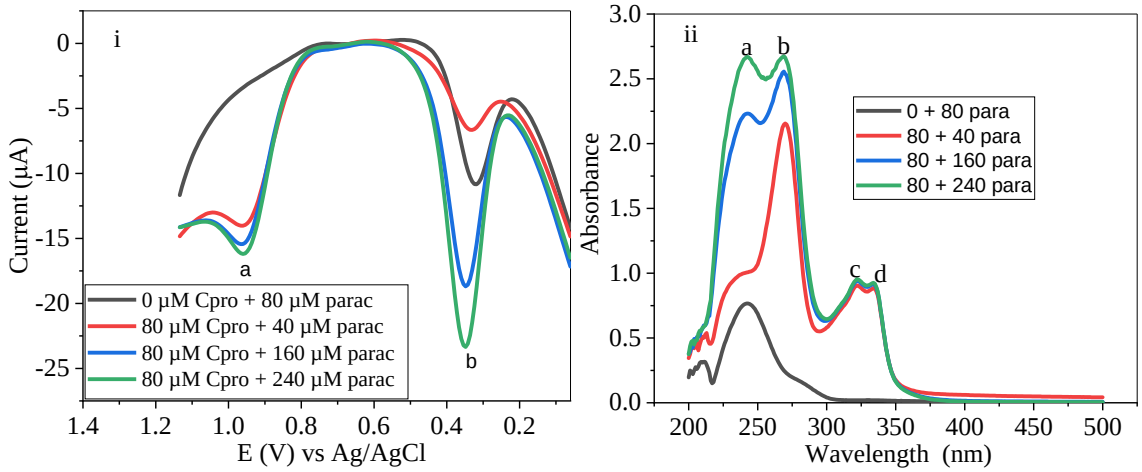

Fig. 4. 34: Plot of background corrected SWV (i) and UV-Vis absorption band (ii) of pH 7.5 ABS containing ( 80 para + 0 µM Cpro), (40 µM para + 80 µM Cpro), (160 µM para + 80 µM Cpro), and (240 µM para + 80 µM Cpro)); peak i (a) and peak i (b) are peak of Cpro and paracetamol respectively.

The poly ($[Mn(Chr)_3]Cl_2$)/PGE-based SWV method has a wider linear range, high selectivity, and high sensitivity than the UV-Vis spectrophotometric method of analysis for the determination of Cpro in pharmaceuticals and urine samples. The comparison has been made using different parameters between the two methods as indicated in Table 4.9.

Table 4. 9: Comparison of poly ($[Mn(Chr)_3]Cl_2$)/PGE based SWV and UV-Vis spectrophotometric method in different parameters in the determination of Cpro

| Methods | Poly($[Mn(Chr)_3]Cl_2$)/PGE based SWV method | UV-Vis spectrophotometric method |
|---|---|---|
| **Dynamic range (µM)** | 1-250 | 1- 120 |
| **LoD (µM)** | 0.536 | 0.413 |
| **Selectivity** | Selective | Not selective |
| **Sensitivity** | 0.148 | 0.025 |
| **Speed of measurement** | Less faster | faster |

## 4.3. Characterization, and Application of poly [Cu(Chr)$_2$Cl]Cl/PGE Based Electrochemical Sensor for the Determination of Norfloxacin in Pharmaceuticals and Milk Samples

### 4.3.1. Characterization of the Complex

#### 4.3.1.1.Physicochemical Characterizations

The complex is greenish yellow and is soluble in acetonitrile and dimethyl sulfoxide. It is insoluble in chloroform, water, and tetrahydrofuran. The complex can be formulated as [Cu(Chr)$_2$Cl)Cl]. Found: Cu –7.79%, and Cl –8.83%; Calculated Cu –7.99%, and Cl –8.92%. This data reveals that the complex can be represented as [Cu(Chr)$_2$Cl)Cl].

#### 4.3.1.2.UV-Vis Spectroscopy Characterization

Electronic spectra showed Chrysin's π→π* (291 nm Fig. 4.35(B) to 260 nm Fig. 4.35(C)) and n→π* (312 nm Fig. 4.35(B) to 315 nm Fig. 4.35(C)) shifting upon complexation. Moreover, the twine bands of the salt at 551 nm and 569 nm corresponding to $^2B_{1g} \rightarrow {}^2B_{2g}$ and $^2B_{1g} \rightarrow {}^2E_g$ Fig. 4.35(A), respectively, disappeared in [Cu(Chr)$_2$Cl]Cl , indicating a geometry change after the coordination of chrysin [189].

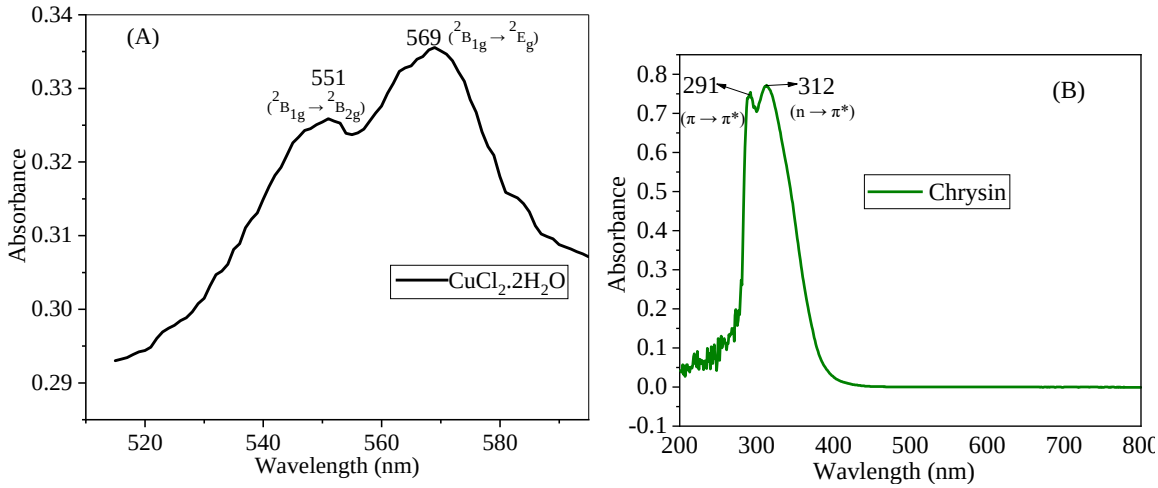

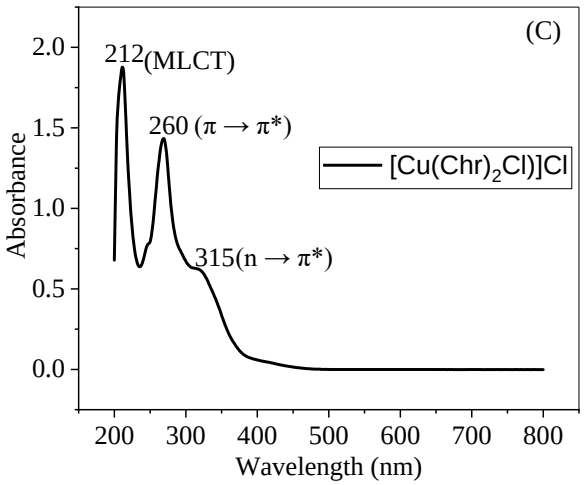


Fig. 4. 35: UV-Vis spectra of $CuCl_2.2H_2O$ (A), Chrysin (B), and the complex (C)

### 4.3.1.3.FT-IR Spectra

Coordination of chrysin was confirmed by the appearance of new bands at 423 $cm^{-1}$ and 397 $cm^{-1}$ assigned to Cu–OH and Cu-O=C (Fig. 4.36(B)), respectively. Furthermore, the shifts in characteristic phenolic C–O stretch from 1165 $cm^{-1}$(A) (free ligand) to 1171 $cm^{-1}$(B) and carbonyl C=O stretch from 1607 $cm^{-1}$ to 1615 $cm^{-1}$ indicate the change in the electronic environment following the coordination relative to Fig. 4.36(A).

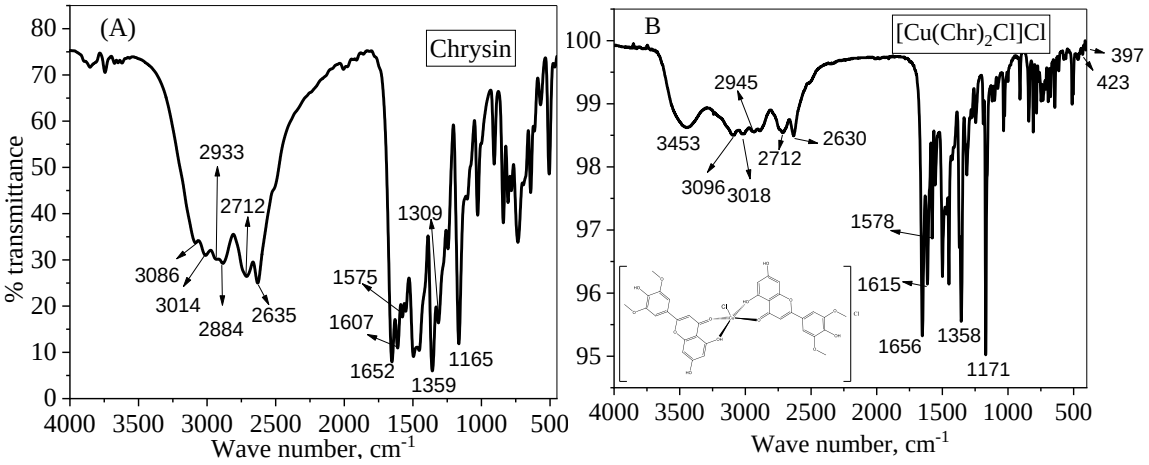


Fig. 4. 36: FTIR spectra of Chrysin (A) and the complex (B)

The structure and the reaction path of the complex $[Cu(Chr)_2Cl)Cl]$ was proposed as shown in (eq. (4.5)) and (Scheme 4.3).

$$CuCl_2.2H_2O + 2C_{17}H_{14}O_7 \rightarrow [Cu(C_{17}H_{14}O_7)_2Cl]Cl + 2H_2O \quad \text{.....(4.5)}$$

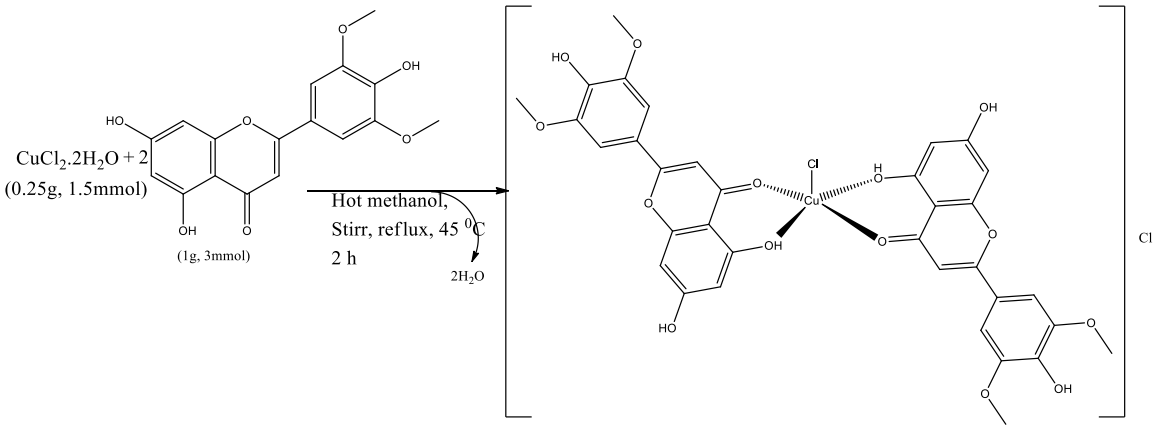


Scheme 4. 3: The proposed synthesis path of the complex

### 4.3.2. Optimization of Potential Window

A potential window, which was required to polymerize 1.0 mM $[Cu(Chr)_2Cl]Cl$ monomer on the surface of pencil graphite electrode was optimized by using different potential windows (0.0 & 1.8, -0.4 & 1.8, -0.8 & 1.8, -1.2 & 1.8, and -1.6 & 1.8) at 15 scan cycle. Then the resulting current intensity in the voltammogram of 500 µM Nor for each of the potential window were compared [190]. The potential window that provided the highest current intensity was optimized. As shown in Fig. 4.37, the synthesized poly $[Cu(Chr)_2Cl]Cl$/PGE in the potential window of (-0.4 & 1.8) provided the highest anodic peak current compared to the others. Therefore, -0.4 & 1.8 was optimized as a potential window to synthesized poly $[Cu(Chr)_2Cl]Cl$/PGE on the surface of pencil graphite electrode for the determination of Nor in milk samples and pharmaceuticals.

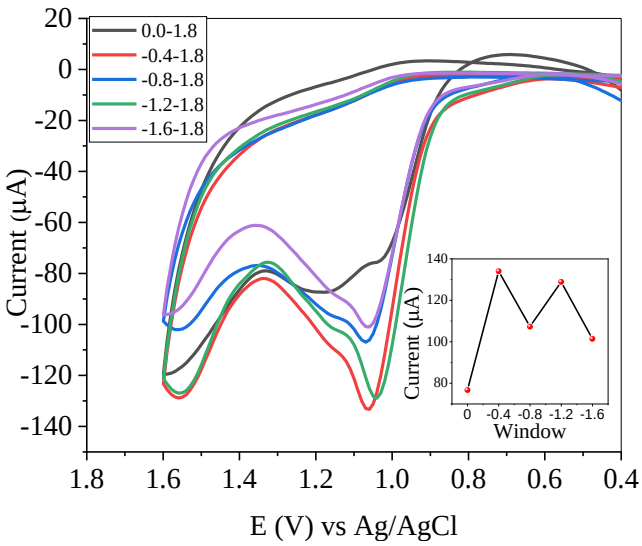


Fig. 4. 37: CV of 500 µM Nor in pH 7.0 PBS using poly $[Cu(Chr)_2Cl]Cl$/PGE synthesized in different potential window (0.0 & 1.8, -0.4 & 1.8, -0.8 & 1.8, -1.2 & 1.8, and -1.6 & 1.8) at 15 scan cycle and at 100 $mVs^{-1}$ scan rate Inset: Plot of absolute value of current vs potential window

### 4.3.3. Optimization of Film Thickness

Poly $[Cu(Chr)_2Cl]Cl$/PGE was synthesized in different scan cycles (4, 8, 12, 16, and 20) and used to measure the current response of 500 µM Nor in pH 7.0 PBS [191]. As shown in Fig. 4.38, Poly $[Cu(Chr)_2Cl]Cl$/PGE which was synthesized at 12 scan cycles and in the potential window -0.4 & 1.8 provided most intense peak. It was also shown in the inset. As a result, scan cycles at 12 was selected as the optimized scan cycles for the synthesis of Poly $[Cu(Chr)_2Cl]Cl$/PGE for the determination of Nor in real samples and pharmaceuticals.

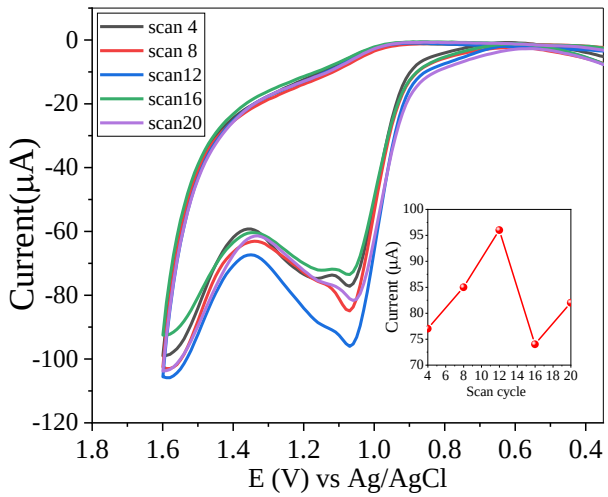


Fig. 4. 38: CV of 500 µM Nor in pH 7.0 PBS using poly $[Cu(Chr)_2Cl]Cl$/PGE synthesized in different scan cycles (4, 8, 12, 16, and 20) in the potential window -0.4 & 1.8 and at 100 $mVs^{-1}$ scan rate Inset: Plot of absolute value of current vs Scan cycle

### 4.3.4. Synthesis of poly $[Cu(Chr)_2Cl]Cl$/PGE

Poly $[Cu(Chr)_2Cl]Cl$/PGE has been synthesized using the optimized potential window and number of scan cycles for every analysis, and the voltammogram of the synthesis is shown in Fig. 4.39A. As shown in the Fig. 4.39A, different peaks were appearing which indicates the presence of growth of film on the surface of pencil graphite electrode. The synthesized modifier has been stabilized and washed using 0.5 M $H_2SO_4$ in the potential range of -0.8 & 0.8 for 8 scan cycles at 100 scan rate and the voltammogram was shown Fig. 4.39B(ii). The stabilization of bare pencil graphite electrode has also been performed using 0.5 M $H_2SO_4$ in the potential range of -0.8 & 0.8 for 8 scan cycles at 100 scan rate and the voltammogram was shown in Fig. 4.39B(i). As shown in Fig. 4.39B, the peak intensity in the stabilization of poly$[Cu(Chr)_2Cl]Cl$/PGE using $H_2SO_4$ was increased more than 40 times than bare PGE which confirms the electroactivity of the modified electrode was improved[182]. This is due to the fast electron transfer between the coated thin film in the modified electrode and the electroactive species in a solution than the unmodified electrode.

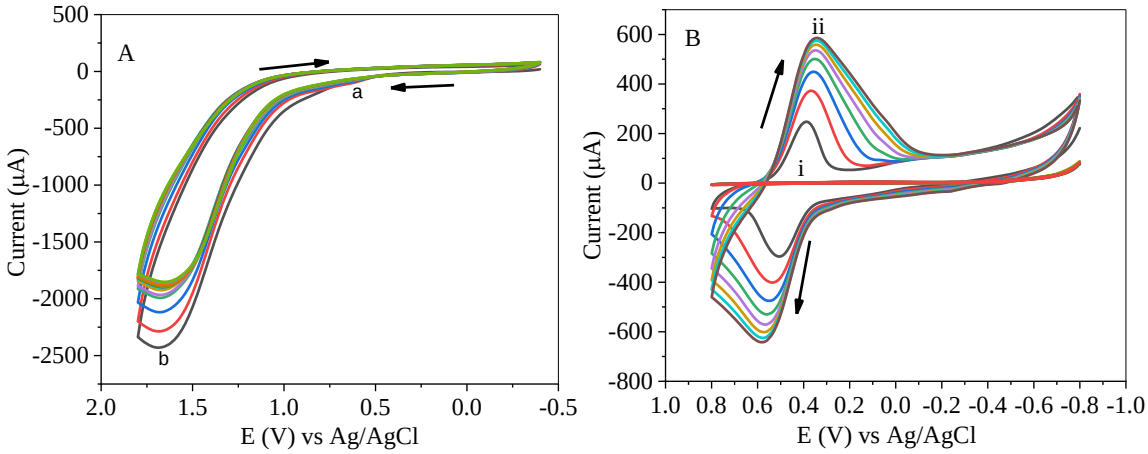


Fig. 4. 39: CVs of (A) 1.0 mM $[Cu(Chr)_2Cl]Cl$/PGE scanned between -0.4 – 1.8 for 12 scan cycles at 100 $mVs^{-1}$ scan rate and (B) CVs of 0.5 M $H_2SO_4$ (i) bare PGE and (ii) poly$[Cu(Chr)_2(Cl)]Cl$/PGE scanned between -0.8 and 0.8 for 8 scan cycles at 100 $mVs^{-1}$

### 4.3.5. Characterization of the Synthesized Electrode

#### 4.3.5.1. Cyclic Voltammetry Characterization of poly $[Cu(Chr)_2Cl]Cl$/PGE

Cyclic voltammetry was used to characterize the synthesized electrode using 10.0 mM $[Fe(CN)_6]^{-3/-4}$ as a probe in 0.1 M KCl relative to the bare PGE electrode [191]. As shown in Fig. 4.40(b), the anodic peak current was 2(two) times higher than the unmodified anodic peak current (Fig. 4.40(a)) and the change in peak potential between anodic peak potential of bare and modified was 96.84 mV. This peak current enhancement and shift of peak potential towards lower anodic potential, confirms the deposition of electoactive modifier on the surface of the pencil graphite electrode.

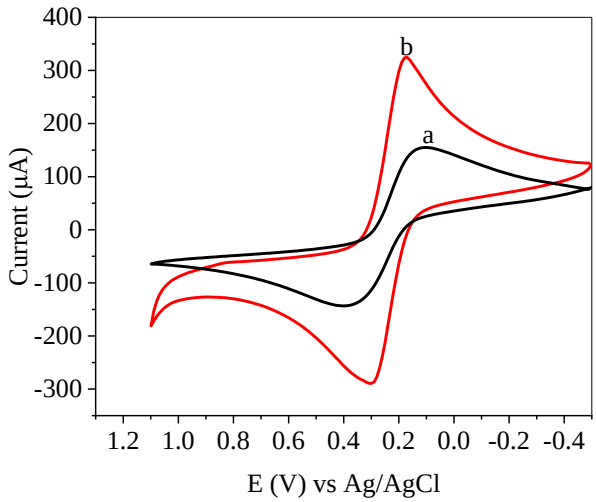


Fig. 4. 40: CVs of 10.0 mM $[Fe(CN)_6]^{-3/-4}$ in 0.1 M KCl (a) bare PGE and (b) poly $[Cu(Chr)_2Cl]Cl$/PGE at 100 $mVs^{-1}$

The effective electroactive surface area was examined by measuring and plotting the voltammogram of 10.0 mM $[Fe(CN)_6]^{-3/-4}$ in 0.1 M KCl at various scan rate (15- 300 mV/s) using both bare and modified electrode. The effective surface area was calculated using Randles-sevick equation (4.6) and the slope values of the plots of current versus square root of scan rate as shown in the inset of Fig. 4.41(A and B) both for bare and modified electrode respectively.

$$I_{pa} = 2.69 \times 10^5 \times n^{3/2} A D^{1/2} V^{1/2} C_o \quad \ldots\ldots (4.6)$$

Where: $I_{pa}$ is the peak current, A is the effective surface area ($cm^2$), n = number of electrons involved during redox reaction for $[Fe(CN)_6]^{-3/-4}$(n = 1), D is the diffusion coefficient of $[Fe(CN)_6]^{-3/-4}$ (D = 7.6 x $10^{-6}$ $cm^2s^{-1}$), *v* is the scan rate (mV/s), and $C_o$ is the concentration of $[Fe(CN)_6]^{-3/-4}$ (10.0 mM).

The effective electroactive surface area of poly $[Cu(Chr)_2Cl]Cl$/PGE was calculated to be 0.43 $cm^2$, and the bare PGE was calculated to be 0.23 $cm^2$. The value of the calculated effective electroactive surface area of poly $[Cu(Chr)_2Cl]Cl$/PGE is roughly 2.0 times higher than the surface area of the bare PGE electrode. Area enhancement in the modified electrode confirms the effective modification of PGE electrode[192].

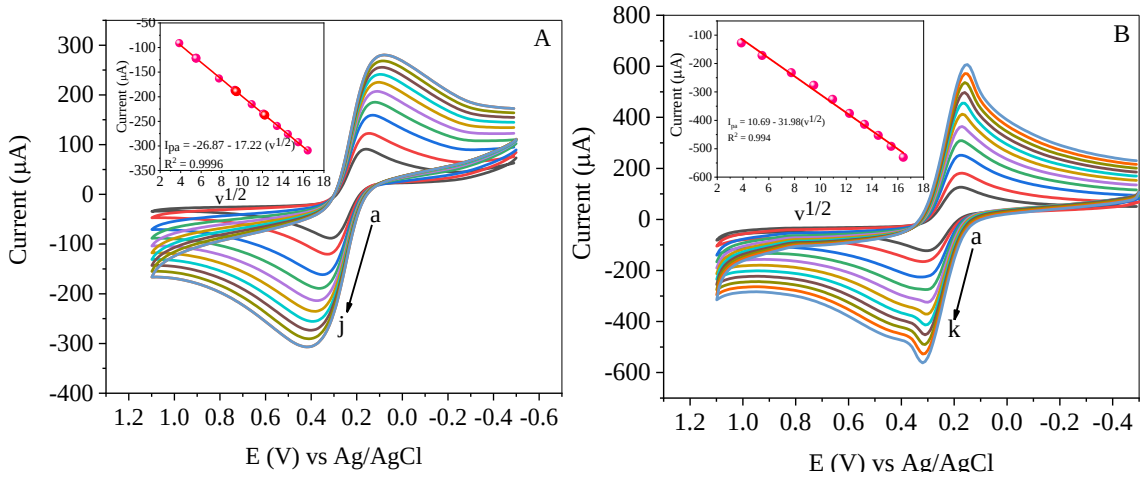


Fig. 4. 41: CVs of 10.0 mM $[Fe(CN)_6]^{-3/-4}$ in 0.1 M KCl (A) bare PGE and (B) poly $[Cu(Chr)_2Cl]Cl$/PGE at different scan rate (15, 30, 60, 90, 120, 150, 180, 210, 240, 270, and 300 $mVs^{-1}$) Insets: plot of current vs square roots of scan rate

### 4.3.5.2.Electrochemical Impedance Spectroscopy

To characterize the modified electrode using EIS, the Nyquist plots were ploted using 10.0 mM $[Fe(CN)_6]^{-3/-4}$ in 0.1 M KCl of bare PGE shown in Fig. 4.42(a) and poly$[Cu(Chr)_2Cl]Cl$/PGE shown in Fig. 4.42(b) in the frequency range of 0.1–1,000,000 Hz, with an amplitude of 0.01 V and at a potential of 0.23 V [193]. As shown in Fig. 4.42, the Nyquist plots show two peak maxima which may due to the presence of lateral and base side surfaces of a pencil deep in a solution. From the Nyquist plot, the charge transfer resistance ($R_{ct}$) reduced by a factor of three compared to the bare electrode. This is ascribed to the increased conductivity of the modified electrode.

The $R_{ct}$ value of poly $[Cu(Chr)_2Cl]Cl$/PGE Fig. 4.42(b) was 166.8Ω, significantly lower than that of bare PGE Fig. 4.42(a), which was 511.2 Ω. This confirms that the electron transfer rate between the modified electrode and the probe ($[Fe(CN)_6]^{-3/-4}$ ) was increased due to modification [173] as summarized in Table 4.10. The double layer capacitance and heterogeneous electron transfer rate constant were calculated using (equation 4.7 and 4.8), respectively, and the value was increased by nearly two times due to modification.

$$C_{dl} = \frac{1}{2\pi R_{ct} f} \text{----------(4.7)}$$

$$K^{o} = \frac{RT}{F^{2}ACR_{ct}} \text{---------- (4.8)}$$

Where: $C_{dl}$-double layer capacitance, $K^{o}$-heterogeneous electron transfer rate constant, $R_{ct}$-charge transfer resistance, A-area, C-concentration, R-ideal gas constant, T-temperature (298 K), $F^{2}$-Faraday's constant, and f-frequency corresponding to the maximum imaginary impedance

Table 4. 10: Values of EIS parameters from the Nyquist plot

| Electrode | Rs ($\Omega$ $cm^2$) | $R_{ct}$ ($\Omega$ $cm^2$) | $K^{o}$ | $C_{dl}$ (F) | f (Hz) |
|---|---|---|---|---|---|
| PGE | 53.7 | 511.2 | $2.26 \times 10^{-7}$ | $1.6 \times 10^{-4}$ | 1.995 |
| Poly $[Cu(Chr)_2Cl]Cl$/PGE | 52.6 | 166.8 | $3.71 \times 10^{-7}$ | $1.9 \times 10^{-3}$ | 0.5 |
| Fitting Error % | 4.467 | 11.53 | - | 18.13 | - |

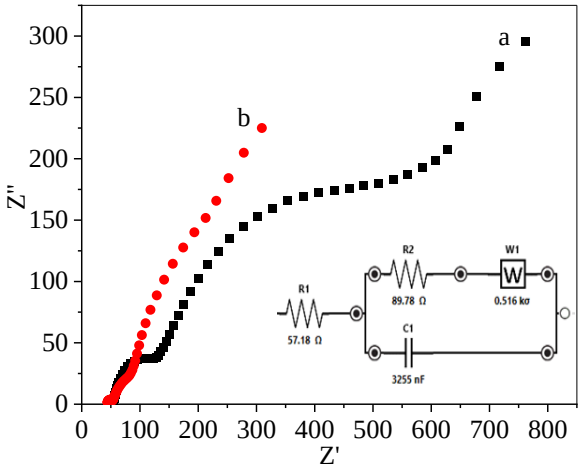


Fig. 4. 42: Nyquist plot of 10.0 mM $[Fe(CN)_6]^{-3/-4}$ in 0.1 M KCl (a) bare PGE and (b) modified by poly $[Cu(Chr)_2Cl]Cl$/PGE in the frequency range: 0.1 – 1,000,000 Hz, amplitude = 0.01 V, and potential = 0.23 V. Inset: equivalent circuit with fitting values

### 4.3.5.3.UV-Vis, Contact Angle, and Digital Optical Microscopy Characterization

The polymerized $[Cu(Chr)_2Cl]Cl$ has been studied by using UV-Vis, contact angle and digital optical microscope characterization methods and using fluorine-doped tin oxide (FTO) as a substrate. FTO has been electropolymerized using a similar

electropolymerization procedure optimized and used in PGE electrode electropolymerization. The UV-Vis absorption spectra and digital optical microscope images were taken from bare FTO and polymerized by $[Cu(Chr)_2Cl]Cl$/FTO as a substrate, and the results are shown in Fig. 4.43A, 4.43B, and 4.43C, respectively. The appearance of a new absorption band in the UV-Vis spectrum (Fig. 4.43Ab) indicated by a circle compared to the bare FTO (Fig. 4.43Aa) confirms the modification of the surface of FTO by poly$[Cu(Chr)_2Cl]Cl$/FTO.

The digital optical microscopic images of the surface of FTO before and after deposition of the polymer were taken at a 5 mm distance and 1800x magnification scale. As shown in Fig 4.43B, the surface of bare FTO was smooth, but the surface of the modified FTO was rough (Fig. 4.43C). The transformation of FTO surface from smooth to rough due to electropolymerization of $[Cu(Chr)_2Cl]Cl$ confirms the deposition of the polymer on the surface of FTO. Since a similar electropolymerization procedure was followed for the deposition of $[Cu(Chr)_2Cl]Cl$ on the surface of the pencil graphite electrode, related deposition and an associated increase in surface roughness were also expected on the pencil graphite electrode, as reported in several research works[154]. The surface of FTO is highly hydrophilic and has wetting properties [194]. In this study, surface wettability of FTO before and after modification by poly$[Cu(Chr)_2Cl]Cl$/FTO was assessed using a contact angle goniometer (DSA25 Drop Shape Analyzer, Krüss, Germany). The result of the contact angle is shown in Fig. 4.43(D and E). As shown, the average contact angle value was increased from 26.4º to 29.9º. This change in contact angle confirms the deposition of less hydrophilic poly$[Cu(Chr)_2Cl]Cl$ polymer film that changes the surface chemistry of FTO.

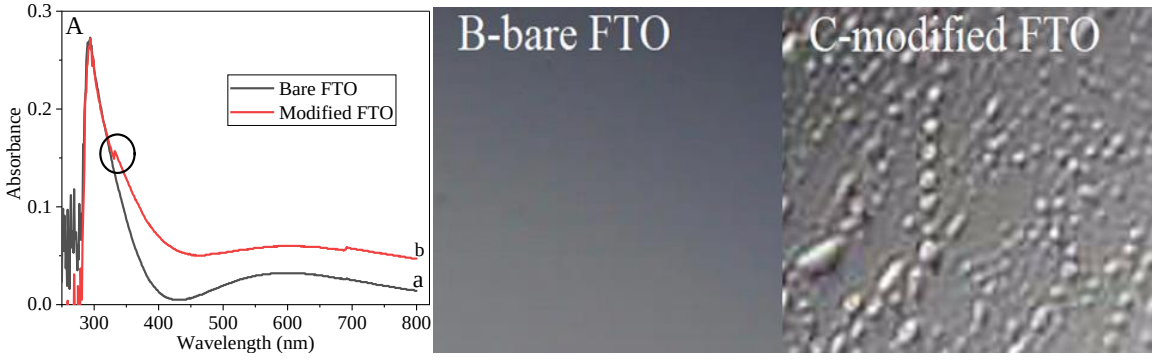

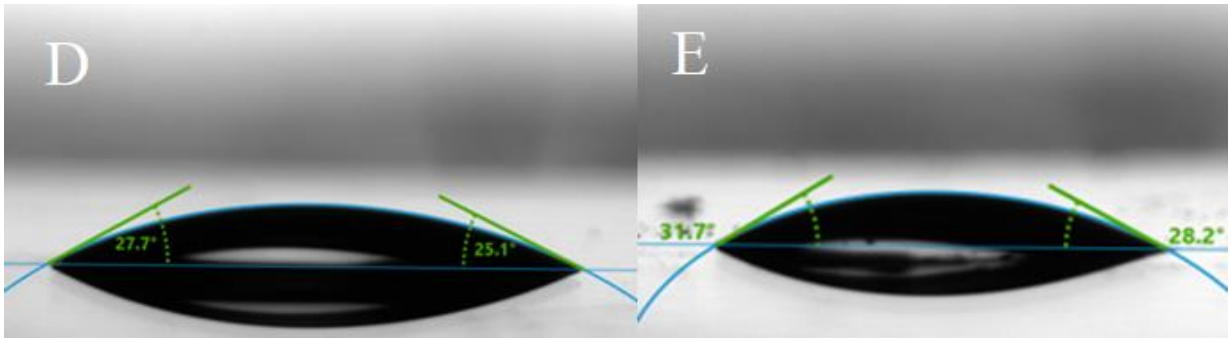


Fig. 4. 43: UV-Vis spectra of poly [Cu(Chr)$_2$Cl]Cl on the surface of FTO (A), digital optical microscopy images at 5 mm distance and 1800x magnification scale (B and C) and water contact angle (D and E);(Aa, B, and D) are using bare FTO and (Ab, C, and E) are using modified FTO .

**4.3.5.4.Electrochemical Properties of Nor**

The electrochemical properties of 500 µM Nor in pH 7 ABS have been studied using poly [Cu(Chr)$_2$Cl]Cl/PGE and unmodified PGE electrodes at 100 mVs$^{-1}$and the result is shown in Fig. 4.44A before blank subtracted and Fig. 4.44B after blank subtracted. As shown in Fig. 4.44B, the blank subtracted voltammogram, the anodic peak current of Nor at the modified electrode was about three times higher than that of the bare PGE. The broad oxidation peak observed at the bare PGE becomes sharper at the poly [Cu(Chr)$_2$Cl]Cl/PGE, indicating enhanced electron transfer at the surface of the modified electrode. The anodic peak potential of the modified electrode (1.06 V) was shifted to a lower value compared to that of the bare PGE (1.18 V), indicating a shift of 120 mV. This shift demonstrates the high electrocatalytic activity of poly[Cu(Chr)$_2$Cl]Cl as a result of enhanced electron transfer kinetics [195].

The peak current enhancement, peak sharpness, and shift towards lower anodic potential confirm the modified electrode has abundant active sites with electrocatalytic properties, and enhanced electron transfer for the oxidation of Nor. The polymer modification increases preconcentration of Nor molecules by stronger binding onto the surface via Cu(II)–O coordination between Cu(II) centers and Nor's carbonyl or carboxyl groups, electrostatic interaction due to the protonated amine group of Nor under acidic

conditions, and π–π stacking enhanced by conjugated structure of polymer and Nor. These effects improve the electrocatalytic sensing of Nor in complex real samples. The poly[Cu(Chr)$_2$Cl]Cl/PGE has a higher electrocatalytic behavior than bare PGE.

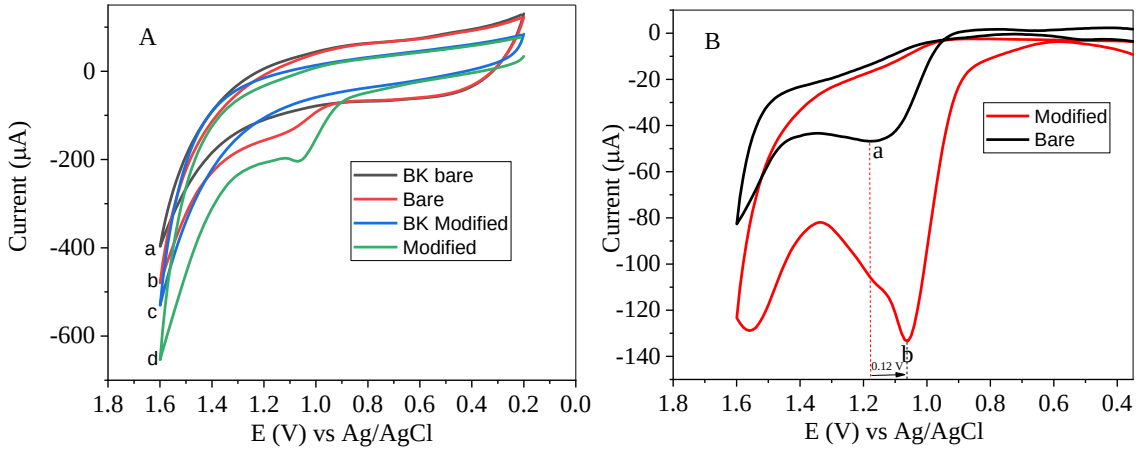


Fig. 4. 44: CVs of 0.1 M PBS at pH 7 and at 100 mVs$^{-1}$ scan rate A(a) bare PGE in the absence of analyte (BK), A(b) bare PGE in the presence of 500 µM Nor, A(c) modified with poly [Cu(Chr)$_2$Cl]Cl/PGE in the absence of the analyte, and A(d) modified with poly [Cu(Chr)$_2$Cl]Cl/PGE and in the presence 500 µM Nor, B(a) is blank subtracted bare PGE and B(b) blank subtracted poly [Cu(Chr)$_2$Cl]Cl/PGE.

The number of electrons transferred during the oxidation of Nor was calculated using equation (4.9).

$$E_p - E_{p1/2} = \frac{48}{\alpha n} \quad \text{---------- (4.9)}$$

The values of $E_p$ and $E_{p1/2}$ obtained from the cyclic voltammogram of Nor Fig. 4.44B(b) at a scan rate of 100 mVs$^{-1}$ were 1058.1 and 997.6 mV, respectively, and their difference was 60.5. The value of αn was calculated to be 0.793, and the value of α for a totally irreversible process is 0.5. As a result, the calculated value of n was 1.59, which is closer to 2.0 and in agreement with the reported literature value [174].

### 4.3.6. Effects of Scan Rate on $I_{pa}$ and $E_{pa}$ of Nor

The effect of scan rate on the anodic peak current and anodic peak potential of 500 µM Nor in PBS of pH 7.0 was studied using CV by varying the scan rate from 15 to 300

$mVs^{-1}$. As shown in the voltammograms of Fig. 4.45A, the anodic peak current increased with the scan rate, and the anodic peak potential shifted to a more positive value, confirming that Nor was undergoing an irreversible oxidation reaction. The value of the correlation coefficient ($R^2$ = 0.99779) in the plots of the oxidative peak current vs. scan rate shown in Fig. 4.45B is higher than the correlation coefficient ($R^2$ = 0.96188) value of the plot of peak current vs. square roots of scan rate in Fig. 4.45C. The higher value of the correlation coefficient of plots of the oxidative peak current vs. scan rate confirms Nor was undergoing adsorptive controlled oxidation. In addition, the value of the slope of the plot of log current vs. log (v) was closer to unity, as shown in Fig. 4.45D, which indicates that the oxidation reaction of Nor was an adsorptive-controlled process [196].

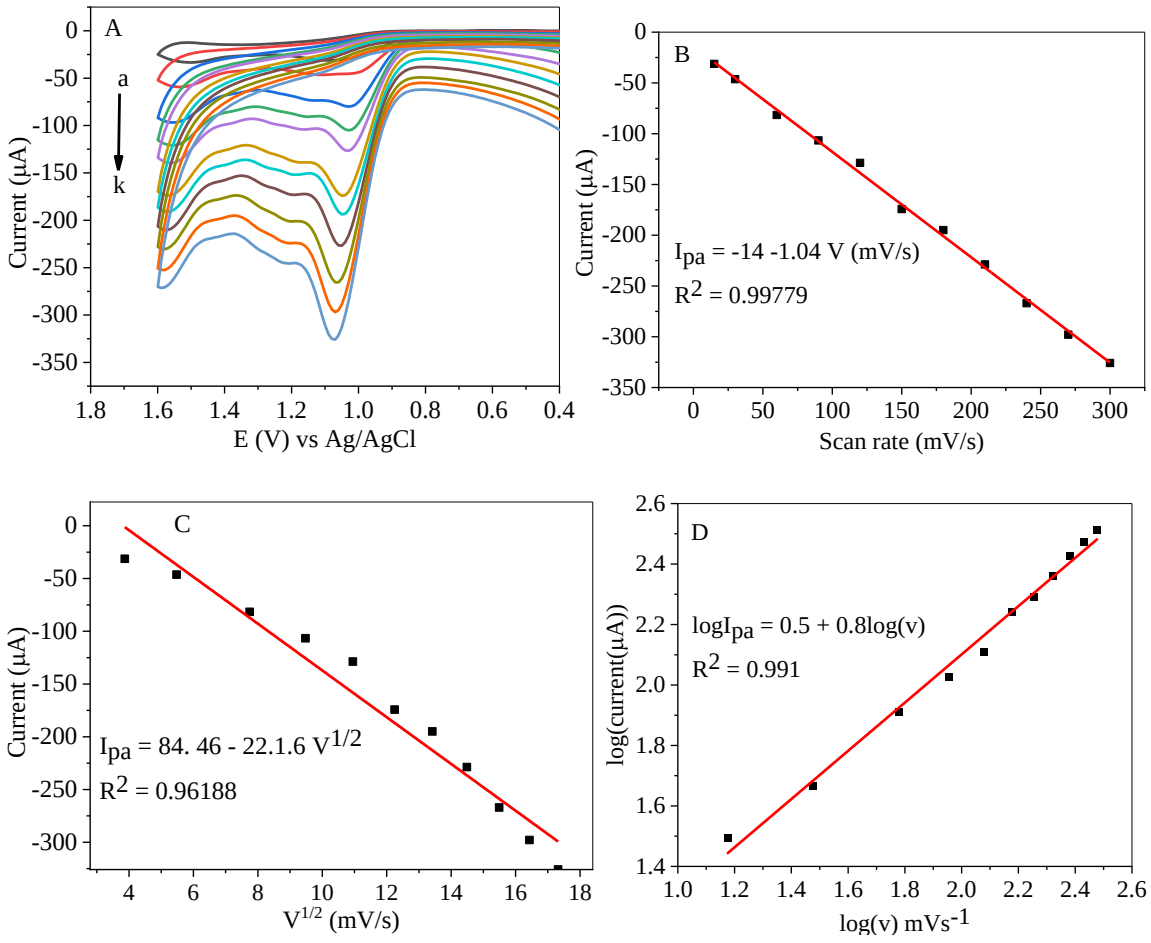

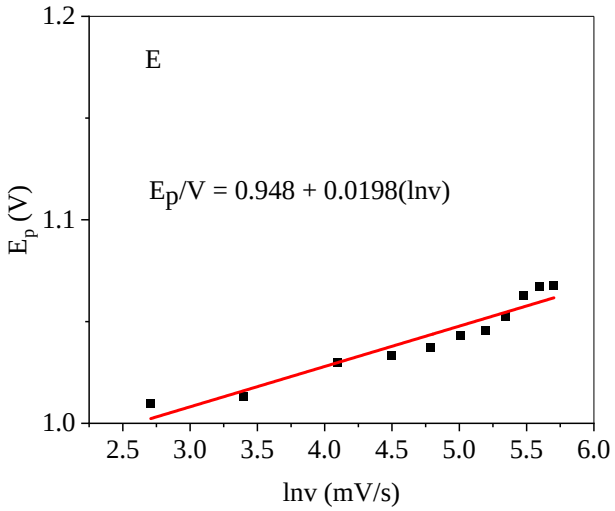


Fig. 4. 45: CVs of 500 µM Nor in pH 7.0 of 0.1 M PBS (A) at different scan rate (15, 30, 60, 90, 120, 150, 180, 210, 240, 270, and 300 $mVs^{-1}$) and (B) plot of $I_{pa}$ vs scan rate, (C) $I_{pa}$ vs square roots of scan rate, (D) plot of log(current) vs log ($v(mVs^{-1})$), and plot of $E_p$ vs lnv (mv/s)

The electron transfer coefficient (α) during oxidation of Nor at the surface of poly[$Cu(Chr)_2Cl$]Cl/PGE was determined using equation (4.10) and the slope value of plot of $E_{pa}$ versus ln(v). From equation 4.10 and Fig. 4.45(E) we can relate $\frac{RT}{(1-\alpha)nf}$ = 0.0198. At T = 298 K and n = 2 and the calculated 'α' value = 0.35 which can be approximated to 0.5. Therefore, α value confirms the irreversibility of the oxidation of Nor in this method.

$$E_p = E^o + \frac{RT}{(1-\alpha)nf}\{0.780 + \ln(\frac{D_R^{\frac{1}{2}}}{K_o}) + \ln[\frac{(1-\alpha)nfv}{RT}]^{1/2}\} \text{ ---------- (4.10)}$$

Where: $E_p$ anodic peak potential, $E^o$–formal potential, n-number of electron, $K^o$-heterogeneous electron transfer rate constant, R-ideal gas constant, T-temperature (298 K), f-faraday's constant, $D_R$-diffusion constant, and (v)-scan rate

### 4.3.7. Effect of pH

The effect of pH on the oxidation peak current and oxidation peak potential of Nor was investigated by measuring the CV of 200 µM Nor in 0.1 M PBS at pH values ranging

from 4.5 to 7.5. As shown in Fig. 4.46A and Fig. 4.46B(a), the oxidation peak current of Nor at poly[Cu(Chr)$_2$Cl]Cl/PGE was increased from pH 4.5 to pH 5.5, and then it declined. Therefore, pH 5.5 was taken as the optimized pH value for the next procedure. Fig. 4.46A also shows that as the pH value increases from 4.5 to 7.5, the oxidation peak potential shifts in the negative direction, which confirms that protons were involved in the redox reaction. Fig. 4.46B(b) shows the plot of the Nor oxidation peak potential against pH value. In this plot, the slope value was 0.097 V/pH, which is closer to 0.0885, which confirms the presence of 3.0 protons for every 2.0 electrons [197]. The proposed oxidation reaction mechanism of Nor is shown in Scheme 4.4.

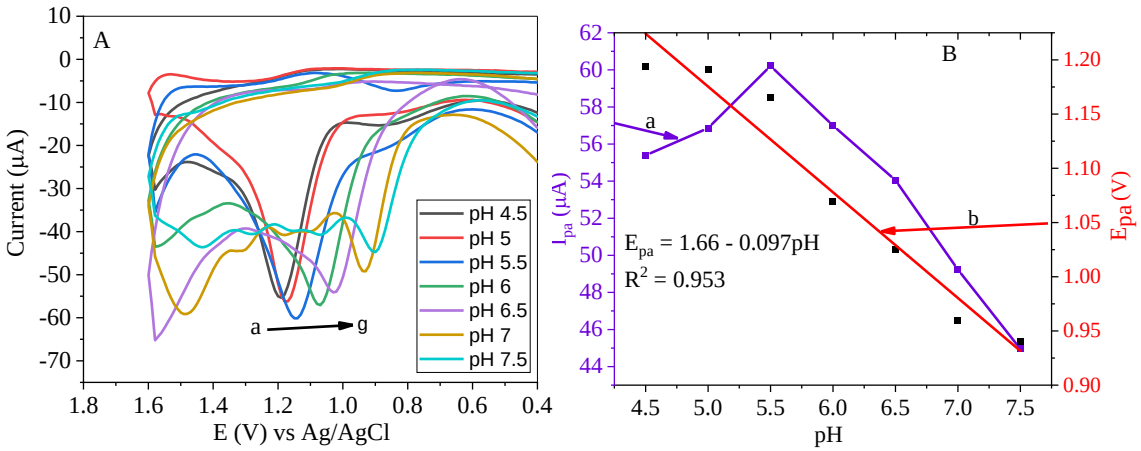


Fig. 4. 46: CVs of 200 µM Nor in 0.1 M PBS at different pH values (a to g: 4.5, 5.0, 5.5, 6.0, 6.5, 7.0, and 7.5) (A) and plot of $I_{pa}$ vs pH B (a) and $E_{pa}$ vs pH B (b) using poly [Cu (Chr)$_2$Cl]Cl/PGE at scan rate of 100 mVs$^{-1}$ .

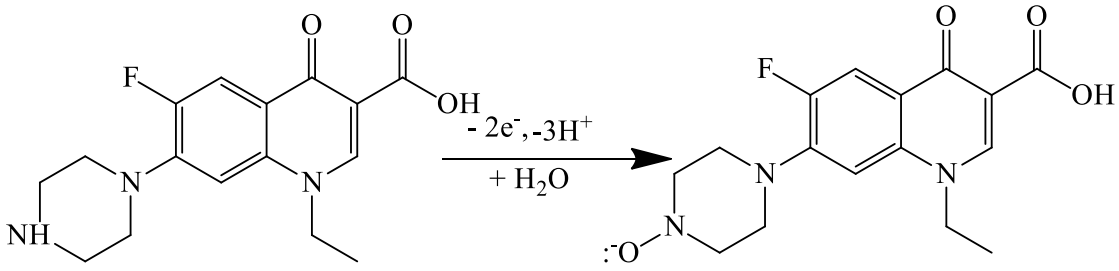


Scheme 4. 4: Proposed reaction mechanism of Norfloxacin

### 4.3.8. Accumulation Time and Accumulation Potential

Accumulation time and accumulation potential for the AdS-SWV of 200 µM Nor in pH 5.5 PBS were optimized using a default step potential of 4 mV, an amplitude of 25 mV, and a frequency 15 Hz. As shown in Fig. 4.47A, the accumulation time was optimized by varying the time from 2 to 30 sec at 0.0 mV accumulation potential [198]. As shown in the inset of Fig. 4.47, the peak current increased as the accumulation time was extended from 2 seconds to 15 seconds, after which it stabilized. Therefore, an accumulation time of 15 seconds was selected as the optimal condition. The accumulation potential also was varied from 350 mV to 750 mV at 15 sec. accumulation time. As shown in Fig. 4.47B and its inset, the peak current was increased from 350 mV to 600 mV, after which the rate of increasing slowed down. Therefore, the accumulation potential at 600 mV was chosen as optimum.

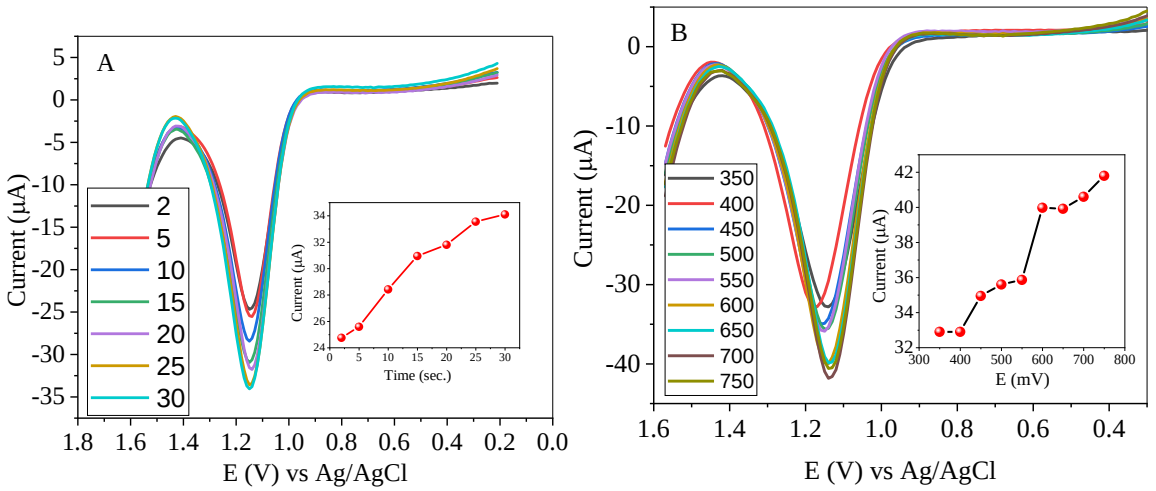


Fig. 4. 47: AdS-SWVs of pH 5.5 PBS containing 200 µM Nor at various accumulation time (2, 5, 10, 15, 20, 25, and 30 sec.) and inset: plot of absolute value of current vs time (A) and (B) at various accumulation potential (350, 400, 450, 500, 550, 600, 650, 700, and 750 mV) and inset: plot of absolute value of current vs accumulation potential at 4 $mVs^{-1}$ step potentials, 25 mV amplitude and 15 Hz frequency using poly [Cu $(Chr)_2Cl]Cl$/PGE.

### 4.3.9. Adsorptive Striping Square Wave Voltammetry Parameter Optimization

In addition to the accumulation potential and accumulation time, the determination of Nor using poly[Cu(Chr)$_2$Cl]Cl/PGE can be affected by step potential, amplitude, and frequency [199]. To optimize each parameter using 200 µM Nor in pH 5.5 PBS, the AdS-SWV at the optimized accumulation potential and accumulation time was measured by varying one while maintaining the others constant. Step potential was varied from 4 mV to 25 mV, amplitude was varied from 10 mV to 45 mV, and frequency was varied from 5 Hz to 40 Hz. The peak current in each parameter was linearly increased, and then its linearity was lost at some point. The parameter was optimized at the point where it lost linearity in each case, as shown in the inset [200]. The voltammogram and the inset of step potential, amplitude, and frequency are plotted in Fig. 4.48A, B, and C, respectively. Based on the loss in linearity indicated by a circle, the parameters were optimized at 15 mV, 30 mV, and 20 Hz, respectively.

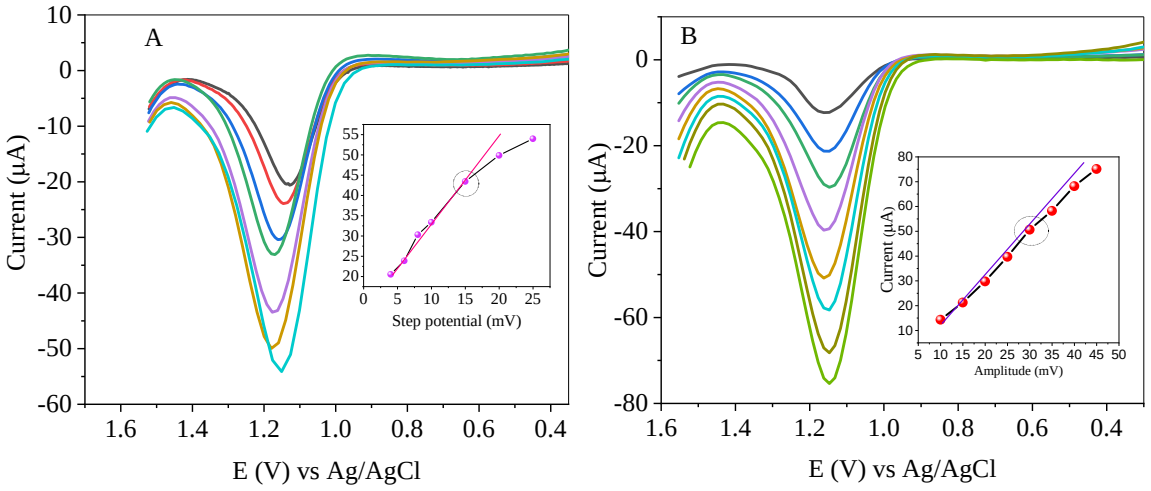

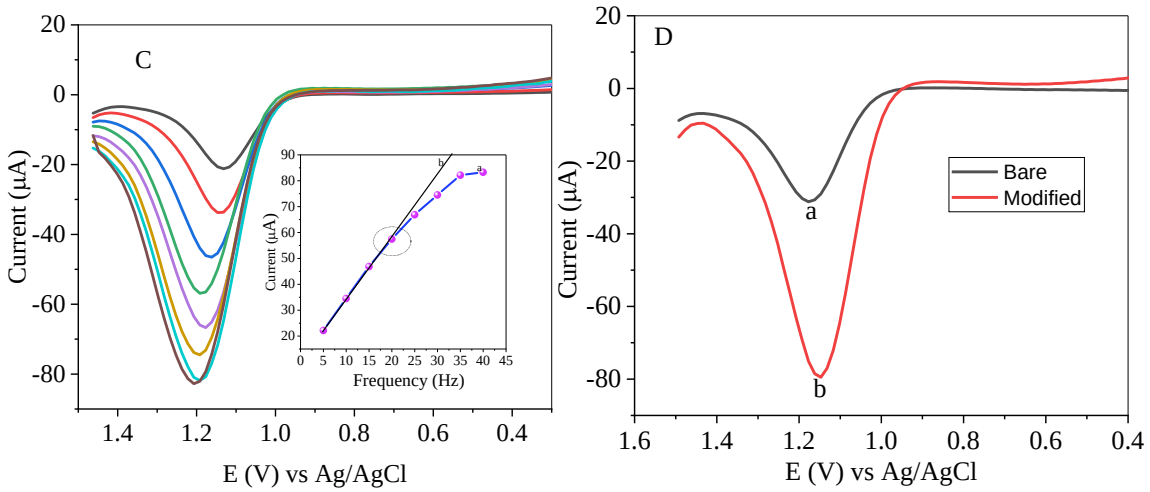


Fig. 4. 48: AdS-SWVs of pH 5.5 PBS containing 200 µM Nor at various step potential (4, 6, 8, 10, **15**, 20, and 25 mV) and inset: plot of absolute value of current vs step potential (A), AdS-SWVs of 200 µM Nor at various amplitude (10, 15, 20, 25, **30**, 35, 40, and 45 mV) and inset: plot of absolute value of current vs amplitude (B), AdS-SWVs of 200 µM Nor at various frequency (5, 10, 15, **20,** 25, 30, 35, and 40 Hz) and inset: plot of absolute value of current vs frequency (C), and AdS-SWVs of pH 5.5 PBS containing 200 µM Nor bare (D)(a) and modified (D)(b) at 15 $mVs^{-1}$ step potentials, 30 mV amplitude and 20 Hz frequency using poly [Cu $(Chr)_2Cl$]Cl/PGE.

### 4.3.10. AdS-SWV Activity of Nor

The AdS-SWV activity of 200 µM Nor in pH 5.5 PBS using poly[Cu$(Chr)_2Cl$]Cl/PGE and bare PGE in the optimized parameters was investigated and shown in Fig. 4.48(D). The peak current of poly[Cu$(Chr)_2Cl$]Cl/PGE was -79.57, and the peak potential was 1148.8 mV (Fig. 4.48 D(b)). The peak current of bare PGE was -31.36, and the peak potential was 1173.7 mV (Fig. 4.48D(a)). These results show the presence of 2.5-fold current enhancements and 24.9 mV anodic peak potential shifts towards lower anodic peak potential. This confirms the new modifier has electrocatalytic properties and has enhanced surface area or enhanced electron transfer rate compared to the bare PGE electrode.

### 4.3.11. Method Calibration

The AdS-SWV method based on poly [Cu(Chr)$_2$Cl]Cl/PGE has been calibrated by preparing a series of standard Nor solutions in pH 5.5 of 0.1 M PBS. As shown in Fig. 4.49A and its inset, the calibration of the method shows current enhancement with linearity in the range of 1.0 µM to 100 µM, with the slope value of -0.51. The slope value of the method is related to the sensitivity of the method. The same series of Nor standard solutions was also measured using UV-Vis spectroscopy. As shown in Fig. 4.49B and its inset, the UV-Vis spectroscopy method shows absorbance linearity only in the concentration range of 1.0 µM to 80 µM and a slope value of 0.031. Therefore, the slope value of AdS-SWV was 16 times higher than the slope value of UV-Vis spectroscopy [201].

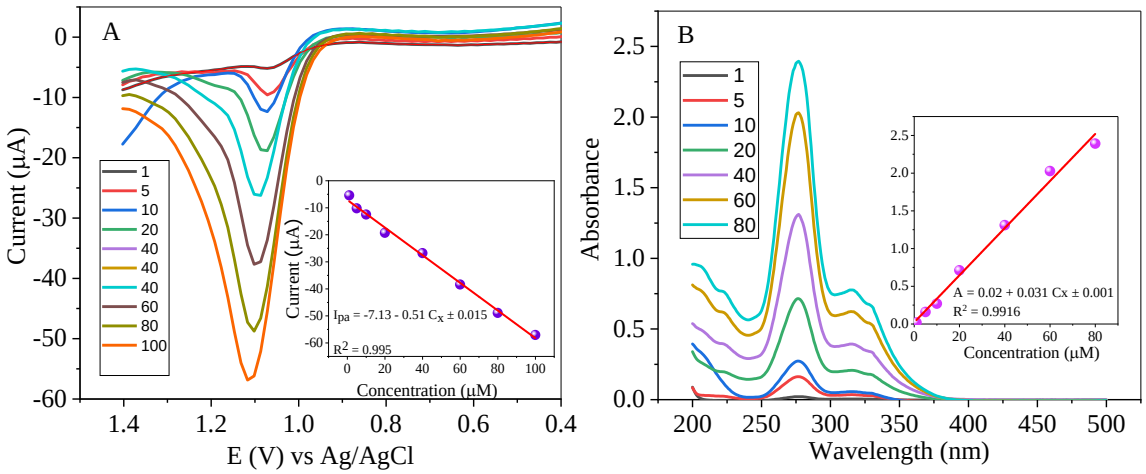


Fig. 4. 49: AdS-SWVs of 0.1 M PBS at pH 5.5 containing various concentrations of Nor (1.0, 5.0, 10.0, 20.0, 40.0, 60.0, 80.0, and 100.0 µM) at poly [Cu(Chr)$_2$Cl]Cl/PGE and the inset is plot of current vs. concentration at accumulation time 15 sec, accumulation potential 600 mV, step potential 15 mVs$^{-1}$, amplitude 30 mV, and frequency 20 Hz (A) and UV-Vis absorption band (B) in (1.0-80.0 µM ) concentration range and its inset was plot of absorbance vs concentration.

### 4.3.12. Real Sample Analysis

#### 4.3.12.1. Tablet Samples from Two Brands

Tablet samples of Nofxin brand analysis were conducted using the spiked method to investigate the method applicability [202]. 40.0 µM tablet samples of Nofxin were spiked with 20 µM, 40 µM, and 60 µM of Nor, and analysis was made using AdS-SWV and UV-Vis techniques in order to evaluate the validity of the developed method. As shown in Fig. 4.50A, the AdS-SWV voltammograms and the absorption bands (Fig. 4.50B) confirm the presence of characteristic peaks of Nor, which increased with its concentration. As listed in Table 4.11, the recovery results were in the ranges of 93.75–99.35 for the developed AdS-SWV method, which is in the accepted range, but the recovery results in UV-Vis were not in the accepted recovery range. The developed poly $[Cu(Chr)_2Cl]Cl$/PGE AdS-SWV result suggests that the proposed method can be used to determine Nor in pharmaceutical samples in an efficient manner.

Table 4. 11: Recovery results of Nor in Nofxin brand samples.

| Un-spiked (µM) | Added Nor (µM) | **Found** (µM) | | % Recovery | |
|---|---|---|---|---|---|
| | | AdS-SWV | UV-Vis | AdS-SWV | UV-Vis |
| 40 | 0 | 40.0 ± 0.3 | 82.1 ± 0.013 | - | - |
| 40 | 20 | 59.65 ± 1.5 | 85.6 ± 0.002 | 98.25 | 228.2 |
| 40 | 40 | 79.74 ± 1.4 | 89.9 ± 0.004 | 99.35 | 124.7 |
| 40 | 60 | 96.25 ± 0.2 | 90.9 ± 0.007 | 93.75 | 84.9 |

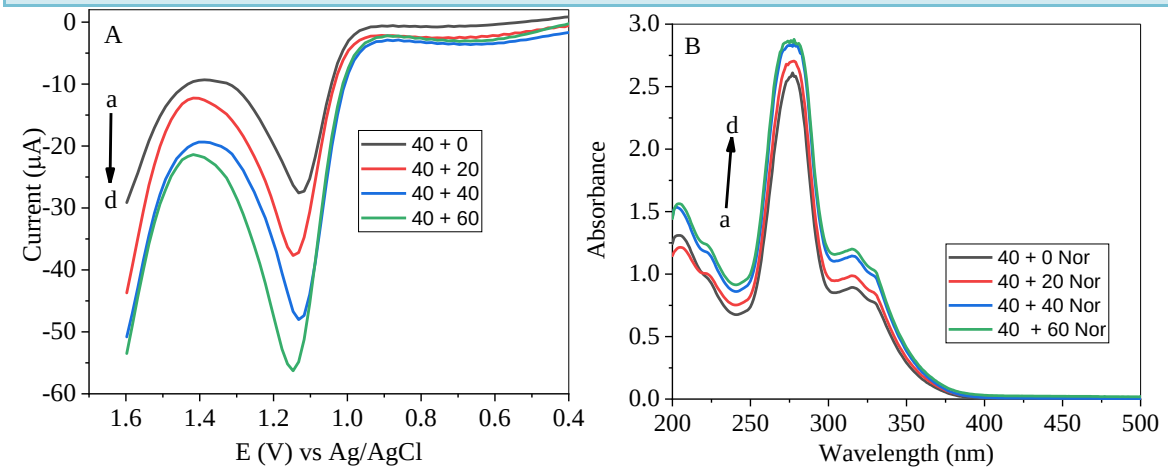

Fig. 4. 50: Blank corrected AdS-SWVs (A) and UV-Vis absorption band (B) of Nofxin brand pharmaceutical samples spiked with various concentrations of standards Nor (40.0 + 0.0, 40.0 + 20.0, 40.0 + 40.0, and 40.0 + 60.0 µM) at poly [Cu(Chr)$_2$Cl]Cl/PGE in PBS of pH 5.5 at step potential 15 mVs$^{-1}$, amplitude 30 mV, and frequency 20 Hz.

**Gyrablock Brands**

Tablet samples of Gyrablock brand analysis were also conducted using the spiked method. 40.0 µM tablet samples of Gyrablock were spiked with 20 µM, 40 µM, and 60 µM of Nor, and analysis was made using the AdS-SWV and UV-Vis techniques in order to perform the validity of the developed method. As shown in Fig. 4.51A, the AdS-SWV voltammograms and the absorption bands in Fig. 4.51B confirm the presence of characteristic peaks of Nor, which increased with its concentration. As presented in Table 4.12, the recovery results were in the ranges of 96.6–109.9 for the developed poly [Cu(Chr)$_2$Cl]Cl/PGE AdS-SWV methods, which is in the accepted range for the determination of Nor in Gyrablock brand. But the recovery results in UV-Vis were not in the accepted recovery range. The developed poly [Cu(Chr)$_2$Cl]Cl/PGE AdS-SWV result suggests that the proposed method can be used to determine Nor in Gyrablock brand pharmaceutical samples in an efficient manner.

Table 4. 12: Recovery results of Nor in Gyrablock brand samples.

| Un-spiked (µM) | Added Nor (µM) | **Found** (µM) | | % Recovery | |
|---|---|---|---|---|---|
| | | AdS-SWV | UV-Vis | AdS-SWV | UV-Vis |
| 40 | 0 | 44.3 ± 1.7 | 52.7 ± 0.002 | - | - |
| 40 | 20 | 61.96 ± 2.3 | 77.5 ± 0.002 | 109.8 | 187.25 |
| 40 | 40 | 83.95 ± 1.1 | 87.4 ± 0.008 | 109.9 | 118.38 |
| 40 | 60 | 97.98 ± 0.7 | 88.4 ± 0.004 | 96.6 | Not linear |

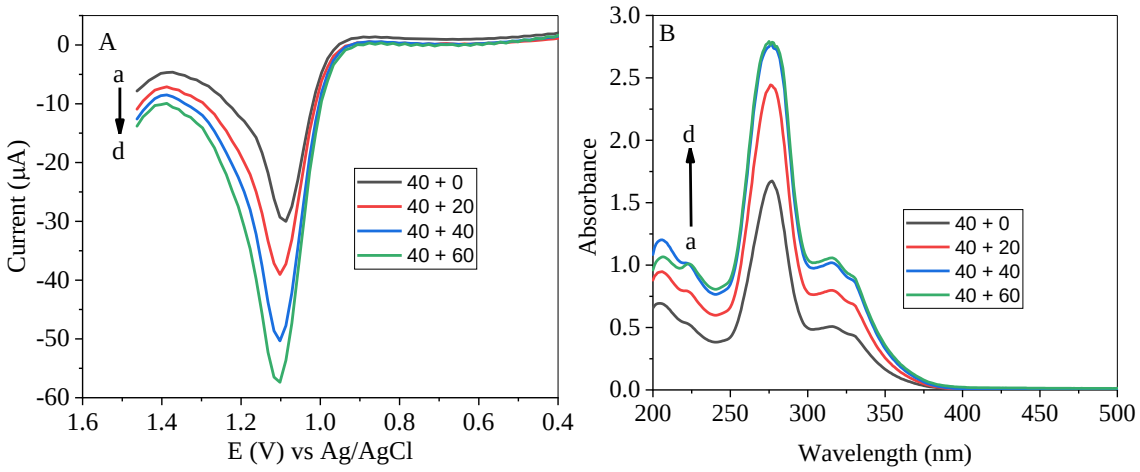


Fig. 4. 51: Blank corrected AdS-SWVs(A) and UV-Vis absorption band (B) of tablet of Gyrablock brand pharmaceutical samples spiked with various concentrations of standards Nor (40.0 + 0.0, 40.0 + 20.0, 40.0 + 40.0, and 40.0 + 60.0 µM) at a poly [Cu(Chr)$_2$Cl]Cl/PGE in PBS of pH 5.5 at step potential 15 mVs$^{-1}$, amplitude 30 mV, and frequency 20 Hz.

### 4.3.12.2. Milk Samples

Milk samples analyse were conducted using poly [Cu(Chr)$_2$Cl]Cl/PGE-based AdS-SWV and UV-Vis spectroscopy via the spiked method [202]. The processed milk samples were spiked with 20 µM, 40 µM, and 60 µM of Nor. As shown in Fig. 4.52A, the AdS-SWV voltammograms confirm the presence of characteristic peaks of Nor, which increased with its concentration, but no measurable peak in the non-spiked milk sample. This confirms that the matrices in the milk samples have no effect on the Nor in poly [Cu(Chr)$_2$Cl]Cl/PGE-based AdS-SWV method. Therefore, the developed method can be used to analyze Nor in milk samples without interfering. The recovery of the spiked milk samples was 81.8 to 91.13 %, as listed in Table 4.13. In UV-Vis spectrophotometry shown in Fig. 4.52B, the non-spiked milk sample shows an unassigned peak in the characterization peak of Nor. But the absence of a peak signal in the non-spiked milk sample, indicated by the circle, confirms the peak was not due to the presence of Nor in the milk samples. The recovery of the spiked milk samples was not in the accepted range due to the background effect and linear range effect.

Table 4. 13: Recovery results of Nor in milk samples.

| Un-spiked (µM) | Added Nor (µM) | **Found** (µM) | | % Recovery | |
|---|---|---|---|---|---|
| | | AdS-SWV | UV-Vis | AdS-SWV | UV-Vis |
| **ND** | 0 | - | 36.8 ± 0.002 | - | - |
| **ND** | 20 | 16.4 ± 0.5 | 69.9 ± 0.007 | 81.8 | 166.5 |
| **ND** | 40 | 36.5 ± 0.2 | 74.5 ± 0.005 | 91.13 | 94.25 |
| **ND** | 60 | 52.9 ± 0.4 | 78.2 ± 0.018 | 88.28 | 69 |

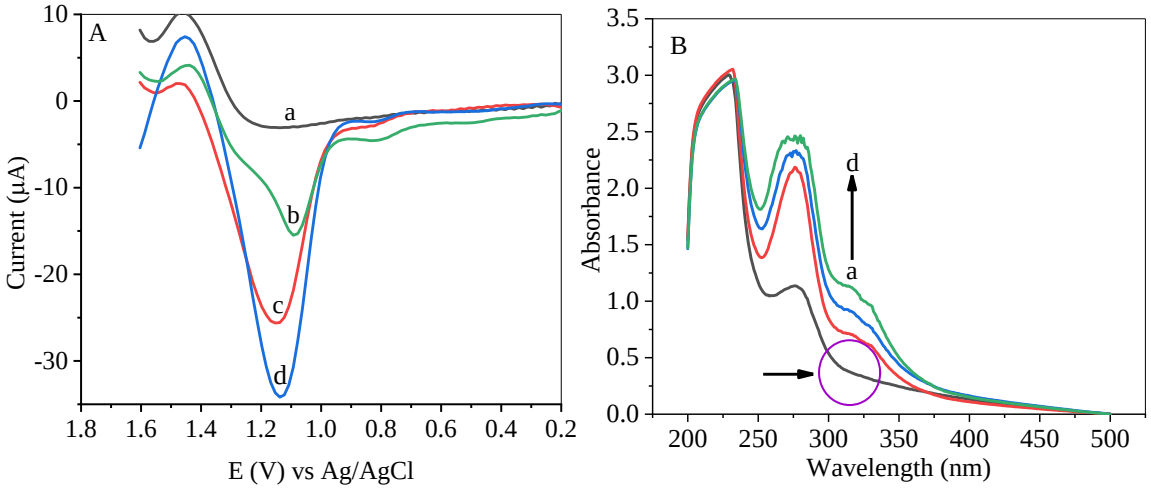


Fig. 4. 52: Blank corrected AdS-SWVs(A) and UV-Vis absorption band (B) of milk samples spiked with various concentrations of standards Nor (non-spiked (a), 20.0 (b), 40.0 (c), and 60.0 (d) µM) at a poly $[Cu(Chr)_2Cl]Cl$/PGE in PBS of pH 5.5 at step potential 15 $mVs^{-1}$, amplitude 30 mV, and frequency 20 Hz.

### 4.3.13. Selectivity Study

The selectivity of the proposed method was evaluated in the presence of paracetamol and caffeine. This is due to caffeine is a common food additive, and paracetamol is a widely usepainkiller that can be co-administered or simultaneously present with Norfloxacin in pharmaceutical formulations or during medication intake[203]. The impact was investigated at different concentrations of paracetamol and caffeine using poly $[Cu(Chr)_2Cl]Cl$/PGE based AdS-SWV and UV-Vis spectrophotometry. The characteristic peaks of caffeine and paracetamol appear separately from the characteristic peaks of Nor in poly $[Cu(Chr)_2Cl]Cl$/PGE based AdS-SWV, as shown in Fig. 4.53(A (a & b) and Fig.

4.53C (a & b)). As shown, characteristic peaks of caffeine and characteristic peaks of paracetamol have no signal at the characteristic peak of Nor in the Fig given in Fig. 4.53. The characteristic peak of Nor remains nearly constant as the interference concentration rises. This constant peak of Nor confirms that the developed method can be used to analyze Nor selectively in the presence of caffeine and paracetamol. But the characteristic peaks of caffeine and paracetamol did not appear separately from the characteristic peaks of Nor in the UV-Vis absorption band, as shown in Fig. 4.53(B and D). As shown, characteristic peaks of caffeine and characteristic peaks of paracetamol have absorption bands at the characteristic peak of Nor in the figure given in Fig. 4.53(B and D). The characteristic peak of Nor did not remain constant as the interference concentration rises. The variation in concentration of Nor confirms that the UV-Vis methods of analysis cannot be used to analyze Nor in the presence of caffeine and paracetamol.

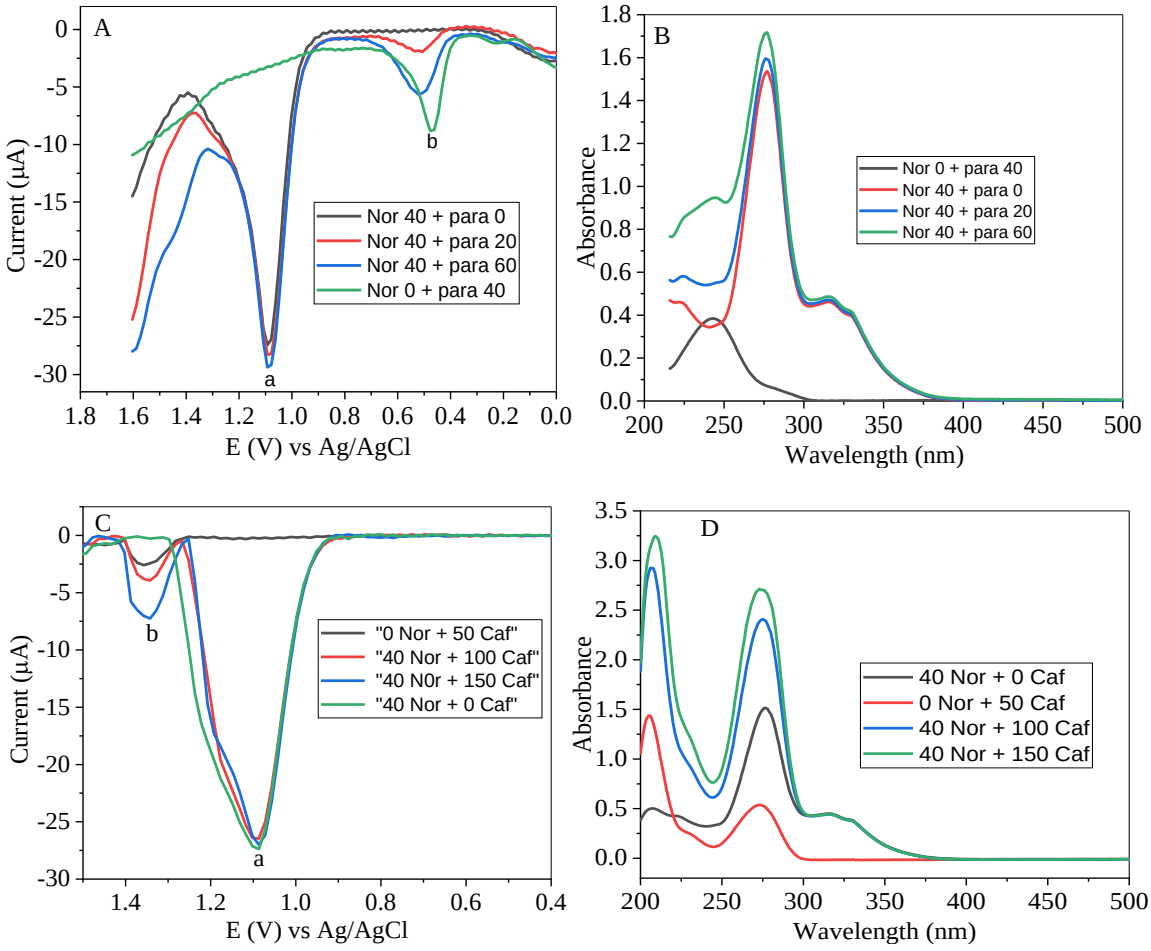

Fig. 4. 53: AdS-SWVs (A & C) and UV-Vis absorption bands (B & D) of 40 µM Nor in the presence of various concentrations of paracetamol (0.0, 20.0, 40.0, and 60.0 µM) (A & B) and caffeine(0.0, 50.0, 100.0, and 150.0 µM) (C & D) in PBS of pH 5.5 at step potential 15 $mVs^{-1}$, amplitude 30 mV, and frequency 20 Hz.

### 4.3.14. Method Repeatability and Reproducibility

In order to study the developed method's repeatability, 200 µM Nor was measured five times using single poly $[Cu(Chr)_2Cl]Cl$/PGE repeatedly, and for reproducibility, 200 µM Nor was measured five times using different poly $[Cu(Chr)_2Cl]Cl$/PGE [204]. The results were plotted and shown in Fig. 4.54A and Fig. 4.54B, respectively. The standard deviation of the repeatability and reproducibility of poly$[Cu(Chr)_2Cl]Cl$/PGE was 0.443 and 1.28, respectively, and their relative standard deviations were calculated to be 0.8% and 2.4, respectively. These results show that the developed method was repeatable and reproducible for the measurement of Nor with high precision.

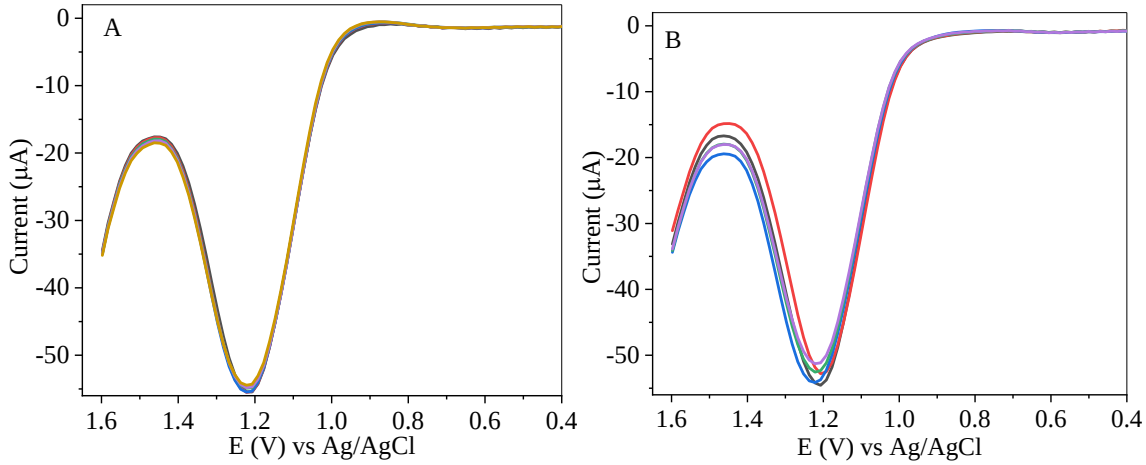


Fig. 4. 54: AdS-SWV of reputability(A) and reproducibility(B) of the developed method using 200 µM Nor and poly $[Cu(Chr)_2Cl]Cl$/PGE in PBS of pH 5.5 at step potential 15 $mVs^{-1}$, amplitude 30 mV, and frequency 20 Hz.

### 4.3.15. Comparison with Literature Values

The developed method for the determination of Nor has been compared with previously reported literatures in terms of the modifier used, dynamic range, limit of detection, and

types of electrode used. As listed in table 4.14, the developed method has a relatively wider dynamic range and comparable limit of detection (LoD). LoD was calculated using the formula 'LoD = 3xS/m' where 'S' is standard deviation of the blank and 'm' is the slope of the calibration curve of Nor. In this work the electrode used was PGE, but in the other reported literatures, the electrodes used are GCE. PGE-based electrode is cheaper and easily available than glassy carbon electrode and surface cleaning in the entire experimental session is not required. Hence, the developed PGE-based complex modified electrochemical method is promising for the determination of Nor in pharmaceuticals and in milk samples.

Table 4. 14: Comparison of different literature values reported for the determination of Nor

| Electrode used | Technique | Modifier | Dynamic range (µM) | LoD (µM) | Reference |
|---|---|---|---|---|---|
| **GCE** | SWV | EPPGS/GCE | 0. 5-50 | 0.28 | [34] |
| **GCE** | DPV | MWCNTs-TOCT/GCE | 0.5-8.0 | 0.1 | [205] |
| **GCE** | LSV | MWCNTs/GCE | 0.1-100.0 | 0.05 | [206] |
| **GCE** | SWV | MIP/MWCNT/GCE | 0.1-8.0 | 0.046 | [207] |
| **PGE** | AdS-SWV | $[Cu(Chr)_2Cl]Cl$/PGE | 1-100 | 0.096 | This work |

## 4.4. Poly [Cu(Reso)$_3$Cl]/PGE Based Electrochemical Sensor for the Simultaneous Determination of Norfloxacin and Caffeine in Pharmaceuticals and Urine Samples

### 4.4.1. Characterization of the Complex

#### 4.4.1.1.Physicochemical Characterization

The decomposition of the complex at 223 ºC is probably attributed to the weak Cu to O bond because of the weak field nature of oxygen-donating ligands. The conductance measurements, recorded for 1x10$^{-3}$ M solutions of the complex in methanol, are indicated in table 4.15. The value shows that the complex is a 2:1 electrolyte. The slightly higher value (48 S cm$^2$ mol$^{-1}$) than expected (30-40 S cm$^2$ mol$^{-1}$) for a 2:1 ion ratio is attributed to the softness and weak interaction with the solvent molecules, which gives freedom of motion; hence, the higher velocity of mobility of the anion [208]. The good agreement between the calculated and experimental values in the percentage composition of the metal indicated the correctness of the proposed structure.

Table 4. 15: Summary of studied physicochemical properties of $Na_2[Cu(Reso)_3Cl]$

| physical property | $Na_2[Cu(Reso)_3Cl]$ |
|---|---|
| Color | Dark brown |
| Melting point ($^0$C) | Decomposed at 223 |
| Solubility | Soluble in $CH_3CN$, DMSO, methanol |
| Conductivity (S cm$^2$ mol$^{-1}$) in methanol | 48 |
| Cu content, %(Calculated/Experimental) | 13.45/13.38 |

#### 4.4.1.2.UV-Vis Spectroscopy Characterization

The electronic spectrum of resorcinol shows an absorption band at 215 nm (Fig. 4.55B), assigned to the n → σ* transition [209]. Upon deprotonation to the resorcinolate anion (ResoNa), this band disappears, reflecting a lowering of the non-bonding (n) orbital energy and a widening of the n–σ* gap. The π → π* transition at 274 nm in resorcinol shifts to 295 nm in ResoNa as shown in Fig. 4.55C), indicating enhanced π-electron delocalization and increased charge density in the aromatic ring. A further weak band near 280 nm undergoes a pronounced bathochromic shift to 450 nm, consistent with

further perturbation of the π system [210]. Upon coordination of the resorcinolate ligand to Cu(II), transitions involving non-bonding orbitals are no longer observed, indicating effective metal–ligand interaction. The d–d transitions of the copper(II) salt at 551 nm and 569 nm disappear, likely owing to ligand-field modification and the Laporte-forbidden nature of these transitions. A new absorption band appears at 312 nm (Fig. 4.55D), assignable to an intraligand π → π* transition or a ligand-to-metal charge transfer (LMCT), thereby supporting the formation of the Cu(II)–resorcinolate complex [211].

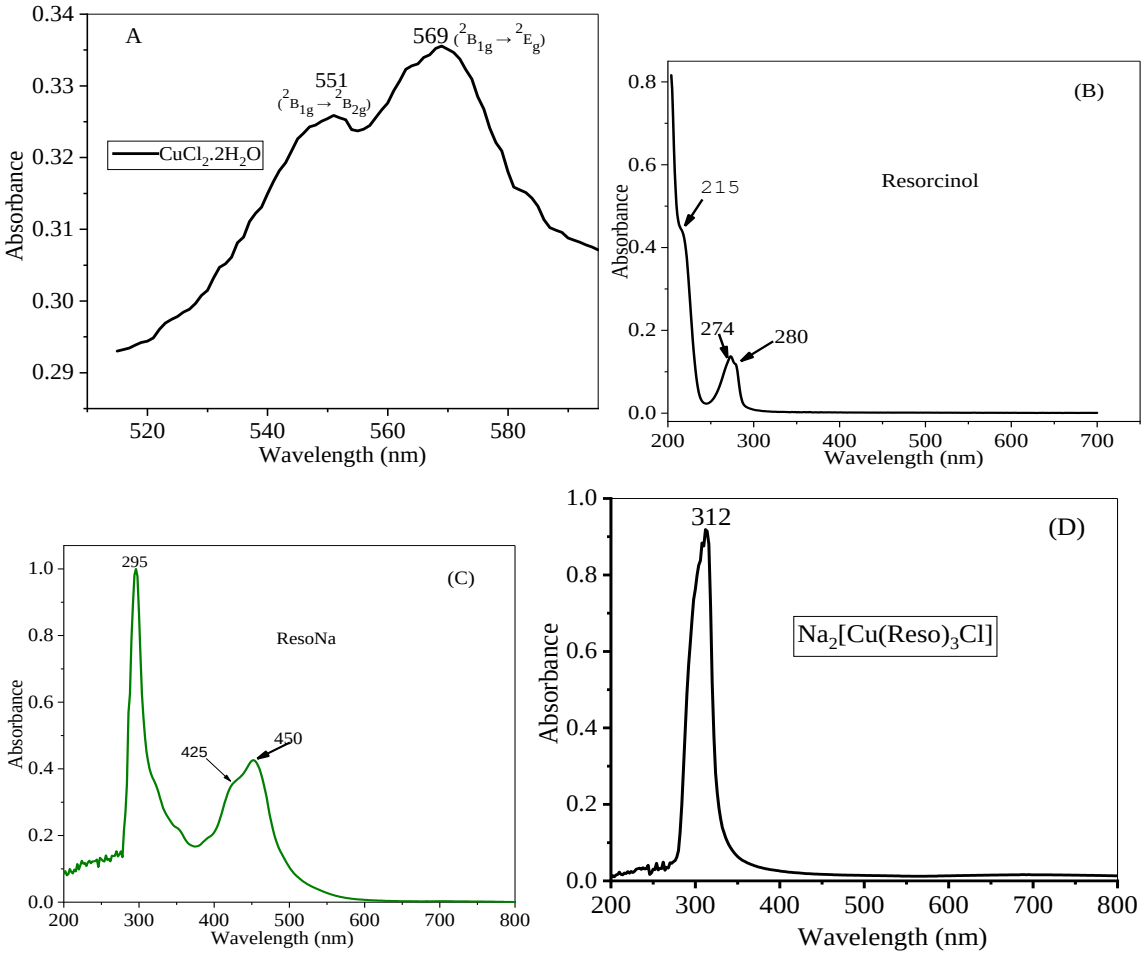


Fig. 4. 55: Absorption bands of (A) $CuCl_2.2H_2O$, (B) resorcinol, (C) sodiumresorcinolate (ResoNa), (D) $Na_2[Cu(Reso)_3Cl)$

### 4.4.1.3.FT-IR Spectroscopy Characterization

The FT-IR spectrum of resorcinol shows a broad percent transmittance at 3262 $cm^{-1}$, attributable to the ν(O–H) stretching vibration (Fig. 4.56a). Upon deprotonation to resorcinolate (ResoNa), this band shifts to 3453 $cm^{-1}$ (Fig. 4.56b), reflecting the loss of hydrogen bonding and increased ionic character of the O–H [212, 213].

The characteristic ν(C=C) and ν(C–O) stretching frequencies of resorcinol observed at 1613 $cm^{-1}$ and 1166 $cm^{-1}$, respectively, shift to 1600 $cm^{-1}$ and 1147 $cm^{-1}$ in ResoNa, consistent with electron delocalization following deprotonation [214].

Upon coordination of resorcinolate to Cu(II), the ν(C=C) band moves slightly to 1608 $cm^{-1}$, suggesting an increase in C–C bond order due to back-donation from the metal center [211]. A new absorption band appearing at 458 $cm^{-1}$, assigned to ν(Cu–O), confirms coordination of the ligand through the deprotonated phenolic oxygen [215]. These spectral shifts collectively support the formation of a Cu(II)–resorcinolate complex in the deprotonated state.

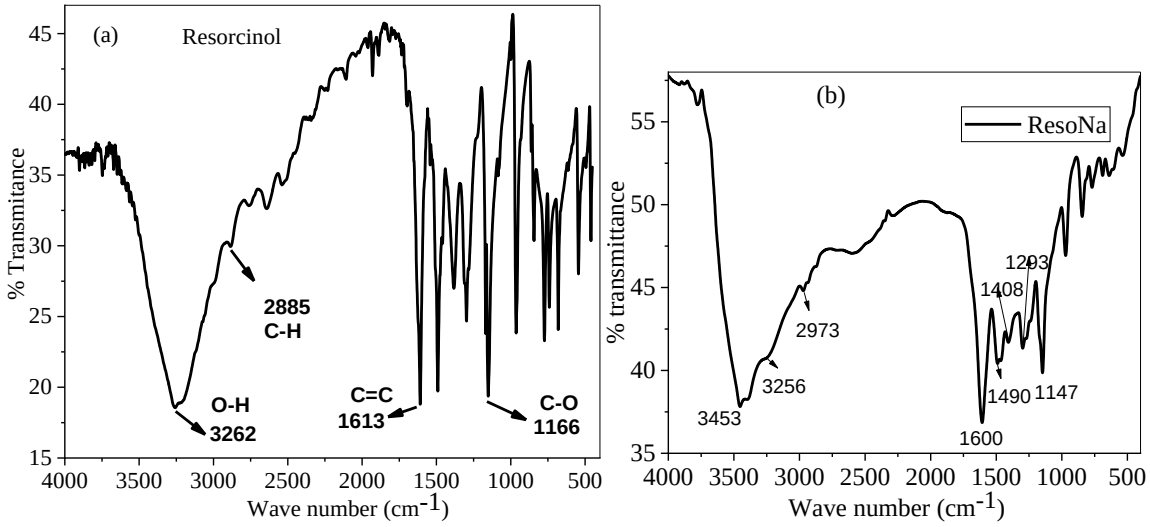

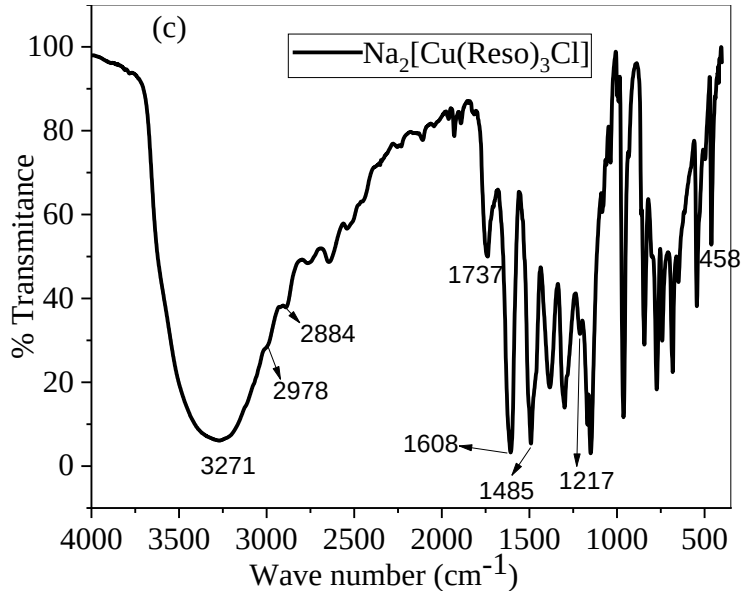


Fig. 4. 56: FT-IR spectra of (a) Resorcinol, (b) ResoNa, (c) $Na_2[Cu(Reso)_3Cl]$

Based on characterization the proposed reaction procedure of the complex ($Na_2[Cu(C_{18}H_{15}O_6Cl]$ ($Na_2[Cu(Reso)_3]$) was shown in (Scheme 4.5) and equations (4.11) & (4.12).

$$C_6H_6O_2 + NaOH \rightarrow NaC_6H_5O_2 + H_2O \ldots\ldots\ldots\ldots\ldots (4.11)$$

$$CuCl_2.2H_2O + 3NaC_6H_5O_2 \rightarrow (Na_2[Cu(C_{18}H_{15}O_6)Cl]) \ldots\ldots\ldots\ldots\ldots\ldots\ldots\ldots (4.12)$$

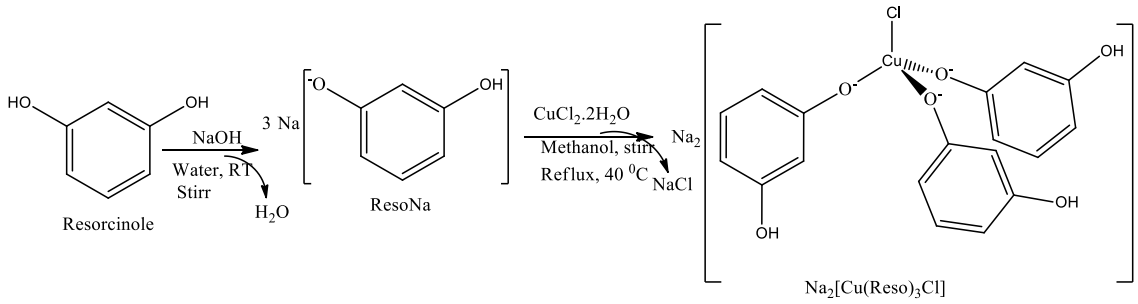


Scheme 4. 5: The proposed synthesis path of $Na_2[Cu(Reso)_3Cl]$

### 4.4.2. Selection of Potential Window

The potential window required to polymerize 1.0 mM $[Cu(Reso)_3Cl]$ was optimized by using different potential range (-0.8 & 1.6, -1.0 & 1.6, -1.2 & 1.6, -1.4 & 1.6, -1.6 & 1.6, and -1.8 & 1.6) at 15 scan cycles and at a 100 $mVs^{-1}$ scan rate. The DPV oxidation

voltammogram of Nor and Caff for each of the potential windows was taken, and the current intensities were compared at a 50 $mVs^{-1}$ scan rate [190]. The potential window, which provides a DPV voltammogram with higher current intensity for both Nor and Caff, was selected. As shown in Fig. 4.57, poly [$Cu(Reso)_3Cl$]/PGE in the range of (-1.4 & 1.6) provides intense anodic peak current compared to others, and this is also shown in the inset. Therefore, -1.4 & 1.6 were selected to synthesize poly [$Cu(Reso)_3Cl$]/PGE electrode.

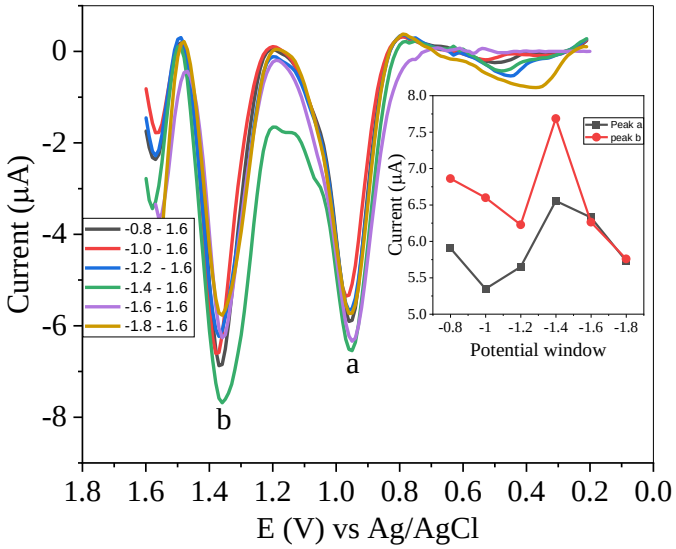


Fig. 4. 57: DPV of 100:200 µM Nor to Caff in pH 7.0 PBS using poly [$Cu(Reso)_3Cl$]/PGE synthesized in different potential windows (-0.8 & 1.6, -1.0 & 1.6, -1.2 & 1.6, -1.4 & 1.6, -1.6 & 1.6, and -1.8 & 1.6) at 15 scan cycles, at 50 $mVs^{-1}$ scan rate, and Inset: Plot of absolute value of current vs. potential window for both peak a (Nor) and peak b (caffeine)

### 4.4.3. Selection of Film Thickness

Poly [$Cu(Reso)_3Cl$]/PGE was synthesized using scan cycles of (5, 8, 10, 12, 14, and 16). The synthesized electrode at each scan cycle was tested using 100:200 µM Nor to Caff, respectively and the resulting current of Nor and Caff in pH 7.0 PBS were plotted as shown in Fig. 4.58. As shown in Fig. 4.58, poly [$Cu(Reso)_3Cl$]/PGE synthesized at 10 scan cycles provides the most intense DPV anodic peak for both Nor and Caff, and this is

also shown in the inset [216].Therefore, scan cycles at 10 was optimized to synthesize Poly [Cu(Reso)$_3$Cl]/PGE.

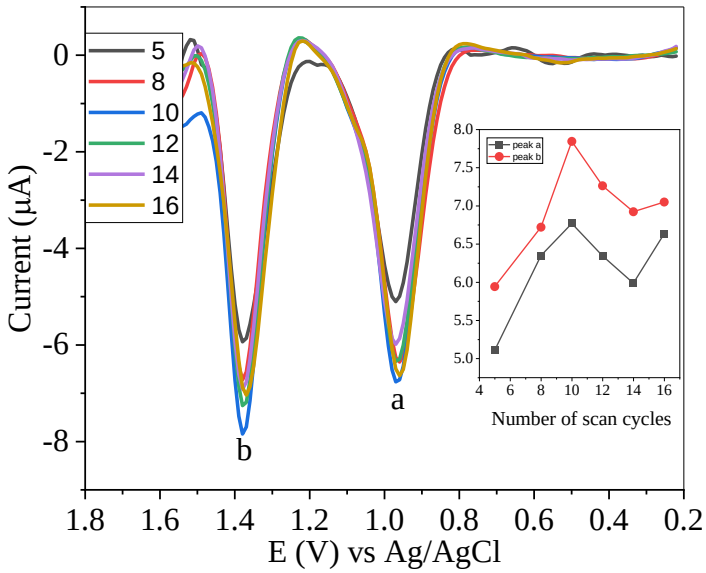


Fig. 4. 58: DPV of 100:200 µM Nor and Caff respectively in pH 7.0 PBS using poly [Cu(Reso)$_3$Cl]/PGE synthesized in different scan cycles (5, 8, 10, 12, 14, and 16) in a -1.4 & 1.6 potential window and at a 50 mVs$^{-1}$ scan rate and Inset: Plot of absolute value of current vs. number of scan cycles for both the Nor peak (a) and the caffeine peak (b)

### 4.4.4. Synthesis of poly [Cu(Reso)$_3$Cl]/PGE

Poly [Cu(Reso)$_3$Cl]/PGE has been synthesized and the voltammogram of the polymerization process of the synthesis was shown in Fig. 4.59(A). As shown in Fig. 4.59(A), different peaks (i, ii, and iii) were appearing and grow with scan cycle indicating the growth of the film on the electrode surface. The direction of the scan cycle is shown by the arrow. The first (i) and the last (ii) scan cycles of the polymerization are shown in the inset of Fig. 4.59(A). The last scan cycle shows a broader and higher reduction and oxidation peak current. The synthesized modifier and the bare PGE electrode were stabilized using monomer free 0.5 M $H_2SO_4$ in the range of -0.75 & 0.8 for 6 scan cycles at a 100 mVs$^{-1}$ scan rate and plotted as shown in Fig. 4.59(B (b and a)). As shown in Fig. 4.59(B), the peak intensity of poly[Cu(Res)$_3$Cl]/PGE Fig. 4.59(B(b)) was more than 60

times relative to bare PGE (Fig. 4.59B(a)), which indicates the presence of effective modification of the electrode [56].

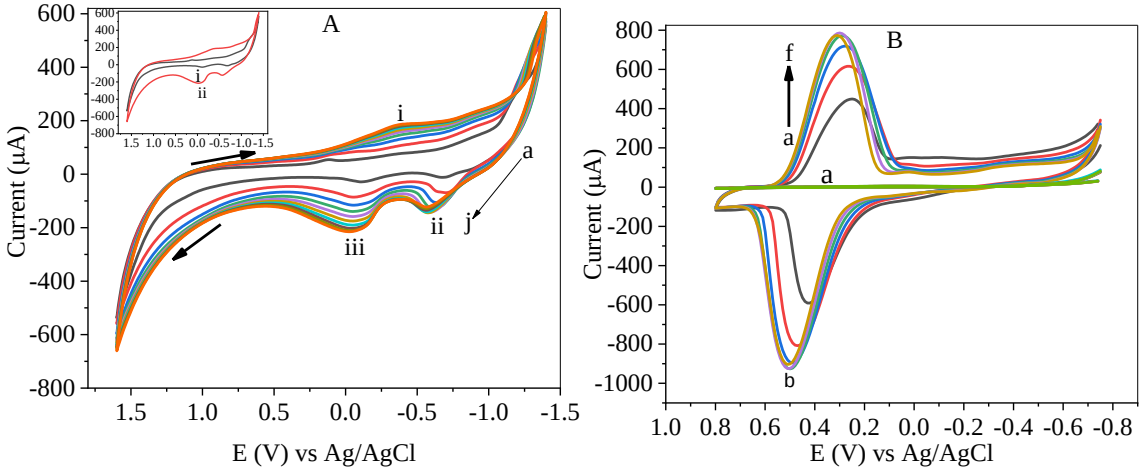


Fig. 4. 59: CVs of (A) 1.0 mM [Cu(Reso)$_3$Cl] scanned between (-1.4 and 1.6) for 10 scan cycles at 100 mVs$^{-1}$ scan rate and (B) CVs of 0.5 M $H_2SO_4$ (a) using bare PGE and (b) poly [Cu(Reso)$_3$Cl]/PGE scanned between (-0.75 and 0.8) for 6 scan cycles at 100 mVs$^{-1}$: Inset in (A) showed the initial (i) and final (ii) cycle of the polymerization

The polymerization mechanism of the monomer can be initiated by the potential energy applied from the electrode. The weakly bound electron from the oxygen heteroatom can be removed and form a radical cation. The radical cation is highly reactive and can rearrange itself and bind the other nearby monomers to form a polymer. The proposed polymerization mechanism is shown in Scheme 4.6. The number of monomers 'n' in a polymer was calculated using the area under each cycle of the polymerization curve. Calculating the area under the curve can be related to the total charge flowing during the polymerization. The integrated area represents current versus voltage; therefore, the total value must be divided by the scan rate to convert it to current versus time, which can then be related to the charge. The sum of charge of all 10 scan cycles was 41,183 µcoulombs. Based on equation 4.13, the value of a mole is 0.427 µmoles which is equivalent to 2.57 x $10^{17}$ molecules. The total count of polymers shown in figure 7.9C is 54. If the area was 1/1000 of the total area of the FTO, the total number of polymers will be 54000. Then the number of monomers per polymer will be 47.6 x $10^{11}$ monomers or molecules.

$Q = nNF$…… (4.13)

Where n, mole per unit ion, N, number of mole, Q, charge, and F, faraday's constant

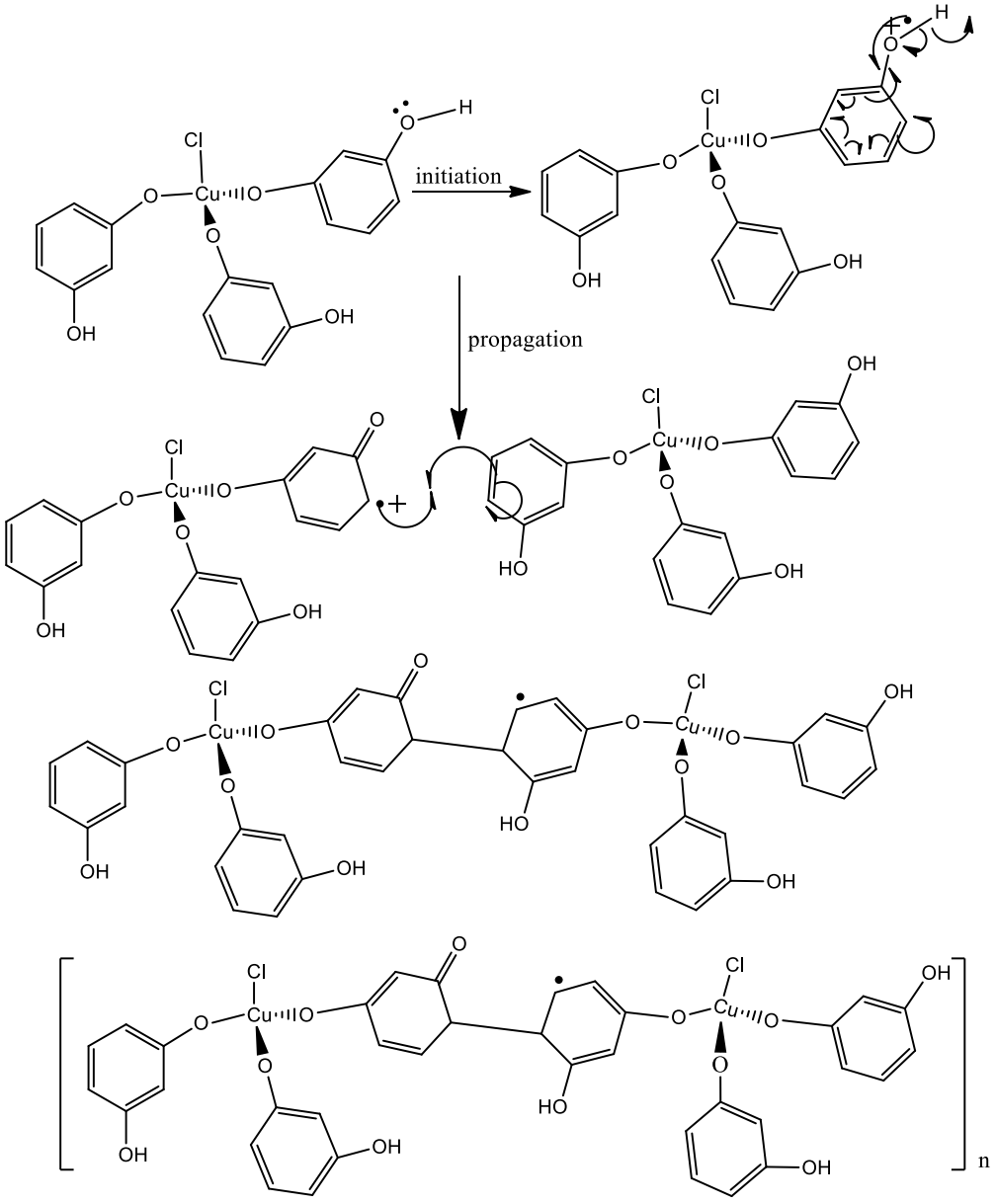


Scheme 4. 6: proposed polymerization mechanism

### 4.4.5. Characterization of the Modified Electrode

#### 4.4.5.1.Cyclic Voltammetry Characterization of poly [Cu(Reso)$_3$Cl]/PGE

The CV voltammogram of 10.0 mM $[Fe(CN)_6]^{-3/-4}$ in 0.1 M KCl using both modified and bare electrode were measured. Current intensity and peak potential of the two voltammogram of the two electrodes were compared to observe the effect of

modification. As shown in Fig. 4.60(b), the anodic peak current of the modified electrode was twofold than the bare electrode (Fig. 4.60(a)), and there is 150.3 mV peak potential shift towards lower potential. The current enhancement and peak potential shift indicates the effective modification of the surface of PGE electrode.

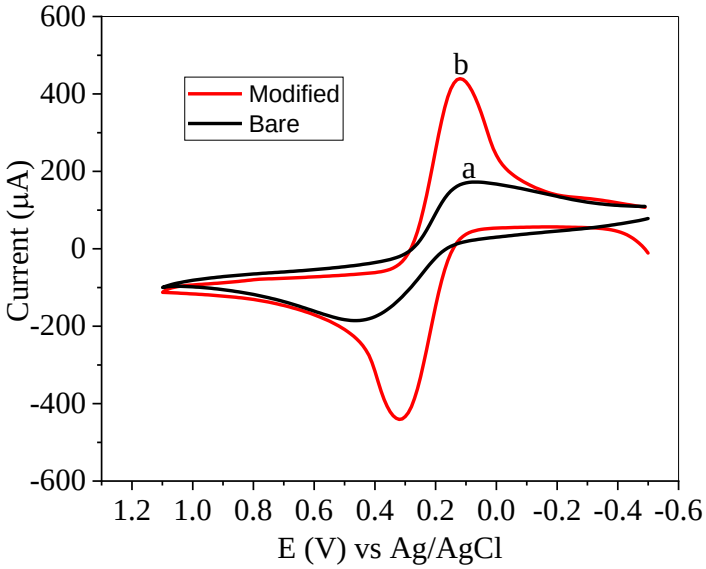


Fig. 4. 60: CVs of 10.0 mM $[Fe(CN)_6]^{-3/-4}$ in 0.1 M KCl using (a) bare PGE and (b) poly $[Cu(Reso)_3Cl]$/PGE at 100 $mVs^{-1}$

The area of modified and unmodified electrodes were investigated by measuring CV voltammogram of 10.0 mM $[Fe(CN)_6]^{-3/-4}$ in supporting electrolyte of 0.1 M KCl at various scan rates (15-300 mV/s). The Randles-sevick equation (4.14) and slope values were used to calculate the area. Voltammograms of unmodified (Fig. 4.61A) and voltammograms (Fig. 4.61B) of modified electrodes with their own insets were plotted.

$$I_{pa} = 2.69 \times 10^5 \times n^{3/2} A D^{1/2} V^{1/2} C_o \quad \text{(4.14)}$$

Where: 'A' is the effective surface area, 'n' is the number of electrons involved during the redox reaction$[Fe(CN)_6]^{-3/-4}$(n = 1), '$I_{pa}$' is the peak current, 'D' is the diffusion coefficient of $[Fe(CN)_6]^{-3/-4}$ (D = 7.6 x $10^{-6}$ $cm^2s^{-1}$), '*v*' is the scan rate, and '$C_o$' is the concentration of $[Fe(CN)_6]^{-3/-4}$ (10.0 mM). The calculated area of poly $[Cu(Reso)_3Cl]$/PGE was 0.69 $cm^2$ and the calculated area of unmodified electrode was 0.23 $cm^2$. The calculated surface area of poly $[Cu(Reso)_3Cl]$/PGE shows roughly 3.0 fold

of unmodified electrode. The modified electrode's area enhancement, confirms effective deposition of modifiers and enhancement of surface roughness [192].

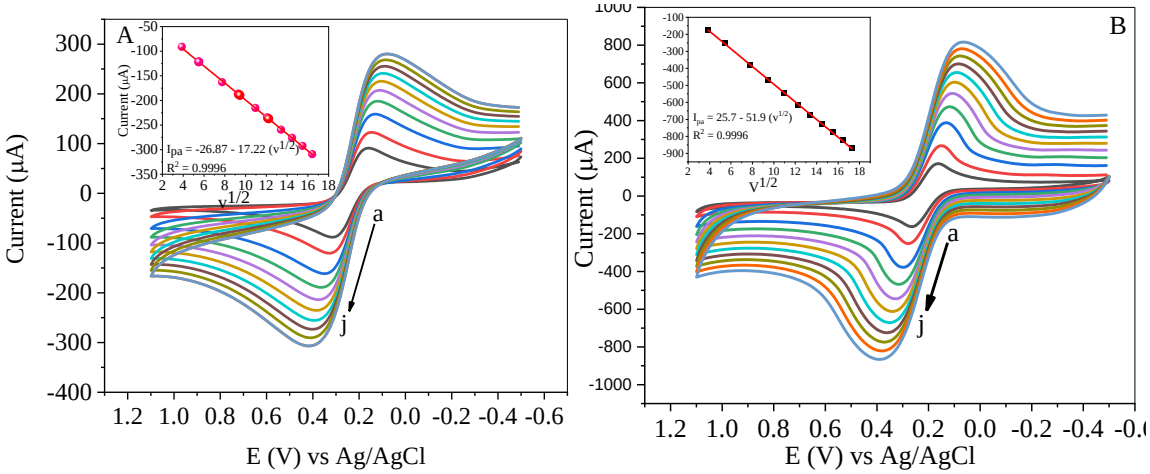


Fig. 4. 61: CVs of 10.0 mM $[Fe(CN)_6]^{-3/-4}$ in 0.1 M KCl (A) bare PGE and (B) modified by poly $[Cu(Reso)_3Cl]$/PGE at different scan rates (15, 30, 60, 90, 120, 150, 180, 210, 240, 270, and 300 $mVs^{-1}$) Insets: Plot of current vs. square root of scan rate

### 4.4.5.2.Electrochemical Impedance Spectroscopy

The electrochemical impedance (EIS) was measured for both bare and modified electrode in the frequency range of 0.1-1,000,000 Hz, at amplitude of 0.01 V, and potential at 0.23 V using 10.0 mM $[Fe(CN)_6]^{-3/-4}$ in 0.1 M KCl as a probe. The resulting EIS for both bare and modified electrodes were plotted using the Nyquist plot, as shown in PGE Fig. 4.62. Charge transfer resistance of the poly $[Cu(Reso)_3Cl]$/PGE electrode shown in Fig. 4.62(b) was reduced by threefold compared to the unmodified electrode in Fig. 4.62(a). This means the conductivity of the modified electrode was increased due to modification. The value of the heterogeneous electron transfer rate constant ($K^o$) in the modified electrode was greater than the $K^o$ of the unmodified electrode. The enhancement of the $K^o$ indicates the effective modification of the electrode. Double-layer capacitance and $K^o$ were calculated using equation (4.15) and equation (4.16), respectively. All the calculated values are listed in Table 4.16.

$$C_{dl} = \frac{1}{2\pi R_{ct} f} \text{----------(4.15)}$$

$$K^o = \frac{RT}{F^2 A C R_{ct}} \text{---------- (4.16)}$$

Where: $K^o$-heterogeneous electron transfer rate constant, $C_{dl}$-double layer capacitance, $R_{ct}$-charge transfer resistance, A-area, R-ideal gas constant, C-concentration, T-temperature (298 K), $F^2$-Faraday's constant, and f-frequency corresponding to the maximum imaginary impedance

Table 4. 16: Values of EIS parameters from the Nyquist plot

| Electrode | $R_s$(Ω $cm^2$) | $R_{ct}$(Ω $cm^2$) | $K^o$ | $C_{dl}$ (F) | f (Hz) |
|---|---|---|---|---|---|
| **PGE** | 41.0 | 205.5 | $5.63 \times 10^{-7}$ | $7.75 \times 10^{-7}$ | 1000 |
| **poly [Cu(Reso)$_3$Cl]/PGE** | 42.4 | 63.2 | $6.1 \times 10^{-7}$ | $25.19 \times 10^{-7}$ | 1000 |
| **Circuit fitting error %** | 2.07 | 4.2 | --- | 8.5 | --- |

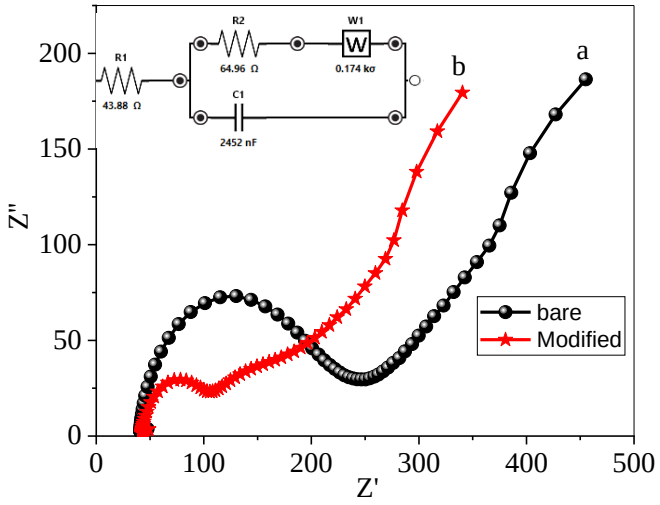


Fig. 4. 62: The Nyquist plot of 10.0 mM $[Fe(CN)_6]^{-3/-4}$ in supporting electrolyte of 0.1 M KCl (a) using bare electrode and (b) modified electrode by poly $[Cu(Reso)_3Cl]$/PGE in the frequency range: 0.1–1,000,000 Hz, potential 0.23 V, and amplitude 0.01 V.

### 4.4.5.3.UV-Vis, Digital optical Microscopy, and Contact Angle Characterization

The polymerized [$Cu(Reso)_3Cl$]/FTO was studied by using digital optical microscopy, UV-Vis and drop shape analyzer using electropolymerized fluorine-doped tin oxide (FTO) as a substrate. Using both bare FTO and polymerized FTO as a substrate, UV-Vis bands and images of digital optical microscope images were taken and the resulting bands and images are shown in Fig. 4.63A and Fig. 4.63(B and C), respectively. The new absorption band at (376 nm) in the UV-Vis spectrum (Fig. 4.63A(b)) indicated by the rectangle relative to the bare FTO Fig. 4.63A(a) confirm the deposition of poly [$Cu(Reso)_3Cl$] on surface of FTO. In addition, the absorption band of the monomer in the UV-Vis spectrum is shown in Fig. 4.55(D) was at 312 nm. But after polymerization, the peak was shifted to 376 nm, which indicates the density of π-electrons was increased and confirms polymerization.

Digital optical microscopy before and after deposition of the modifier at 5 mm distance and 1800x magnification scale, were taken. As shown in Fig. 4.63B, due to modification the surface of FTO was changed from smooth to rough (Fig. 4.63C). The change of surface of FTO from smooth to rough due to deposition of [$Cu(Reso)_3Cl$] using FTO as a substrate approves the deposition of the polymer. Similar and related deposition of [$Cu(Reso)_3Cl$]/PGE on the surface of PGE and roughness of the surface of the PGE was expected [154].

The surface of FTO was changed due to surface coating from hydrophilic and wetting to hydrophobic [217]. In this study, surface wettability of FTO before modification, before washing by acid, and after washing the poly[$Cu(Reso)_3Cl$]/FTO electrode was assessed using a contact Shape Analyzer. The result of the contact angle is shown in Fig. 4.63(D, E, and F). As shown, the average contact angle value was increased from 26.4º to 106.3º before washing by $H_2SO_4$ and 26.4º to 71.4º after washing the modified FTO. The average water contact angle of the modified FTO before washing is higher than after washing due to the adsorbed monomers on the surface of the FTO. The change of value of contact angel indicates change of the surface chemistry of FTO by poly[$Cu(Reso)_3Cl$]/FTO due to its deposition.

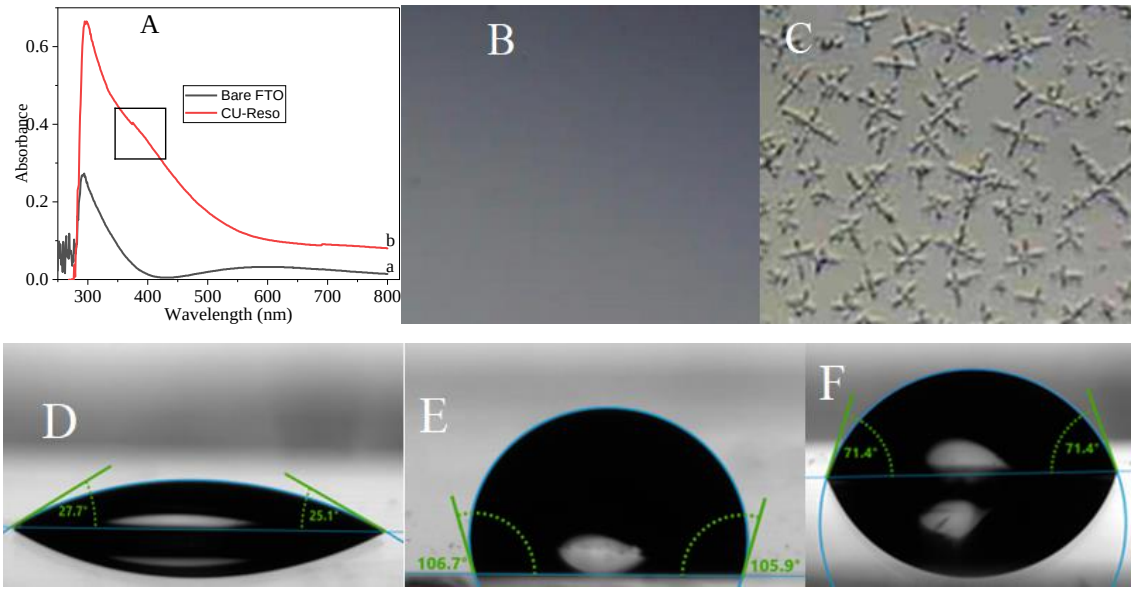


Fig. 4. 63: UV-Vis spectra of poly $[Cu(Reso)_3Cl]$/FTO on the surface of FTO (A) and digital optical microscopy images at 5 mm distance and 1800x magnification scale (B and C) and water contact angle (D, E, and F); (Aa, B, and D) are using bare FTO, (Ab, C, E, and F) are using modified FTO, and (E) is before washing by $H_2SO_4$

### 4.4.5.4.Electrochemical Properties of Nor and Caff

The current response of 100 µM Nor and 200 µM Caff in pH 7 PBS were studied using poly $[Cu(Reso)_3Cl]$/PGE and bare PGE electrodes simultaneously using DPV at 50 $mVs^{-1}$. As shown in the background corrected DPV voltammogram in Fig. 4.64, peak current of the modified electrode was two-fold and more compared to peak current of the bare PGE electrode. Current enhancement for both Nor (peak a) and Caff (peak b) confirms the modified electrode enhanced in its electrochemical activity towards Nor and Caff.

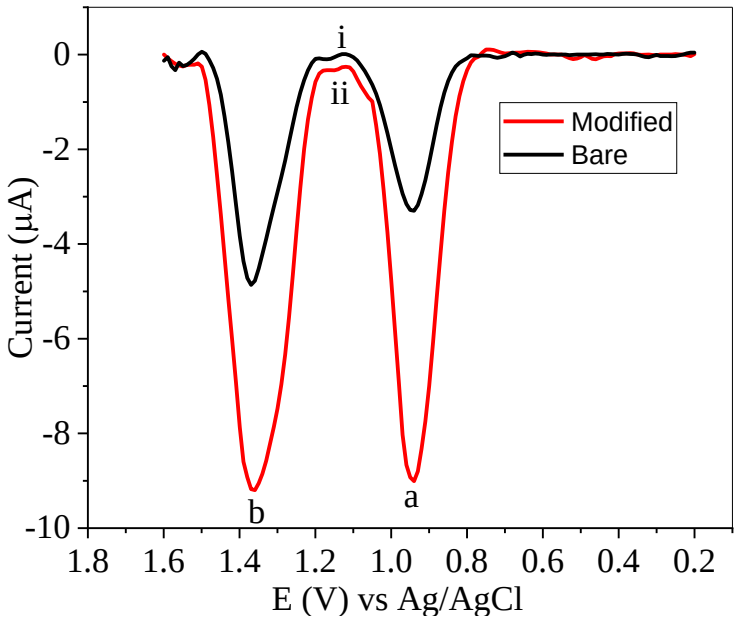


Fig. 4. 64: DPVs of background-corrected 100 µM Nor (peak a) and 200 µM Caff (peak b) in 0.1 M PBS at pH 7 and at 50 $mVs^{-1}$ scan rates (i) bare PGE and (ii) poly $[Cu(Reso)_3Cl]$/PGE.

### 4.4.6. Effects of Scan Rate on $I_{pa}$ and $E_{pa}$ of Nor and Caff

The change in current and potential due to a change in scan rate was studied by measuring the CV voltammograms of 100 µM Nor and 200 µM Caff in different scan rates (30 to 270 $mVs^{-1}$). As shown in the CV voltammograms of Fig. 4.65A, peak current was raised due to a change in scan rate and peak potential was shifted for both Nor and Caff, which confirms both Nor and Caff were undergoing irreversible oxidation. The correlation coefficient for Nor ($R^2$ = 0.9901) and the correlation coefficient for Caff ($R^2$ = 0.9903), Fig. 4.65B is greater than the correlation coefficient of Nor ($R^2$ = 0.9516) and the correlation coefficient of Caff ($R^2$ = 0.9661) shown in the plot of peak current vs. square roots of scan rates in Fig. 4.65C. This confirms that the oxidation reaction of both Nor and Caff in this method was undergoing an adsorptive-controlled reaction [218].

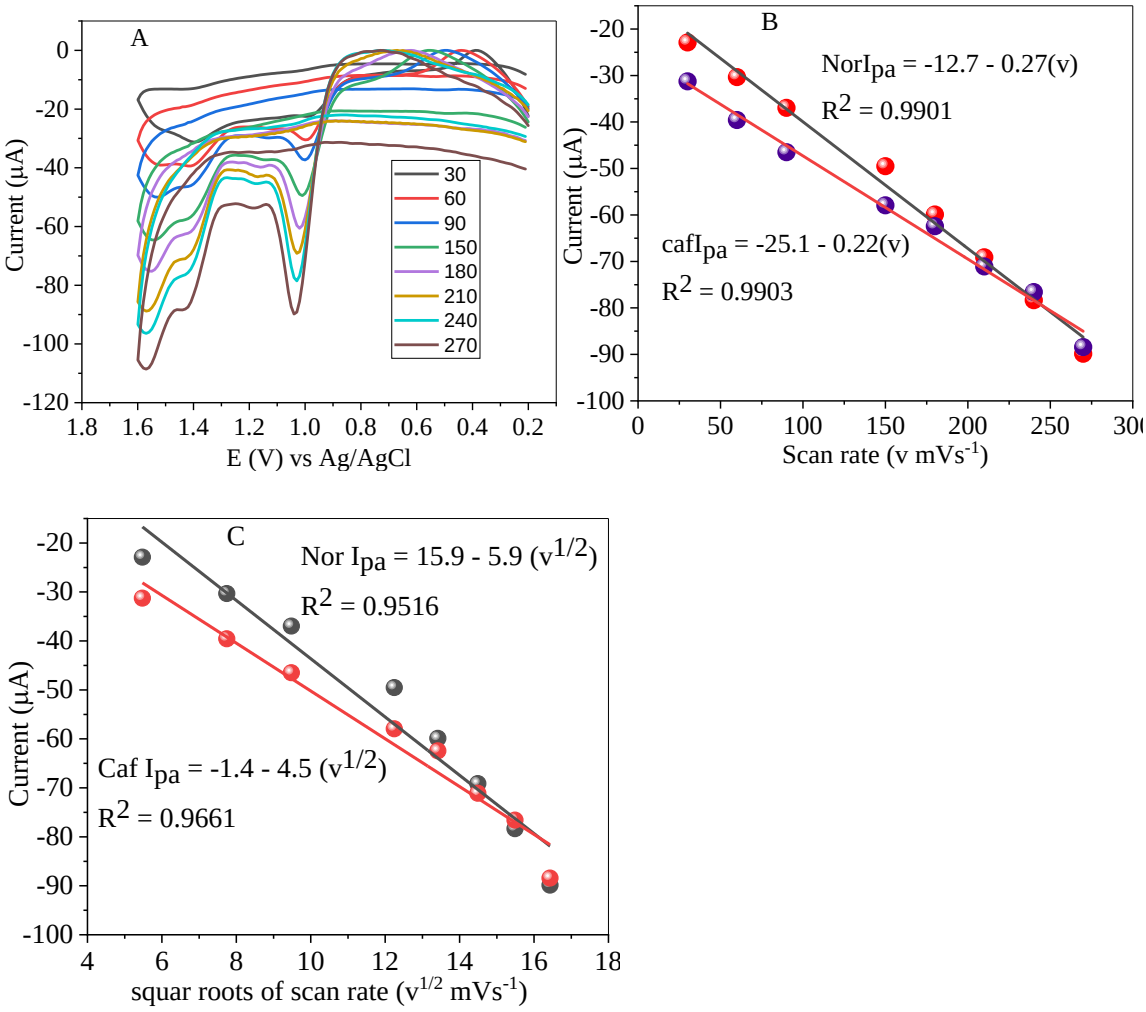


Fig. 4. 65: CVs of BK subtracted 100 µM Nor and 200 µM Caff in pH 7.0 of 0.1 M PBS (A) at different scan rates (30, 60, 90, 120, 150, 180, 210, 240, and 270 $mVs^{-1}$); (B) plot of $I_{pa}$ vs scan rate; and (C) plot of $I_{pa}$ vs square roots of scan rate

### 4.4.7. Effect of pH

Different pH values on current and potential of Nor and Caff were studied by measuring the DPV of 100 µM Nor and 200 µM Caff in pH range from 4.5 to 7.0 of 0.1 M PBS. As shown in Figs. 4.66A, 4.66(B(b)), and 4.66(C(ii)), the current of Nor and Caff at poly $[Cu(Reso)_3Cl]$/PGE rise from pH 4.5 to pH 6.0. But after pH 6.0 it was dropped. As a result, pH 6.0 was optimized. Presence of a potential shift towards the negative direction in the pH range from 4.5-7.0 shown in Fig. 4.66A, confirms the involvement of protons in the reaction. Fig. 4.66(B (a)) and Fig. 4.66(B (i)) show the plots of the Nor and Caff

peak potential against pH value, respectively. The slope value of -0.11 V/pH for Nor is closer to 0.0885, indicating the presence of 3-protons for every 2-electrons [61]. But in the case of Caff, the slope value was -0.034 V/pH, which is closer to -0.0592, indicating a 1:1 protons-to-electrons ratio in the reaction.

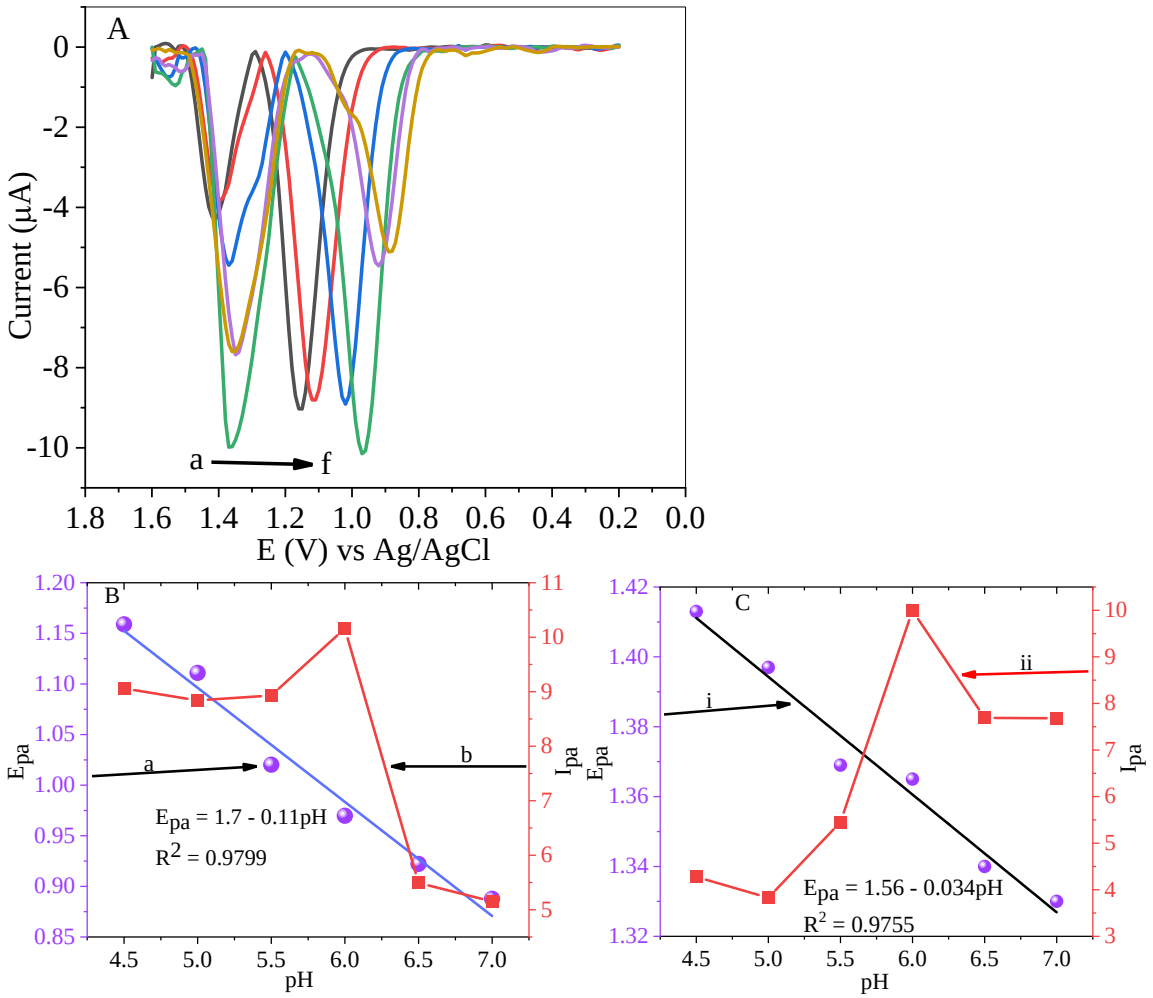


Fig. 4. 66: DPVs of 100 µM Nor and 200 µM Caff in 0.1 M PBS at different pH values (a to f: 4.5, 5.0, 5.5, 6.0, 6.5, and 7.0) (A), plot of $I_{pa}$ vs. pH B (b) and $E_{pa}$ vs pH B (a) for Nor, plot of $I_{pa}$ vs pH C (ii) and $E_{pa}$ vs pH C (i) for Caff using poly $[Cu(Reso)_3Cl]$/PGE at a scan rate of 50 $mVs^{-1}$.

The reaction mechanism of Nor was proposed as shown in Scheme 4.7 based on the calculation of the number of electrons using CV at a 90 $mvs^{-1}$ scan rate (Fig. 4.65A) and the slope value in the plot of $E_{pa}$ vs. pH (Fig. 4.66B) **[219]**.

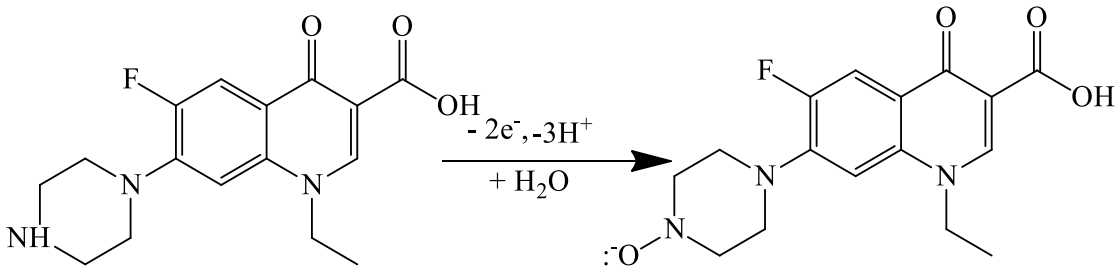


Scheme 4. 7: Proposed reaction mechanism of norfloxacin

### 4.4.8. Accumulation Time and Accumulation Potential

Deposition potential and time of AdSSWV of 100 µM Nor and 200 µM Caff in pH 6.0 PBS were optimized at default 4 mV, 25 mV, and 15 Hz step potential, amplitude, and frequency, respectively. As shown in Fig. 4.67A, the time was varying from 2 to 25 sec. at 0.0 mV deposition potential to optimize deposition time. As shown in Fig. 4.67A inset, the peak current was attained at a common maximum for Nor (peak a) and Caff (peak b) at 15 sec. Therefore, deposition time at 15 sec. was optimized. The potential was also varying from 350 mV to 550 mV at 15 sec. to optimize deposition potential. As shown in Fig. 4.67B and its inset, the peak current was increased from 350 mV to 450 mV for both Nor (peak a) and Caff (peak b), and the increment was slowed down. Therefore, the deposition potential at 450 mV was optimized for the next procedure, indicated by a circle in the inset.

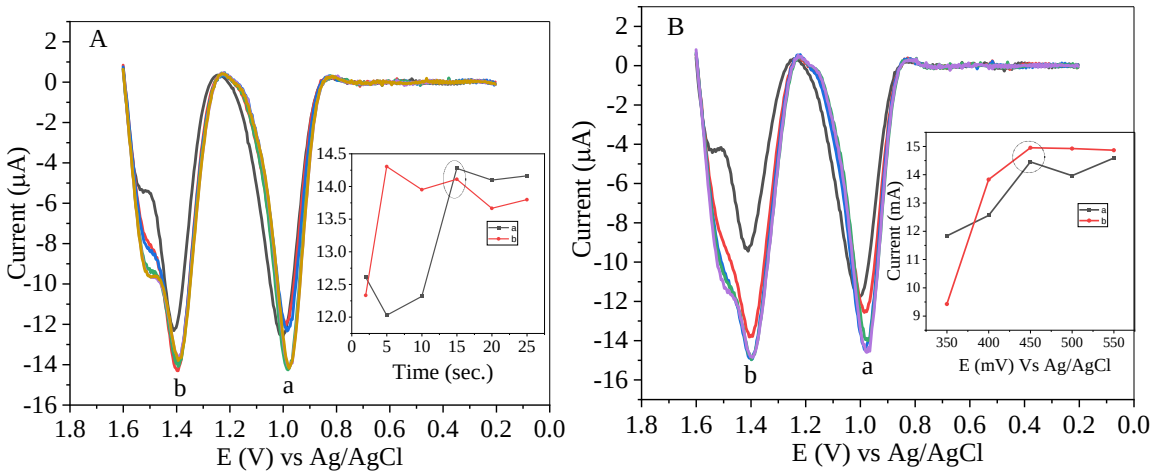

Fig. 4. 67: AdSSWVs of 100 µM Nor (a) and 200 µM Caff (b) at various accumulation times (2, 5, 10, 15, 20, and 25 sec.) and inset: plot of absolute value of current vs. time (A) and AdSSWVs of 100 µM Nor (a) and 200 µM Caff (b) at various accumulation potentials (350, 400, 450, 500, and 550) Inset: Plot of absolute value of current vs. accumulation potential (B) at 4 $mVs^{-1}$ step potentials, 25 mV amplitude, and 15 Hz frequency using poly $[Cu(Reso)_3Cl]$/PGE.

### 4.4.9. Square Wave Voltammeter Parameter Optimization

Determination of Nor and Caff simultaneously using poly $[Cu(Reso)_3Cl]$/PGE can be affected by amplitude, frequency and step potential [199]. Each parameter was optimized using 100 µM Nor and 200 µM Caff at the optimized pH value. The optimization was carried out by varying one variable while maintain the other constant. Therefore, step potential was varied from 2 mV to 12 mV, amplitude from 10 mV to 50 mV, and frequency from 10 Hz to 45 Hz. For both Nor and Caff of all parameters, initially the currents increased and at some point the linearity was lost shown in Figs. 4.68A, B, and C, respectively. Based on lose in linearity, the step potential, amplitude, and frequency were set at 6 mV, 35 mV, and 20 Hz, respectively.

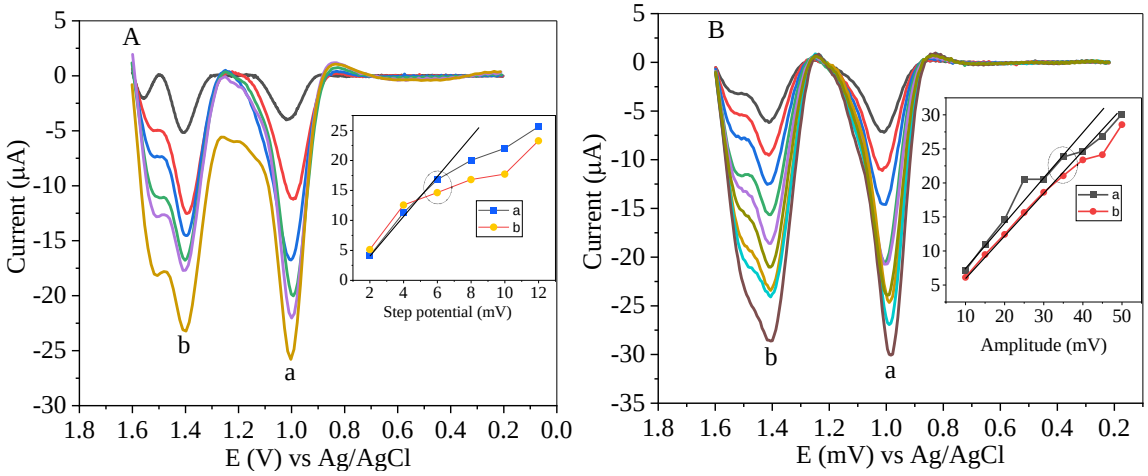

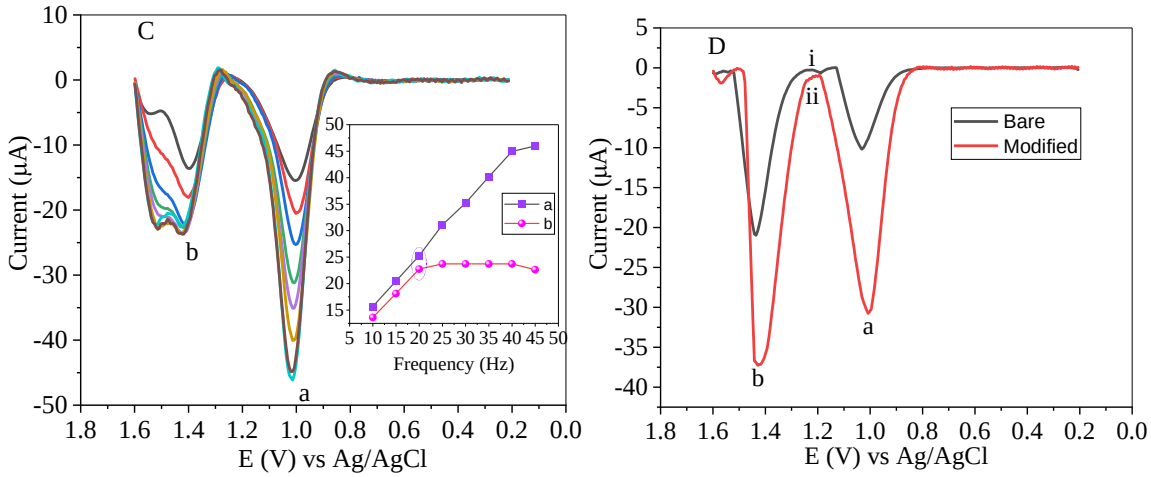


Fig. 4. 68: AdSSWVs of 100 µM Nor (peak a) and 200 µM Caff (peak b) at various step potentials (2, 4, **6**, 8, 10, and 12 mV) (A); at various amplitudes (10, 15, 20, 25, 30, **35**, 40, 45, and 50 mV)(B); at various frequencies (10, 15, **20,** 25, 30, 35, 40, and 45 Hz)(C) with their inset: plot of absolute value of current vs. step potential, amplitude and frequency; and AdSSWVs of 100 µM Nor (a) and 200 µM Caff (b) bare (i) and modified (ii) (D) at 6 $mVs^{-1}$ step potentials, 35 mV amplitude, and 20 Hz frequency using poly [$Cu(Reso)_3Cl$]/PGE.

### 4.4.10. AdSSWV Activity of Nor and Caff

The AdSSWV activity of 100 µM Nor and 200 µM Caff using poly [$Cu(Reso)_3Cl$]/PGE and a unmodified PGE electrodes in the selected parameters has been examined simultaneously and plotted in Fig. 4.68(D). Current and potential of Nor using poly [$Cu(Reso)_3Cl$]/PGE (ii) were 30.76 µA, and 1004 mV (Fig. 4.68D(peak a)), respectively. But as shown in Fig. 4.68D(a), Current and potential of Nor using bare electrode (i) were 10.25 µA and1027 mV, respectively. Therefore, the developed method shows 3.0-fold current enhancement and 23 mV peak potential shift towards lower peak potential. In the case of Caff using poly [$Cu(Reso)_3Cl$]/PGE (Fig. 4.68D(ii)), the peak current was 37.3 µA and the peak potential was 1425 mV(Fig. 4.68D(peak b)). But as shown in Fig. 4.68D(i), the peak current of bare electrode was 20.9 µA and peak potential was 1437 mV. Therefore, the developed method shows 2.0-fold current enhancement and 12 mV

peak potential shift towards lower peak potential. This confirms the developed method has electrocatalytic properties for both Nor and Caff.

### 4.4.11. Method Calibration

The developed AdSSWV based on poly[Cu(Reso)$_3$Cl]/PGE method was calibrated using Nor and Caff standard solutions simultaneously in the range of 5.0 µM to 150 µM and 10.0 µM to 300 µM, respectively. As shown in Fig. 4.69A and Fig. 4.69B, the method calibration is linear in the range of 5.0 µM to 150 µM for Nor (peak a) with the slope value of -0.236. In the case of Caff, the linearity was in the range of 10.0 µM to 300 µM (peak b) with the slope value of -0.098 [220].

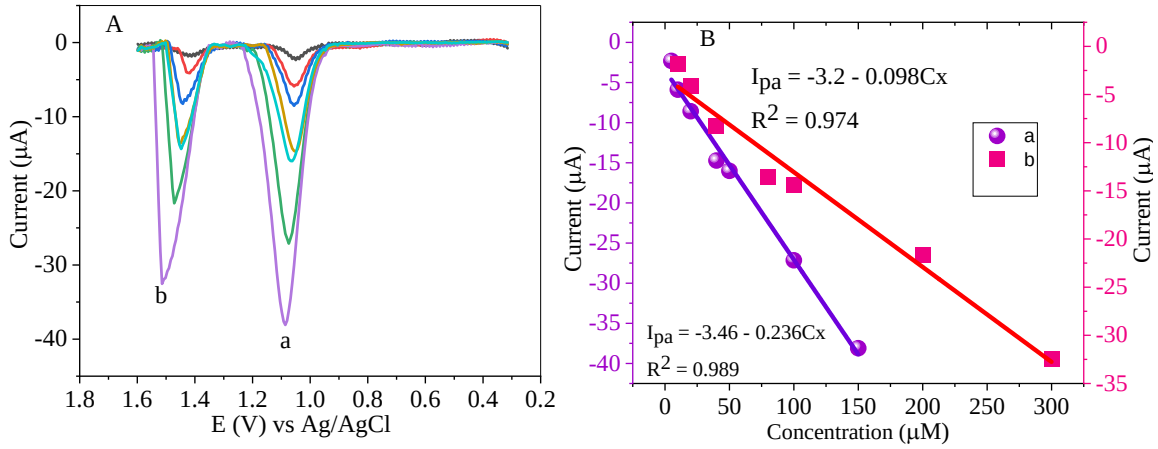


Fig. 4. 69: AdSSWVs of Nor in various concentrations, A(a) (5, 10, 20, 40, 50, 100, and 150 µM) and Caff A(b) (10, 20, 40, 80, 100, 200, and 300 µM) at poly [Cu(Reso)$_3$Cl]/PGE (A) and a plot of current vs. concentration (B) at optimized parameters.

### 4.4.12. Real Sample Analysis

Attempts of determination of Nor in the presence of Caff using UV-Vis spectroscopy method simultaneously was conducted. As we can see in Fig. 4.70, the absorption band of Caff Appear on the characteristic absorption band of Nor but not at point indicated by circle and as the concentration of Caff was increased from (50-150 µM) ‘a’ to ‘d’ the intensity of the peak was also increased but no clear peak separation between

characteristic band of Nor and Caff. Absence of peak separation confirms simultaneous determination of Nor and Caff was not possible using UV-Vis spectroscopy method.

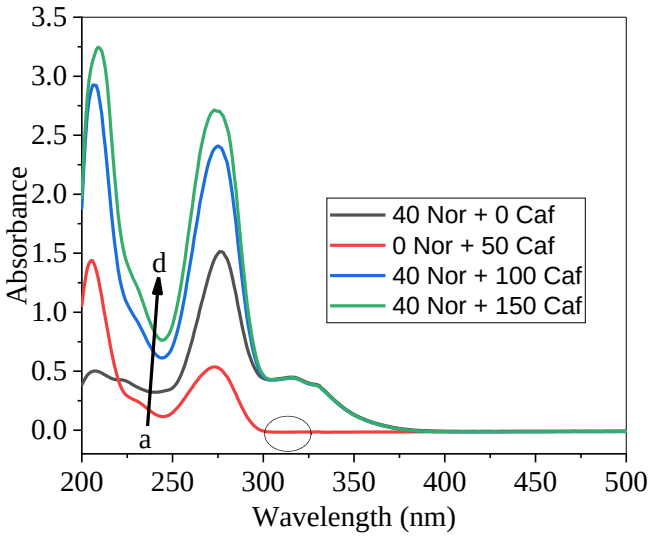


Fig. 4. 70: UV-Vis absorption band of Caff 'a' in the absence Nor and 'c' and 'd' in the presence of 40 µM Nor, 'b' is band of Nor in the absence of Caff in PBS of pH 6.0

#### 4.4.12.1. Tablet Samples from Two Brands

Nor tablet samples in the two brands were analyzed. The first brand was Nofxin in which analysis was conducted in the presence of 100 µM Caff. 20.0 µM nominal tablet concentration was spiked with 20 µM, 40 µM, and 60 µM Nor standard solution and analyzed. The peak intensity of Nor was increased as its concentration increased. But the peak intensity of Caff remained constant as the concentration of Nor was increased as shown in Fig. 4.71. The resulting recovery was in the range of 100.3–103.0 as listed in Table 4.17. This result shows, poly [Cu(Reso)$_3$Cl]/PGE AdSSWV can be applied for the determination of Nor in the presence of Caff effectively.

Table 4. 17: Recovery and pharmaceutical sample analysis results of Nor in Nofxin samples in the presence of 100 µM Caff.

| Un-spiked (µM) | Added Nor (µM) | **Added Caff.** (µM) | **Found** (µM) ± S | % Recovery |
|---|---|---|---|---|
| **20** | 0 | - | 19.78 ± 0.08 | - |

| | | | | |
|---|---|---|---|---|
| **20** | 20 | 100 | 41.2 ± 0.09 | 103.04 |
| **20** | 40 | 100 | 60.5 ± 0.35 | 100.8 |
| **20** | 60 | 100 | 80.2 ± 0.15 | 100.3 |

S = standard division

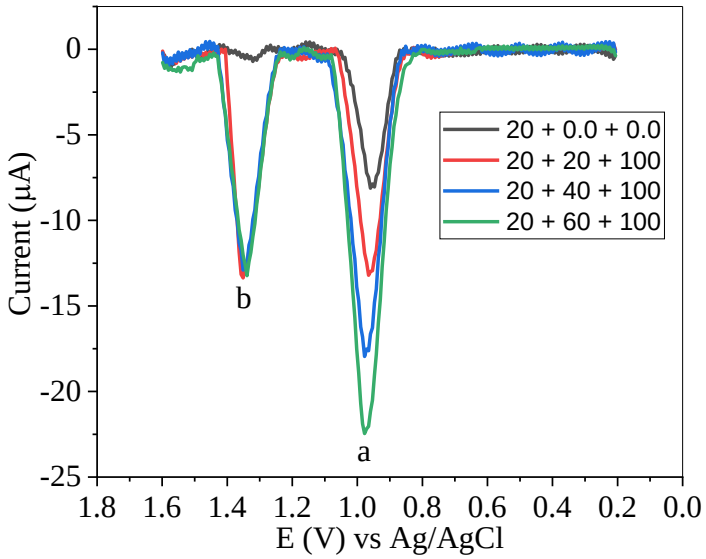


Fig. 4. 71: Background-corrected AdSSWVs of Nofxin (a) spiked with Nor standard solutions in the presence of 100 µM of Caff (b) (20.0 + 0.0 + 0.0, 20.0 + 20.0 + 100, 20.0 + 40.0 + 100, and 20.0 + 60.0 + 100 µM) at poly [Cu(Reso)$_3$Cl]/PGE at the optimized parameters

Similarly Nor analysis in Gyrablock brand analysis was conducted by spiking 20 µM nominal concentration with 20 µM, 40 µM, and 60 µM standard solution of Nor in the presence of 100 µM Caff, and analyzed using AdSSWV (Fig. 4.72). As shown in Table 4.18, the recovery results were in the ranges of 100.4–102.4 for the developed poly [Cu(Reso)$_3$Cl]/PGE AdSSWV method in the presence of 100 µM Caff. The developed poly [Cu(Reso)$_3$Cl]/PGE based AdSSWV results confirms, the developed method can be used for the determination of Nor in Gyrablock brand samples in the presence of Caff.

Table 4. 18: Recovery results of Nor in Gyrablock brand samples in the presence of 100 µM Caff.

| Un-spiked **(µM)** | Added Nor (µM) | **Added Caff (µM)** | **Found** (µM) ± **S** | % Recovery |
|---|---|---|---|---|
| **20** | 0 | ---- | 22.5 ± 0.52 | ---- |
| **20** | 20 | 100 | 40.95 ± 0.20 | 102.38 |
| **20** | 40 | 100 | 60.24 ± 0.10 | 100.4 |
| **20** | 60 | 100 | 80.8 ± 0.15 | 101.0 |

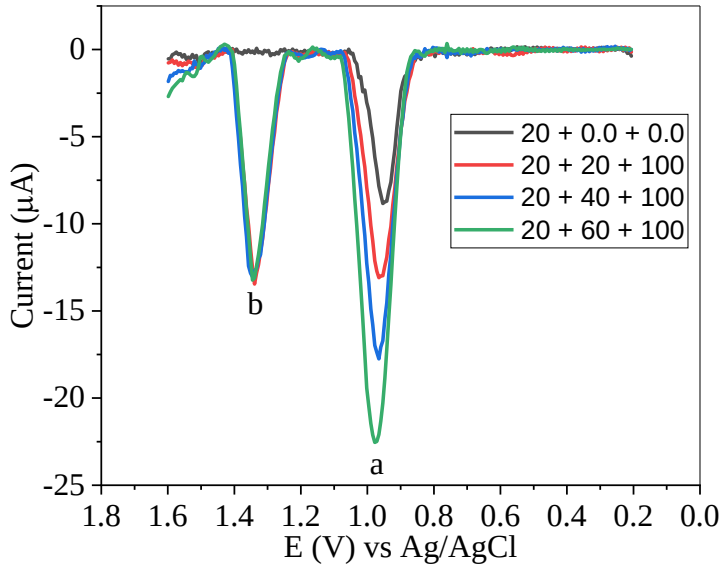


Fig. 4. 72: Background-corrected AdSSWVs of Nor (a) and Caff (b) in Gyrablock tablet spiked with different concentrations of Nor standards (20.0 + 0.0 + 0.0, 20.0 + 20.0 + 100 µM, 20.0 + 40.0 + 100 µM, and 20.0 + 60.0 + 100 µM) using poly [$Cu(Reso)_3Cl$]/PGE at the optimized parameters

### 4.4.12.2. Urine Samples

As indicated in Fig. 4.72, human urine samples were spiked with (40-80 µM), (80-160 µM), and (160-320 µM) of the (Nor-Caff) ratio, respectively, and AdSSWVs was implemented. In the voltammogram shown in Fig. 4.72, the peaks of uric acid, Nor, and Caff were appear, which confirms that the new approach can simultaneously analyze uric

acid, Nor, and Caff without interfering. The non-spiked urine sample showed none quantifiable characteristic peak of Caff. Uric acid Peak (a), and peak (b), the peak of creatinine originating from the urine sample remained nearly constant, while peak (c), the characteristic peak of Nor and peak (d), the characteristic peak of Caff increased with their concentration. The percent recovery ranges from 95.5% to 100.4% for Nor and 98.5% to 100.9% for Caff as listed in Table 4.19, was obtained, which is in the accepted range. This indicates the sample matrices have no effect on (Nor and Caff), and (Nor and Caff) themselves have no effect on uric acid. Consequently, the developed method can be used for identification and quantification of Nor and Caff simultaneously in a urine samples.

Table 4. 19: Recovery results of Nor and Caff in urine samples

| Non-spiked **(µM)** | Added Nor (µM) | **Added Caff (µM)** | **Found Nor** (µM) **± S** | **Found Caff** (µM) **± S** | % Recov. Nor | % Recov. **Caff** |
|---|---|---|---|---|---|---|
| **None** | ---- | ---- | ---- | ---- | ---- | ---- |
| **None** | 40 | 80 | 38.2 ± 0.24 | 80.7 ± 0.05 | 95.5 | 100.9 |
| **None** | 80 | 160 | 79.6 ± 0.5 | 157.6 ± 0.04 | 99.5 | 98.5 |
| **None** | 160 | 320 | 160.6 ± 0.43 | 321.0 ± 0.08 | 100.4 | 100.3 |

None = none quantifiable, S = standard division, and Recov. = Recovery

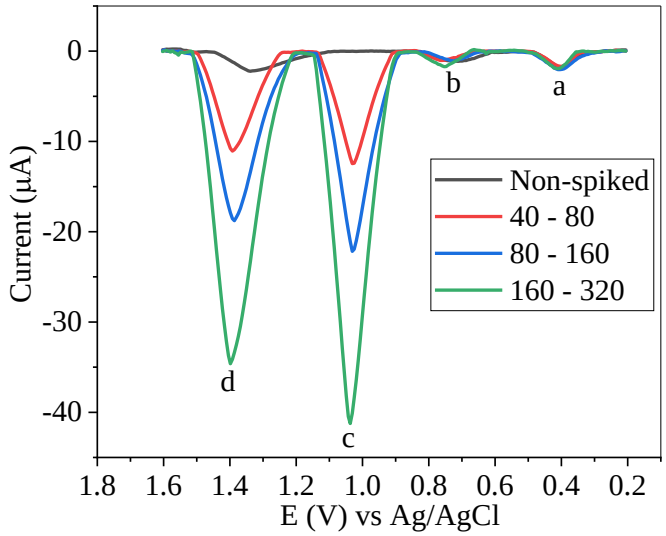


Fig. 4. 73: Background-corrected AdSSWVs of urine sample and spiked with Nor and Caff standards solutions (non-spiked, (40–80), (80–160), and (160–320) µM), respectively using poly [Cu(Reso)$_3$Cl]/PGE at the optimized parameters.

### 4.4.13. Selectivity Study

The selectivity of the proposed method has been evaluated in the presence of paracetamol and uric acid [203]. Different concentration of paracetamol and uric acid were added to study the effect in the analysis of Nor and Caff simultaneously using poly [Cu(Reso)$_3$Cl]/PGE based AdSSWV. The peaks of paracetamol, uric acid, Nor, and Caff were appear separately as shown in Fig. 4.74A(a, b & c) and Fig. 4.74B(a, b & c). As shown, peaks of paracetamol has no peak signal at the characteristic peaks of (Nor and Caff) in Fig. 4.74A, and peaks of uric acid has no signal at the characteristic peak of (Nor and Caff), as shown in Fig. 4.74B. The characteristic peak of (Nor and Caff) not changed with concentration of paracetamol (Fig. 4.74A) and uric acid (Fig. 4.74B). This shows that the presence of paracetamol or uric acid does not interfere in the determination of Nor and Caff simultaneously.

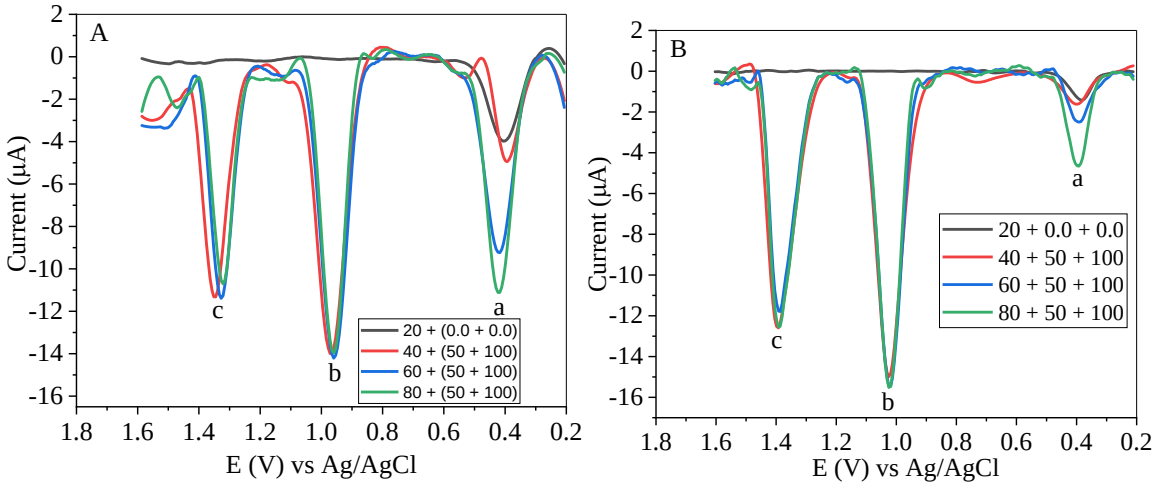


Fig. 4. 74: Background-corrected AdSSWVs of 50 µM Nor (peak b) and 100 µM Caff (peak c) in different concentration of paracetamol (Aa) and uric acid (Ba) (20 + (0.0 + 0.0), 40 + (50 + 100), 60 + (50 + 100), and 80 + (50 + 100) µM) at the optimized parameters

### 4.4.14. Method Repeatability and Reproducibility

AdSSWVs of 100 µM Nor and 200 µM Caff were measured five times using a single poly [Cu(Reso)$_3$Cl]/PGE repeatedly, and similarly for reproducibility, same solution were measured five times using different poly [Cu(Reso)$_3$Cl]/PGE electrode [221]. The plot is shown in Fig. 4.75A for repeatability and Fig. 4.75B for reproducibility. The standard deviation and relative standard deviation of repeatability were 0.443 and 0.8%, respectively whereas the standard deviation and relative standard deviation of repeatability were 1.28 and 2.4%, respectively. Based on the results the method is repeatable and reproducible.

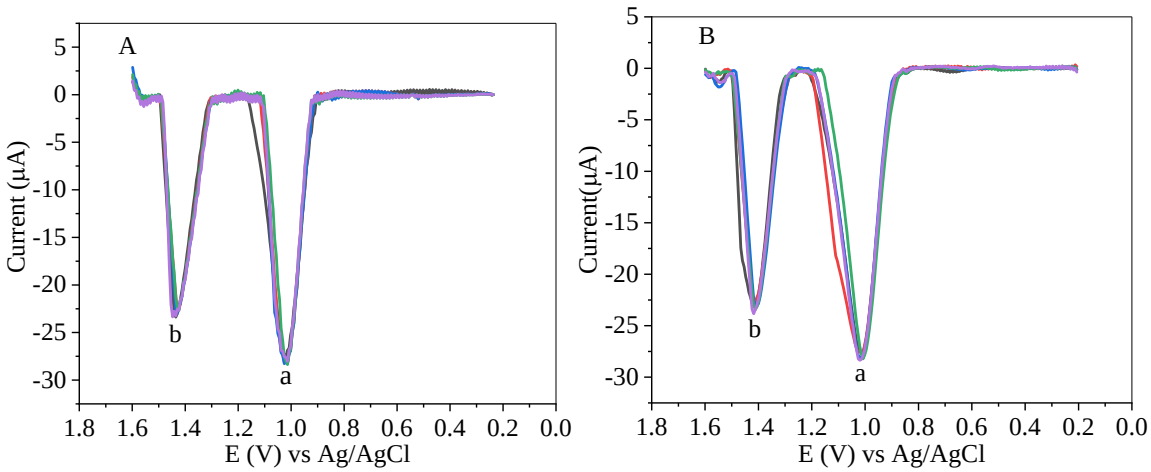


Fig. 4. 75: AdSSWV of reputability (A) and reproducibility (B) of 100 µM Nor (a) and 200 µM Caff (b) using poly [Cu(Reso)$_3$Cl]/PGE at the optimized parameters

### 4.4.15. Comparison with Literature Values

Based on electrode types, LoD, and dynamic range, of this work were compared with some previous works. As we can see in Table 4.20, in this work the dynamic range is relatively wider for both Nor and Caff and a lower LoD for Caff. The LoD of Nor was higher than the reported value. In this work, the developed method was used for the simultaneous determination of Nor and Caff, but previous works did not used for the simultaneous determination of Nor and Caff. PGE electrode was used in this work, which was easily available and cheap compared to other reported electrodes used for the determination of Nor and Caff. Therefore, this method can be a good alternative method for the determination of Nor and Caff in pharmaceuticals and in urine samples.

Table 4. 20: Comparison of different literature values with this work for the determination of Nor and Caff

| Electrode used | Technique | Modified electrode | Dynamic range (µM) | Nor LoD (µM) | Caff LoD (µM) | Reference |
|---|---|---|---|---|---|---|
| **CPE** | SWV | PGM/CPE | 100-900 | ------ | 45 | [21] |
| **GCE** | DPV | Lt/fMWCNT/GCE | 10-110 | ------ | 3.54 | [222] |
| **GCE** | DPV | Lignin/GCE | 6-100 | ------ | 0.84 | [223] |
| **GCE** | SWV | LIG/GCE | 500-5000 | ------ | 60 | [224] |
| **GCE** | DPV | MWCNTs-TOCT/GCE | 0.5-8.0 | 0.1 | ------ | [225] |
| **BPPGS** | SWV | EPPGS | 0.5 -50 | 0.28 | ------ | [226] |
| **BDD** | SWAdSV | APT/BDD | 0.157-12.5 | 0.04 | ------ | [227] |
| **PGE** | AdSSWV | $[Cu(Reso)_3Cl]$/ PGE | 5-150 Nor 10-300 Caff | 1.26 | 3.05 | This work |

# 5. CHAPTER FIVE: CONCLUSION AND RECOMMENDATION

## 5.1. Conclusion

In this work, 0.7 mm HB pencil graphite electrode has been modified and produced poly $[Mn(Chr)_3]Cl_2$/PGE, poly $[Cu(Chr)_2Cl]Cl$/PGE, and poly$[Cu(Reso)_3Cl]$/PGE working electrodes. These developed working electrode were characterized and showed current enhancement, reduced charge transfer resistance, enhanced effective surface area, and reduced peak potential relative to the bare electrode using $[Fe(CN)_6]^{-3/-4}$ as a probe. The electrochemical techniques were optimized to be SWV and AdSSWV. The developed and optimized techniques were applied for the determination of fluoroquinolones in different brands of pharmaceuticals, in milk samples, in urine samples, and in the presence of different potential interferences. The performance of poly ($[Mn(Chr)_3]Cl_2$)/PGE-based SWV and poly$[Cu(Chr)_2Cl]Cl$/PGE-based AdS-SWV were compared with UV-Vis spectrophotometric methods and the new developed electrochemical methods were highly selective and sensitive than UV-Vis spectrophotometric method. The percent recoveries in pharmaceuticals ranged from 84.5 to 114.3%, in urine samples 92.8 to 114.9%, and in milk samples 81.80% to 91.13%. The values of dynamic range, LoD, and sensitivity of the developed method for Cpro were in 1-200 µM, 0.54, and 0.16, respectively. Dynamic range, LoD, and sensitivity for Nor were in 1-100 µM, 0.09, and 0.5, respectively and for Caff were in 10-300 µM, 3.05, and 0.09, respectively. These developed methods can be used to determine the pharmaceutical samples in fluoroquinolones classes and other pharmaceuticals in different sample matrices.

## 5.2. Recommendations

The prepared electrochemical sensors in this work are highly sensitive and selective to analyte relative to UV-Vis spectrophotometry. We recommend that, any interested scholars and laboratory experts in the area can apply the developed methodologies for quality control, in clinical diagnosis, and for fieldwork analysis mainly in the presence of scarcity of glassy carbon electrode. It is better to investigate the morphology of the surface of the modified electrode, and distribution patterns of the surface deposited materials after modification by using Scanning Electron Microscopy (SEM), XRD, Transmission Electron Microscopy (TEM), and XPS, in order to obtain full information of the developed sensors.

# 6. REFERENCES


1. Fàbrega, A., et al., *Mechanism of action of and resistance to quinolones.* Microb Biotechnol, 2009. **2**(1): p. 40-61.

2. Chanie, G., et al., *Selective square wave voltammetric determination of tinidazole in pharmaceutical formulations, and human urine samples using poly (bis (2, 2'-bipyridine) diresorcinolateruthenium (III) chloride) modified glassy carbon electrode.* Sensing and Bio-Sensing Research, 2024. **43**: p. 100607.

3. Baeza, A.N., et al., *The Ultratrace Determination of Fluoroquinolones in River Water Samples by an Online Solid-Phase Extraction Method Using a Molecularly Imprinted Polymer as a Selective Sorbent.* Molecules, 2022. **27**(23): p. 8120.

4. Dönmez, F., Y. Yardım, and Z. Şentürk, *Electroanalytical determination of enrofloxacin based on the enhancement effect of the anionic surfactant at anodically pretreated boron-doped diamond electrode.* Diamond and Related Materials, 2018. **84**: p. 95-102.

5. Sharma, P.C., A. Jain, and S. Jain, *Fluoroquinolone antibacterials: a review on chemistry, microbiology and therapeutic prospects.* Acta Pol Pharm, 2009. **66**(6): p. 587-604.

6. Aldred, K.J., R.J. Kerns, and N. Osheroff, *Mechanism of quinolone action and resistance.* Biochemistry, 2014. **53**(10): p. 1565-1574.

7. Redgrave, L.S., et al., *Fluoroquinolone resistance: mechanisms, impact on bacteria, and role in evolutionary success.* Trends in microbiology, 2014. **22**(8): p. 438-445.

8. Diabetes, N.I.o., Digestive, and K. Diseases, *LiverTox: clinical and research information on drug-induced liver injury*. 2012: National Institute of Diabetes and Digestive and Kidney Diseases.

9. Correia, S., et al., *Mechanisms of quinolone action and resistance: where do we stand?* Journal of medical microbiology, 2017. **66**(5): p. 551-559.

10. Stahlmann, R. and H.M. Lode, *Risks associated with the therapeutic use of fluoroquinolones.* Expert Opinion on Drug Safety, 2013. **12**(4): p. 497-505.

11. Blondeau, J.M., *Fluoroquinolones: mechanism of action, classification, and development of resistance.* Survey of Ophthalmology, 2004. **49**(2, Supplement 2): p. S73-S78.

12. Kloskowski, T., N. Gurtowska, and T. Drewa, *Does ciprofloxacin have an obverse and a reverse?* Pulmonary Pharmacology & Therapeutics, 2010. **23**(5): p. 373-375.

13. Zhang, G.-F., et al., *Ciprofloxacin derivatives and their antibacterial activities.* European Journal of Medicinal Chemistry, 2018. **146**: p. 599-612.

14. Chen, X., et al., *Effects of norfloxacin, copper, and their interactions on microbial communities in estuarine sediment.* Environmental Research, 2022. **212**: p. 113506.

15. Wang, F., et al., *Effects of antibiotic norfloxacin on the degradation and enantioselectivity of the herbicides in aquatic environment.* Ecotoxicology and Environmental Safety, 2021. **208**: p. 111717.

16. Su, Y., et al., *Unraveling the mechanism of norfloxacin removal and fate of antibiotics resistance genes (ARGs) in the sulfur-mediated autotrophic denitrification via metagenomic and metatranscriptomic analyses.* Science of The Total Environment, 2024. **922**: p. 171328.

17. Hassall, J., et al., *Limitations of current techniques in clinical antimicrobial resistance diagnosis: examples and future prospects.* npj Antimicrobials and Resistance, 2024. **2**(1): p. 16.

18. Zhang, G.F., et al., *Ciprofloxacin derivatives and their antibacterial activities.* Eur J Med Chem, 2018. **146**: p. 599-612.

19. Pawar, B., et al., *Chapter 1 - Understanding pharmacotoxicology*, in *Essentials of Pharmatoxicology in Drug Research*, R. Tekade, Editor. 2023, Academic Press. p. 1-28.

20. Bushra, R., N. Aslam, and A.Y. Khan, *Food-drug interactions.* Oman Med J, 2011. **26**(2): p. 77-83.

21. Yenealem, D., et al., *Electrochemical detection and characterization of caffeine in selected tea samples using polyglycine modified Carbon paste electrode.* South African Journal of Chemical Engineering, 2025. **51**: p. 225-231.

22. Tasić, Ž.Z., et al. *Recent Advances in Electrochemical Sensors for Caffeine Determination*. Sensors, 2022. **22**, DOI: 10.3390/s22239185.

23. Samoggia, A. and T. Rezzaghi, *The Consumption of Caffeine-Containing Products to Enhance Sports Performance: An Application of an Extended Model of the Theory of Planned Behavior.* Nutrients, 2021. **13**(2).

24. Abdel Hameed, E.A., et al., *Two Eco-Friendly Chromatographic Methods Evaluated by GAPI for Simultaneous Determination of the Fluoroquinolones Moxifloxacin, Levofloxacin, and Gemifloxacin in Their Pharmaceutical Products.* Separations, 2022. **9**(11): p. 330.

25. Baeza, A., et al., *The ultratrace determination of fluoroquinolones in river water samples by an online solid-phase extraction method using a molecularly imprinted polymer as a selective sorbent.* Molecules, 2022. **27**(23): p. 8120.

26. Nguyen, T.D., et al., *Determination of fluoroquinolones in pharmaceutical formulations by extractive spectrophotometric methods using ion-pair complex formation with bromothymol blue.* Journal of analytical methods in chemistry, 2018. **2018**.

27. Speltini, A., et al., *Fluoroquinolone residues in compost by green enhanced microwave-assisted extraction followed by ultra performance liquid chromatography tandem mass spectrometry.* Journal of Chromatography A, 2015. **1410**: p. 44-50.

28. Tlili, I., et al., *Simultaneous detection of antibiotics and other drug residues in the dissolved and particulate phases of water by an off-line SPE combined with on-line SPE-LC-MS/MS: Method development and application.* Science of the Total Environment, 2016. **563**: p. 424-433.

29. Elgendy, K., et al., *Rapid HPLC determination of ciprofloxacin, ofloxacin, and marbofloxacin alone or in a mixture.* Results in Chemistry, 2023. **5**: p. 100749.

30. Scherer, R., et al., *Determination of Ciprofloxacin in Pharmaceutical Formulations Using HPLC Method with UV Detection.* Indian J Pharm Sci, 2014. **76**(6): p. 541-4.

31. Mahmoud, T.Y., I.S. Hamza, and A.L. Jarallah *Spectrophotometric Method for the Determination of Ciprofloxacin in Pure and Pharmaceutical Preparations: Development and Validation*. Engineering Proceedings, 2023. **59**, DOI: 10.3390/engproc2023059164.

32. Córdoba-Borrego, M., M. Córdoba-Díaz, and D. Córdoba-Díaz, *Validation of a high-performance liquid chromatographic method for the determination of norfloxacin and its application to stability studies (photo-stability study of norfloxacin).* Journal of Pharmaceutical and Biomedical Analysis, 1999. **18**(6): p. 919-926.

33. Al-Tamrah, S.A., M.A. Abdalla, and A.A. Al-Otibi, *Spectrophotometric determination of norfloxacin using bromophenol blue.* Arabian Journal of Chemistry, 2019. **12**(8): p. 3993-3997.

34. Goyal, R.N., A.R.S. Rana, and H. Chasta, *Electrochemical sensor for the sensitive determination of norfloxacin in human urine and pharmaceuticals.* Bioelectrochemistry, 2012. **83**: p. 46-51.

35. Pokhrel, P., et al., *A simple HPLC Method for the Determination of Caffeine Content in Tea and Coffee.* Journal of Food Science and Technology Nepal, 2016. **9**: p. 74.

36. Vuletić, N., L. Bardić, and R. Odžak, *Spectrophotometric determining of caffeine content in the selection of teas, soft and energy drinks available on the Croatian market.* Food research (Kuala Lumpur), 2021. **5**(2): p. 325-330.

37. Sri, K., B. Hema, and M. Sumakanth, *NOVEL UV SPECTROSCOPIC METHOD FOR QUANTIFICATION OF CAFFEINE IN MARKETED ENERGY DRINKS.* International Journal of Current Pharmaceutical Research, 2023: p. 47-50.

38. Singh, B.R., et al., *Determination of caffeine content in coffee using Fourier transform infra-red spectroscopy in combination with attenuated total reflectance technique: a bioanalytical chemistry experiment for biochemists.* Biochemical Education, 1998. **26**(3): p. 243-247.

39. Daghbouche, Y., et al., *Flow Injection Fourier Transform Infrared Determination of Caffeine in Soft Drinks.* Analytical Chemistry, 1997. **69**(6): p. 1086-1091.

40. Ostojic, J., et al., *Advantages of an Electrochemical Method Compared to the Spectrophotometric Kinetic Study of Peroxidase Inhibition by Boroxine Derivative.* Molecules, 2017. **22**: p. 1120.

41. Chang, S.K., A. Ismail, and Z.A.M. Daud, *Ascorbic Acid: Properties, Determination and Uses*, in *Encyclopedia of Food and Health*, B. Caballero, P.M. Finglas, and F. Toldrá, Editors. 2016, Academic Press: Oxford. p. 275-284.

42. Ünlüer, Ö.B., et al., *Chapter 12 - Future of the modern age of analytical chemistry: Nanominiaturization*, in *Handbook on Miniaturization in Analytical Chemistry*, C.M. Hussain, Editor. 2020, Elsevier. p. 277-296.

43. Ducey, M.W., et al., *2.25 - Microdialysis Sampling in the Brain: Analytical Approaches and Challenges*, in *Comprehensive Sampling and Sample Preparation*, J. Pawliszyn, Editor. 2012, Academic Press: Oxford. p. 535-557.

44. Pozo-Ayuso, D.F., M. Castaño-Álvarez, and A. Fernández-la-Villa, *Chapter 6 - Enhancing electrochemical performance by using redox cycling with interdigitated electrodes*, in *Laboratory Methods in Dynamic Electroanalysis*, M.T. Fernandez Abedul, Editor. 2020, Elsevier. p. 57-65.

45. Benedito da Silva, O. and S.A.S. Machado, *Evaluation of the detection and quantification limits in electroanalysis using two popular methods: application in the case study of paraquat determination.* Analytical Methods, 2012. **4**(8): p. 2348-2354.

46. Hasnat, M., et al., *Electrochemical Methods for the Detection of Toxic As(III) and As(V) from Natural Water*, in *Combined Application of Physico-Chemical & Microbiological Processes for Industrial Effluent Treatment Plant*, M. Shah and A. Banerjee, Editors. 2020, Springer Singapore: Singapore. p. 315-337.

47. Cassoux, P., L. Valade, and P.L. Fabre, *1.44 - Electrochemical Methods, Electrocrystallization*, in *Comprehensive Coordination Chemistry II*, J.A. McCleverty and T.J. Meyer, Editors. 2003, Pergamon: Oxford. p. 761-773.

48. Uslu, B. and S. Ozkan, *Electroanalytical Application of Carbon Based Electrodes to the Pharmaceuticals.* Analytical Letters - ANAL LETT, 2007. **40**: p. 817-853.

49. Kalathil, S., S.A. Patil, and D. Pant, *Microbial Fuel Cells: Electrode Materials*, in *Encyclopedia of Interfacial Chemistry*, K. Wandelt, Editor. 2018, Elsevier: Oxford. p. 309-318.

50. Arfin, T., *9 - Emerging trends in lab-on-a-chip for biosensing applications*, in *Functionalized Nanomaterials Based Devices for Environmental Applications*, C.M. Hussain, S.K. Shukla, and G.M. Joshi, Editors. 2021, Elsevier. p. 199-218.

51. Abdel-Aziz, A.M., H.H. Hassan, and I.H.A. Badr, *Activated Glassy Carbon Electrode as an Electrochemical Sensing Platform for the Determination of 4-Nitrophenol and Dopamine in Real Samples.* ACS Omega, 2022. **7**(38): p. 34127-34135.

52. Navratil, R., et al., *Polymer lead pencil graphite as electrode material: Voltammetric, XPS and Raman study*. Journal of Electroanalytical Chemistry, 2016. **783**: p. 152-160.

53. Alves, G., et al., *Disposable Pencil Graphite Electrode for Ciprofloxacin Determination in Pharmaceutical Formulations by Square Wave Voltammetry.* Electroanalysis, 2020. **33**.

54. Pinar, P.N.T., *Electrooxidation and Low-tech Determination of Pantoprazole on a Disposable Pencil Graphite Electrode by the use of Cationic Surfactant.* Acta Chim Slov, 2020. **67**(1): p. 212-220.

55. Simões, F.R. and M.G. Xavier, *6 - Electrochemical Sensors*, in *Nanoscience and its Applications*, A.L. Da Róz, et al., Editors. 2017, William Andrew Publishing. p. 155-178.

56. Ananda Murthy, H.C., et al., *17 - Functionalized metal and metal oxide nanomaterial-based electrochemical sensors*, in *Functionalized Nanomaterial-Based Electrochemical Sensors*, C.M. Hussain and J.G. Manjunatha, Editors. 2022, Woodhead Publishing. p. 369-392.

57. Baranwal, J., et al., *Electrochemical Sensors and Their Applications: A Review.* Chemosensors, 2022. **10**(9): p. 363.

58. Edwards, G.A., A.J. Bergren, and M.D. Porter, *8 - Chemically Modified Electrodes*, in *Handbook of Electrochemistry*, C.G. Zoski, Editor. 2007, Elsevier: Amsterdam. p. 295-327.

59. Forner-Cuenca, A. and F.R. Brushett, *Engineering porous electrodes for next-generation redox flow batteries: recent progress and opportunities.* Current Opinion in Electrochemistry, 2019. **18**: p. 113-122.

60. Murthy, H.C.A. and H.P. Nagaswarupa, *Chapter 3 - Novel trends for synthesis of carbon nanomaterial-based sensors*, in *Carbon Nanomaterials-Based Sensors*, J.G. Manjunatha and C.M. Hussain, Editors. 2022, Elsevier. p. 29-42.

61. Gupte, T. and T. Pradeep, *Chapter 3 - Nanosensors for water quality monitoring*, in *Separation Science and Technology*, S. Ahuja, Editor. 2022, Academic Press. p. 37-53.

62. Rani, G., J. Rajesh Banu, and K.N. Yogalakshmi, *Chapter 18 - Electrode modification and its application in microbial electrolysis cell*, in *Scaling Up of Microbial Electrochemical Systems*, D.A. Jadhav, et al., Editors. 2022, Elsevier. p. 339-357.

63. Fomo, G., et al., *Electrochemical Polymerization*. 2019. p. 105-131.

64. Tajik, S., et al., *Recent developments in conducting polymers: applications for electrochemistry.* RSC Adv, 2020. **10**(62): p. 37834-37856.

65. Turunc, E., I. Gumus, and H. Arslan, *Redox active Co(II) complex modified carbon paste electrode for the determination of dopamine.* Materials Chemistry and Physics, 2020. **243**: p. 122597.

66. Henthorn, J.T., S. Lin, and T. Agapie, *Combination of Redox-Active Ligand and Lewis Acid for Dioxygen Reduction with π-Bound Molybdenum− Quinonoid Complexes.* Journal of the American Chemical Society, 2015. **137**(4): p. 1458-1464.

67. Li, J., et al. *Electrocatalytic CO2 Reduction and H2 Evolution by a Copper (II) Complex with Redox-Active Ligand*. Molecules, 2022. **27**, DOI: 10.3390/molecules27041399.

68. Bhatt, S. and S. Chatterjee, *Fluoroquinolone antibiotics: Occurrence, mode of action, resistance, environmental detection, and remediation – A comprehensive review.* Environmental Pollution, 2022. **315**: p. 120440.

69. Redgrave, L.S., et al., *Fluoroquinolone resistance: mechanisms, impact on bacteria, and role in evolutionary success.* Trends in Microbiology, 2014. **22**(8): p. 438-445.

70. Harris, J.B. and E.T. Ryan, *102 - Enteric Fever and Other Causes of Fever and Abdominal Symptoms*, in *Mandell, Douglas, and Bennett's Principles and Practice of Infectious Diseases (Eighth Edition)*, J.E. Bennett, R. Dolin, and M.J. Blaser, Editors. 2015, W.B. Saunders: Philadelphia. p. 1270-1282.e3.

71. Baggio, D. and M.R. Ananda-Rajah, *Fluoroquinolone antibiotics and adverse events.* Aust Prescr, 2021. **44**(5): p. 161-164.

72. Măgeruşan, L., et al. *Analytical Applicability of Graphene-Modified Electrode in Sunset Yellow Electrochemical Assay*. Sensors, 2023. **23**, DOI: 10.3390/s23042160.

73. Baccarin, M., P. Cervini, and E.T.G. Cavalheiro, *Comparative performances of a bare graphite-polyurethane composite electrode unmodified and modified with graphene and carbon nanotubes in the electrochemical determination of escitalopram.* Talanta, 2018. **178**: p. 1024-1032.

74. Morrin, A., *Sensors | Chemically Modified Electrodes ☆*, in *Encyclopedia of Analytical Science (Third Edition)*, P. Worsfold, et al., Editors. 2019, Academic Press: Oxford. p. 161-171.

75. Park, C., et al., *Enhancement of electrode performance through surface modification using carbon nanotubes and porous gold nanostructures.* Nanotechnology, 2021. **32**(50).

76. Kassa, A., G.T. Tigineh, and A. Abebe, *Electrochemical Determination of Chloroquine Phosphate in Real Samples Using a Diresorcinate-1,10-phenanthrolinecobalt(II)-Modified Glassy Carbon Electrode.* ChemistryOpen, 2023. **12**(3): p. e202300004.

77. Gashu, M., et al., *Poly(bis(2,2'-bipyridine) hydroxy Copper(II) iodide modified glassy carbon electrode for electrochemical determination of chloroquine in pharmaceuticals and biological samples.* Sensing and Bio-Sensing Research, 2023. **42**: p. 100598.

78. Metto, M., et al., *Selective and sensitive electroanalytical biosensor based on Poly([Cu(H2O)2P2]I2)/GCE for the determination of esomeprazole in pharmaceutical formulations and biological fluid samples.* International Journal of Electrochemical Science, 2024. **19**(11): p. 100837.

79. Kassa, A., et al., *Ethylendiaminetetrakis(1,10-phenanthroline)dicopper(II) chloride: Synthesis and application for voltammetric determination of doxycycline in real samples.* Microchemical Journal, 2024. **207**: p. 112038.

80. Huang, W.-C. and I.C. Tang, *Chapter 8 - Bacterial and Yeast Cultures – Process Characteristics, Products, and Applications*, in *Bioprocessing for Value-Added Products from Renewable Resources*, S.-T. Yang, Editor. 2007, Elsevier: Amsterdam. p. 185-223.

81. Etebu, E. and I. Arikekpar, *Antibiotics: Classification and mechanisms of action with emphasis on molecular perspectives.* International Journal of Applied Microbiology and Biotechnology Research, 2016. **4**: p. 90-101.

82. Swallow, S., *Chapter Two - Fluorine in Medicinal Chemistry*, in *Progress in Medicinal Chemistry*, G. Lawton and D.R. Witty, Editors. 2015, Elsevier. p. 65-133.

83. Ericsson, C.D., *Chapter 8 - Traveler's Diarrhea: Prevention and Self-Treatment*, in *The Travel and Tropical Medicine Manual (Fifth Edition)*, C.A. Sanford, P.S. Pottinger, and E.C. Jong, Editors. 2017, Elsevier. p. 112-120.

84. Aldred, K.J., R.J. Kerns, and N. Osheroff, *Mechanism of quinolone action and resistance.* Biochemistry, 2014. **53**(10): p. 1565-74.

85. Sandra Georgina, S.-G., et al., *Mechanisms of Resistance to Quinolones*, in *Antimicrobial Resistance*, M. Mihai, et al., Editors. 2020, IntechOpen: Rijeka. p. Ch. 2.

86. Shumyantseva, V.V., et al., *Predicting drug–drug interactions by electrochemically driven cytochrome P450 3A4 reactions.* 2022. **37**(3): p. 241-248.

87. Kennedy, C., L. Brewer, and D. Williams, *Drug interactions.* Medicine, 2020. **48**(7): p. 450-455.

88. Cheng, L. and H. Wong, *Food Effects on Oral Drug Absorption: Application of Physiologically-Based Pharmacokinetic Modeling as a Predictive Tool.* Pharmaceutics, 2020. **12**(7).

89. He, K. and L. Blaney, *Systematic optimization of an SPE with HPLC-FLD method for fluoroquinolone detection in wastewater.* Journal of Hazardous Materials, 2015. **282**: p. 96-105.

90. Golet, E.M., et al., *Trace Determination of Fluoroquinolone Antibacterial Agents in Urban Wastewater by Solid-Phase Extraction and Liquid Chromatography with Fluorescence Detection.* Analytical Chemistry, 2001. **73**(15): p. 3632-3638.

91. Holtzapple, C.K., S.A. Buckley, and L.H. Stanker, *Determination of fluoroquinolones in serum using an on-line clean-up column coupled to high-performance immunoaffinity–reversed-phase liquid chromatography.* Journal of Chromatography B: Biomedical Sciences and Applications, 2001. **754**(1): p. 1-9.

92. Nguyen, T.D., et al., *Determination of Fluoroquinolones in Pharmaceutical Formulations by Extractive Spectrophotometric Methods Using Ion-Pair Complex Formation with Bromothymol Blue.* Journal of Analytical Methods in Chemistry, 2018. **2018**: p. 8436948.

93. Xu, H., et al., *Analysis of Fluoroquinolones in Animal Feed Based on Microwave-Assisted Extraction by LC–MS–MS Determination.* Chromatographia, 2011. **74**(3): p. 267-274.

94. Da Silva Santos, F., et al., *Review—Recent Advances of Electrochemical Techniques in Food, Energy, Environment, and Forensic Applications.* ECS Sensors Plus, 2022. **1**(1): p. 013603.

95. Chang, H.-W., et al. *Electrochemical Organophosphorus Pesticide Detection Using Nanostructured Gold-Modified Electrodes*. Sensors, 2022. **22**, DOI: 10.3390/s22249938.

96. Kumunda, C., et al., *Electrochemical Detection of Environmental Pollutants Based on Graphene Derivatives: A Review*. Frontiers in Materials, 2021. **7**.

97. Dong, S. and Z. Peng, *SENSORS | Chemically Modified Electrodes*, in *Encyclopedia of Analytical Science (Second Edition)*, P. Worsfold, A. Townshend, and C. Poole, Editors. 2005, Elsevier: Oxford. p. 245-254.

98. Cruz-Navarro, J.A., et al. *Recent Advances in the Use of Transition-Metal Porphyrin and Phthalocyanine Complexes as Electro-Catalyst Materials on Modified Electrodes for Electroanalytical Sensing Applications*. Solids, 2021. **2**, 212-231 DOI: 10.3390/solids2020014.

99. Cruz-Navarro, J.A., et al., *Progress in the use of electrodes modified with coordination compounds for methanol electro-oxidation.* Inorganica Chimica Acta, 2021. **520**: p. 120293.

100. Scholz, F., *Voltammetric techniques of analysis: the essentials.* ChemTexts, 2015. **1**(4): p. 17.

101. Rezaei, B. and N. Irannejad, *Chapter 2 - Electrochemical detection techniques in biosensor applications*, in *Electrochemical Biosensors*, A.A. Ensafi, Editor. 2019, Elsevier. p. 11-43.

102. Makwakwa, T., et al., *Optimization of Square Wave Voltammetry (SWV) Parameters by Design of Experiment (DoE) Methodologies for the Determination of Mifepristone at Glassy Carbon Electrode (GCE).* Electroanalysis, 2021. **34**.

103. Baranwal, J., et al. *Electrochemical Sensors and Their Applications: A Review*. Chemosensors, 2022. **10**, DOI: 10.3390/chemosensors10090363.

104. Faridbod, F., V.K. Gupta, and H.A. Zamani, *Electrochemical Sensors and Biosensors.* International Journal of Electrochemistry, 2011. **2011**: p. 352546.

105. Heard, D.M. and A.J. Lennox, *Electrode materials in modern organic electrochemistry.* Angewandte Chemie International Edition, 2020. **59**(43): p. 18866-18884.

106. Arulraj, A. and S.T. Nishanthi, *Chapter 13 - 2D materials–based flexible supercapacitors for high energy storage devices*, in *Nanostructured, Functional, and Flexible Materials for Energy Conversion and Storage Systems*, A. Pandikumar and P. Rameshkumar, Editors. 2020, Elsevier. p. 417-436.

107. Bhattacharyya, S.K., S. Banerjee, and N. Chandra Das, *22 - Polymer-graphene composite in hydrogen production*, in *Polymer Nanocomposites Containing Graphene*, M. Rahaman, et al., Editors. 2022, Woodhead Publishing. p. 639-682.

108. Makarychev-Mikhailov, S., A. Shvarev, and E. Bakker, *CHAPTER 4 - New trends in ion-selective electrodes*, in *Electrochemical Sensors, Biosensors and their Biomedical Applications*, X. Zhang, H. Ju, and J. Wang, Editors. 2008, Academic Press: San Diego. p. 71-114.

109. Kahlert, H., *Reference Electrodes*, in *Electroanalytical Methods: Guide to Experiments and Applications*, F. Scholz, Editor. 2002, Springer Berlin Heidelberg: Berlin, Heidelberg. p. 261-278.

110. Oiye, É.N., et al., *Electrochemical Sensors Containing Schiff Bases and their Transition Metal Complexes to Detect Analytes of Forensic, Pharmaceutical and Environmental Interest. A Review.* Critical Reviews in Analytical Chemistry, 2019. **49**(6): p. 488-509.

111. Sarakatsanou, C., S. Karastogianni, and S. Girousi *Promising Electrode Surfaces, Modified with Nanoparticles, in the Sensitive and Selective Electroanalytical Determination of Antibiotics: A Review*. Applied Sciences, 2023. **13**, DOI: 10.3390/app13095391.

112. Elattar, R.H., et al., *Applications of metal complexes in analytical chemistry: A review article.* Coordination Chemistry Reviews, 2024. **501**: p. 215568.

113. Wałęsa-Chorab, M., et al., *Electrochromism and electrochemical properties of complexes of transition metal ions with benzimidazole-based ligand.* RSC advances, 2017. **7**(80): p. 50858-50867.

114. Baryshnikova, S.V. and A.I. Poddel'sky, *Heteroligand Metal Complexes with Extended Redox Properties Based on Redox-Active Chelating Ligands of o-Quinone Type and Ferrocene.* Molecules, 2022. **27**(12): p. 3928.

115. Hanusa, T.P., *Cyanide complexes of the transition metals.* Encyclopedia of inorganic chemistry, 2006.

116. Bencini, A. and V. Lippolis, *1,10-Phenanthroline: A versatile building block for the construction of ligands for various purposes.* Coordination Chemistry Reviews - COORD CHEM REV, 2010. **254**: p. 2096-2180.

117. Scarpi-Luttenauer, M., et al., *Bent 1,10-Phenanthroline Ligands within Octahedral Complexes Constructed around a TiO4N2 Core.* Inorganic Chemistry, 2020. **59**(17): p. 12005-12016.

118. Kaur, G., M.I.J. Polson, and R.M. Hartshorn, *4'-(2-Methylphenyl)-2,2':6',2''-terpyridine: coordination chemistry with Ni(II), Cu(II), Zn(II) and Ag(I).* Journal of Coordination Chemistry, 2019. **72**(5-7): p. 1013-1035.

119. Chiririwa, H. and O. Aoyi, *Synthesis and Characterization of New Tetradentate Ligands.* Iranian Journal of Science and Technology, Transactions A: Science, 2017. **41**(4): p. 1003-1009.

120. Lee, C.-H., et al., *Isomeric Tetradentate Ligand-Containing Cyclometalated Gold(III) Complexes.* Journal of the American Chemical Society, 2020. **142**(1): p. 520-529.

121. Debalke, A., et al., *Synthesis of a novel diaquabis(1,10-phenanthroline)copper(II)chloride complex and its voltammetric application for detection of amoxicillin in pharmaceutical and biological samples.* Heliyon, 2022. **8**(10): p. e11199.

122. Chanie, G., et al., *Selective square wave voltammetric determination of tinidazole in pharmaceutical formulations, and human urine samples using poly(bis(2,2'-bipyridine)diresorcinolateruthenium(III) chloride) modified glassy carbon electrode.* Sensing and Bio-Sensing Research, 2024. **43**: p. 100607.

123. Kassa, A., G.T. Tigineh, and A. Abebe, *Electrochemical Determination of Chloroquine Phosphate in Real Samples Using a Diresorcinate-1, 10-phenanthrolinecobalt (II)-Modified Glassy Carbon Electrode.* ChemistryOpen, 2023. **12**(3): p. e202300004.

124. Kaliyaraj Selva Kumar, A., et al., *A mini-review: How reliable is the drop casting technique?* Electrochemistry Communications, 2020. **121**: p. 106867.

125. Mullemwar, S.Y., N. Thejo Kalyani, and S.J. Dhoble, *14 - OLEDs: Emerging technology trends and designs*, in *Phosphor Handbook*, V.B. Pawade, et al., Editors. 2023, Woodhead Publishing. p. 307-328.

126. Yilbas, B.S., A. Al-Sharafi, and H. Ali, *Chapter 3 - Surfaces for Self-Cleaning*, in *Self-Cleaning of Surfaces and Water Droplet Mobility*, B.S. Yilbas, A. Al-Sharafi, and H. Ali, Editors. 2019, Elsevier. p. 45-98.

127. Hong, M., J. Zou, and Z.-G. Chen, *4 - Synthesis of thermoelectric materials*, in *Thermoelectricity and Advanced Thermoelectric Materials*, R. Kumar and R. Singh, Editors. 2021, Woodhead Publishing. p. 73-103.

128. Saleh, T.A., *Chapter 6 - Synthesis of hybrid materials: methods and classification*, in *Polymer Hybrid Materials and Nanocomposites*, T.A. Saleh, Editor. 2021, William Andrew Publishing. p. 177-212.

129. Mazuryk, J., P.S. Sharma, and W. Kutner, *Chapter 8 - Molecularly imprinted polymer composites in drug delivery*, in *Molecularly Imprinted Polymer Composites*, M.P. Sooraj, et al., Editors. 2021, Woodhead Publishing. p. 173-226.

130. Murthy, H.C.A., et al., *17 - Polymer composites for electrochemical sensor applications*, in *Polymeric Nanocomposite Materials for Sensor Applications*, J. Parameswaranpillai and S. Ganguly, Editors. 2023, Woodhead Publishing. p. 405-436.

131. Tran, L.T., et al., *A glassy carbon electrode modified with polyaniline nanowires: An electrochemically effective surface area and an electrocatalytic activity for the oxidation of methanol under alkaline conditions.* Journal of Chemical Research, 2022. **46**(5): p. 17475198221123414.

132. Mustafa, R., et al., *Sensitive detection of mitragynine from Mitragyna speciosa Korth using an electrochemical immunosensor based on multiwalled carbon nanotubes/chitosan- modified carbon electrode.* Sensors and Actuators B: Chemical, 2021. **345**: p. 130356.

133. Shalaby, E.A., et al., *Simultaneous voltammetric sensing of Zn(2+), Cd(2+), and Pb(2+) using an electrodeposited Bi-Sb nanocomposite modified carbon paste electrode.* RSC Adv, 2023. **13**(11): p. 7118-7128.

134. kokab, T., et al., *Tripeptide Derivative-Modified Glassy Carbon Electrode: A Novel Electrochemical Sensor for Sensitive and Selective Detection of Cd2+ Ions.* ACS Omega, 2020. **5**(17): p. 10123-10132.

135. Brett, C., *Electrochemical Impedance Spectroscopy in the Characterisation and Application of Modified Electrodes for Electrochemical Sensors and Biosensors.* Molecules, 2022. **27**: p. 1497.

136. Cruz-Manzo, S. and P. Greenwood, *Chapter 7 - Impedance analysis on the individual cells of a PEMFC stack*, in *Electrochemical Phenomena in the Cathode Impedance Spectrum of PEM Fuel Cells*, S. Cruz-Manzo and P. Greenwood, Editors. 2022, Elsevier. p. 269-310.

137. Kassa, A. and M. Amare, *Highly selective and sensitive differential pulse voltammetric method based on poly (Alizarin)/GCE for determination of cefadroxil in tablet and human urine samples.* Arabian Journal of Chemistry, 2021. **14**(8): p. 103296.

138. Rais, Z., *Chapter 9 - Surface wettability and contact angle measurements of nanocellulose thin films*, in *Properties and Characterization of Nanocellulose and Nanocellulose-Based Composites*, M. Jawaid, R. Khiari, and B. Singh, Editors. 2026, Woodhead Publishing. p. 311-331.

139. Cakir, M., *An inexpensive contact angle measurement system.* Revista Mexicana de Física, 2022. **68**.

140. Chen, X., B. Zheng, and H. Liu, *Optical and digital microscopic imaging techniques and applications in pathology.* Anal Cell Pathol (Amst), 2011. **34**(1-2): p. 5-18.

141. Chen, X., B. Zheng, and H. Liu, *Optical and Digital Microscopic Imaging Techniques and Applications in Pathology.* Analytical cellular pathology (Amsterdam), 2011. **34**: p. 5-18.

142. Gashu, M., et al., *Sensitive and selective electrochemical determination of doxycycline in pharmaceutical formulations using poly(dipicrylamine) modified glassy carbon electrode*. Sensing and Bio-Sensing Research, 2022. **37**: p. 100507.

143. Kok, S.J. and A.J.J. Debets, *Fast sample preparation for analysis of tablets and capsules: the ball-mill extraction method.* Journal of Pharmaceutical and Biomedical Analysis, 2001. **26**(4): p. 599-604.

144. Gashu, M., B.A. Aragaw, and M. Tefera, *Voltammetric determination of oxytetracycline in milk and pharmaceuticals samples using polyurea modified glassy carbon electrode.* Journal of Food Composition and Analysis, 2023. **117**: p. 105128.

145. Naveed, S. and N. Waheed, *Simple UV spectrophotometric assay of ciprofloxacin.* Mintage J. Pharm. Med. Sci, 2014. **3**(4): p. 10-13.

146. Debalke, A., et al., *Synthesis of a novel diaquabis (1, 10-phenanthroline) copper (II) chloride complex and its voltammetric application for detection of amoxicillin in pharmaceutical and biological samples.* Heliyon, 2022. **8**(10).

147. Tsega, T., et al., *Synthesis, structural characterisations, electrochemical behavior and antibacterial activities of a chromium (III) resorcinolate complex.* International Journal of Electrochemical Science, 2024. **19**(8): p. 100659.

148. Zihon, M., et al., *Manganese (II) resorcinolate complex: synthesis, characterizations, electrochemical behavior, and antibacterial activities.* Journal of Applied Electrochemistry, 2025. **55**(3): p. 727-737.

149. Ahmed, H., M. Al-Rasheed, and R.A. Almoaeen, *ICP-OES Method for the Determination of Trace Metals in Nori Seaweed: Application for the Analysis of Different Samples from Different Countries.* Food Analytical Methods, 2024. **17**(4): p. 523-533.

150. Abbasi, M., A.R. Mahmoudi, and K. Asadpour-Zeynali, *Fabrication of a polishable and reusable triple electrode as a new generation of three-electrode systems for the electrochemical analysis applications through both immersion and drop casting-procedures.* Sensing and Bio-Sensing Research, 2024. **43**: p. 100635.

151. Tefera, M., et al., *Simultaneous determination of caffeine and paracetamol by square wave voltammetry at poly(4-amino-3-hydroxynaphthalene sulfonic acid)-modified glassy carbon electrode.* Food Chemistry, 2016. **210**: p. 156-162.

152. Gorup, L.F., et al., *Chapter 2 - Methods for design and fabrication of nanosensors: the case of ZnO-based nanosensor*, in *Nanosensors for Smart Cities*, B. Han, et al., Editors. 2020, Elsevier. p. 9-30.

153. Bedin, K., et al., *Inexpensive Bismuth-Film Electrode Supported on Pencil-Lead Graphite for Determination of Pb(II) and Cd(II) Ions by Anodic Stripping Voltammetry.* International Journal of Analytical Chemistry, 2018. **2018**: p. 1-9.

154. Shitahun, A., et al., *Synthesis, characterization, and application of a novel electrochemical sensor based on poly [Mn(Chr)3]Cl2/PGE for the determination of ciprofloxacin in pharmaceuticals and urine samples.* International Journal of Electrochemical Science, 2025. **20**(3): p. 100937.

155. Mandoj, F., et al., *Porphyrinoid Thin Films for Chemical Sensing*, in *Encyclopedia of Interfacial Chemistry*, K. Wandelt, Editor. 2018, Elsevier: Oxford. p. 422-443.

156. Esmaeily, Z., et al., *Electropolymerization as an electrochemical preconcentration approach for the determination of melamine in milk samples.* Electrochimica Acta, 2021. **390**: p. 138897.

157. Habibi, B. and S. Pashazadeh, *Fabrication, characterization and performance evaluation of an amplified electrochemical sensor based on MOFs nanocomposite for leukemia drug Imatinib determination.* Sensing and Bio-Sensing Research, 2023. **42**: p. 100604.

158. Kenneth, L.B., *Electrochemical Preparation and Characterization of Chemically Modified Electrodes*, in *Voltammetry*, M. Nobanathi Wendy, G. Sandile Surprise, and M. Gugu Hlengiwe, Editors. 2018, IntechOpen: Rijeka. p. Ch. 4.

159. Rao, L.T., et al., *Automated pencil electrode formation platform to realize uniform and reproducible graphite electrodes on paper for microfluidic fuel cells.* Scientific Reports, 2020. **10**(1): p. 11675.

160. Pandey, A., et al., *Review—Pencil Graphite Electrode: An Emerging Sensing Material.* Journal of The Electrochemical Society, 2019. **167**: p. 037501.

161. Abdulghani, A., H. Jasim, and A. Shebeeb Hasan, *Determination of β-lactam Antibiotics in Pharmaceutical Preparations by Uv-visible Spectrophotometry Atomic Absorption and High Performance Liquid Chromatography.* Pakistan Journal of Chemistry, 2012. **2**.

162. Kassa, A. and M. Amare, *Highly selective and sensitive differential pulse voltammetric method based on poly(Alizarin)/GCE for determination of cefadroxil in tablet and human urine samples.* Arabian Journal of Chemistry, 2021. **14**: p. 103296.

163. Debalke, A., et al., *Synthesis of a novel diaquabis(1,10-phenanthroline)copper(II)chloride complex and its voltammetric application for detection of amoxicillin in pharmaceutical and biological samples.* Heliyon, 2022. **8**.

164. Abebe, A. and T. Hailemariam, *Synthesis and Assessment of Antibacterial Activities of Ruthenium (III) Mixed Ligand Complexes Containing 1, 10-Phenanthroline and Guanide.* Bioinorganic chemistry and applications, 2016. **2016**(1): p. 3607924.

165. Abebe, A. and T. Hailemariam, *Synthesis and assessment of antibacterial activities of ruthenium (III) mixed ligand complexes containing 1, 10-phenanthroline and guanide.* Bioinorganic chemistry and applications, 2016. **2016**.

166. Zoubir, J., et al., *Electrocatalytic detection of dimetridazole using an electrochemical sensor Ag@CPE. Analytical application. Milk, tomato juice and human urine.* Sensors International, 2021. **2**: p. 100105.

167. Chang, Y.H., P.M. Woi, and Y. Alias, *Optimization parameters for electropolymerization of melamine in deep eutectic solvent.* Malaysian Journal of Analytical Sciences, 2022. **26**(2): p. 202-214.

168. Granado, V.L.V., et al., *Thin-film electrochemical sensor for diphenylamine detection using molecularly imprinted polymers.* Analytica Chimica Acta, 2014. **809**: p. 141-147.

169. Maji, B., B. Barik, and P. Dash, *Chapter 1 - Methods for design and fabrication of nanosensors*, in *Nanosensors for Smart Manufacturing*, S. Thomas, et al., Editors. 2021, Elsevier. p. 3-18.

170. Suhanto, R.N., et al., *Modified Working Electrode by Magnetite Nanocomposite for Electrochemical Sensor Application.* IOP Conference Series: Materials Science and Engineering, 2018. **367**(1): p. 012054.

171. Zolfaghari Asl, A., A. Rafati, and S. Khazalpour, *Electrocatalytic Behavior of TiO2/MWCNTs Nanocomposite Decorated on Glassy Carbon Electrode for Individual and Simultaneous Voltammetric Determination of Adenine and Guanine in Real Samples.* Journal of The Electrochemical Society, 2022. **169**.

172. Espinoza, E.M., et al., *Practical Aspects of Cyclic Voltammetry: How to Estimate Reduction Potentials When Irreversibility Prevails.* Journal of The Electrochemical Society, 2019. **166**(5): p. H3175.

173. Brett, C.M.A. *Electrochemical Impedance Spectroscopy in the Characterisation and Application of Modified Electrodes for Electrochemical Sensors and Biosensors*. Molecules, 2022. **27**, DOI: 10.3390/molecules27051497.

174. Shen, B. and X. Wen, *Electrochemical oxidation of Ciprofloxacin in two different processes: the electron transfer process on anode surface and the indirect oxidation process in bulk solutions.* Environmental Science: Processes & Impacts, 2018. **20**.

175. Amare, M. and W. Teklay, *Voltammetric determination of paracetamol in pharmaceutical tablet samples using anthraquinone modified carbon paste electrode.* Cogent Chemistry, 2019. **5**(1): p. 1576349.

176. Tasić Ž, Z., et al., *Electrochemical determination of L-tryptophan in food samples on graphite electrode prepared from waste batteries.* Sci Rep, 2022. **12**(1): p. 5469.

177. Brahman, P.K., et al., *Highly sensitive stripping voltammetric determination of a biomolecule, pyruvic acid in solubilized system and biological fluids.* Arabian Journal of Chemistry, 2016. **9**: p. S1897-S1904.

178. Guziejewski, D., et al., *Improved electroanalytical characteristics for flumetralin determination in the presence of surface active compound.* Monatshefte für Chemie - Chemical Monthly, 2017. **148**(3): p. 555-562.

179. Freitas, A. and I. Vieira, *Sensor Modified with Gold Nanoparticles Stabilized in Dialdehyde Starch/DMSO Matrix for Methyldopa Detection.* Electroanalysis, 2022. **35**.

180. Makwakwa, T.A., et al., *Optimization of square wave voltammetry (SWV) parameters by design of experiment (DOE) methodologies for the determination of mifepristone at glassy carbon electrode (GCE).* Electroanalysis, 2022. **34**(7): p. 1103-1113.

181. Alghamdi, A.F., *Validation and application of the square wave voltammetry method for the electrochemical determination of eszopiclone in pharmaceutical formulations and human biological fluids using glassy carbon electrode.* Journal of King Saud University - Science, 2024. **36**(9): p. 103408.

182. Tefera, M., et al., *Voltammetric determination of uric acid using multiwall carbon nanotubes coated-poly(4-amino-3-hydroxy naphthalene sulfonic acid) modified glassy carbon electrode.* Heliyon, 2021. **7**(7): p. e07575.

183. Madhuchandra, H.D. and B.E.K. Swamy, *Electrochemical determination of Adrenaline and Uric acid at 2-Hydroxybenzimidazole modified carbon paste electrode Sensor: A voltammetric study.* Materials Science for Energy Technologies, 2020. **3**: p. 464-471.

184. Smajdor, J., B. Paczosa-Bator, and R. Piech, *Electrochemical Sensor Based on the Hierarchical Carbon Nanocomposite for Highly Sensitive Ciprofloxacin Determination.* Membranes (Basel), 2023. **13**(7).

185. Garbellini, G., R. Rocha-Filho, and O. Fatibello-Filho, *Voltammetric determination of ciprofloxacin in urine samples and its interaction with dsDNA on a cathodically pretreated boron-doped diamond electrode.* Anal. Methods, 2015. **7**.

186. Akyüz, B.G., et al., *Determination of ciprofloxacin in pharmaceutical dosage, human serum and urine, using molecularly imprinted polymer modified electrode by voltammetry.* Avrupa Bilim ve Teknoloji Dergisi, 2020(20): p. 859-865.

187. Ren, S., et al., *Perspective and application of modified electrode material technology in electrochemical voltammetric sensors for analysis and detection of illicit drugs.* Sensors and Actuators A: Physical, 2021. **329**: p. 112821.

188. Cazedey, E.C.L. and H.R.N. Salgado, *Spectrophotometric determination of ciprofloxacin hydrochloride in ophthalmic solution.* Advances in Analytical Chemistry, 2012. **2**(6): p. 74-79.

189. Abebe, A. and T. Hailemariam, *Synthesis and Assessment of Antibacterial Activities of Ruthenium(III) Mixed Ligand Complexes Containing 1,10-Phenanthroline and Guanide.* Bioinorganic Chemistry and Applications, 2016. **2016**: p. 1-9.

190. Saito, M., et al., *Electrochemical polymerization of tetraphenylporphyrinatoruthenium(II) complexes with diaza compounds as axial ligands.* Electrochimica Acta, 2000. **45**(18): p. 3021-3028.

191. Moulya, K.P., et al., *Polymer modified carbon paste electrode for the electrochemical analysis of Tartrazine.* Results in Chemistry, 2023. **5**: p. 100809.

192. Tanner, E. and R. Compton, *How can Electrode Surface Modification Benefit Electroanalysis?* Electroanalysis, 2018. **30**.

193. Elugoke, S.E., et al., *Electrochemical sensor for the detection of adrenaline at poly(crystal violet) modified electrode: optimization and voltammetric studies.* Heliyon, 2022. **8**(10): p. e10835.

194. Jhaveri, J.H. and Z.V.P. Murthy, *A comprehensive review on anti-fouling nanocomposite membranes for pressure driven membrane separation processes.* Desalination, 2016. **379**: p. 137-154.

195. Argoubi, W., et al., *Sensitive detection of ascorbic acid using screen-printed electrodes modified by electroactive melanin-like nanoparticles.* RSC Advances, 2019. **9**: p. 37384-37390.

196. Masood, Z., H. Muhammad, and I.A. Tahiri *Comparison of Different Electrochemical Methodologies for Electrode Reactions: A Case Study of Paracetamol*. Electrochem, 2024. **5**, 57-69 DOI: 10.3390/electrochem5010004.

197. Lotfipour, F., et al., *Electrochemical late-stage modification of hydralazine an antihypertensive drug. A green strategy for the synthesis of nano-structured new sulfonylhydrazine derivatives.* Green Synthesis and Catalysis, 2024.

198. Sultan, S., et al., *Calix[4]arene Derivative-Modified Glassy Carbon Electrode: A New Sensing Platform for Rapid, Simultaneous, and Picomolar Detection of Zn(II), Pb(II), As(III), and Hg(II).* ACS Omega, 2019. **2019**.

199. Tabanlıgil Calam, T. and G. Taşkın Çakıcı, *Optimization of square wave voltammetry parameters by response surface methodology for the determination of Sunset yellow using an electrochemical sensor based on Purpald®.* Food Chemistry, 2023. **404**: p. 134412.

200. Biya, S., et al., *Highly sensitive square wave voltammetric method for determination of brucine in artificial urine samples based on choline chloride modified glassy carbon electrode*. Heliyon, 2023. **9**(3): p. e14544.

201. Qu, K. and D. Dan, *Chapter 1 - Introduction*, in *Environmental Analytical Chemistry*, K. Qu and D. Dan, Editors. 2024, Elsevier. p. 1-33.

202. Xu, J., et al., *A critical view on spike recovery for accuracy evaluation of analytical method for medicinal herbs.* Journal of Pharmaceutical and Biomedical Analysis, 2012. **62**: p. 210-215.

203. Baskaran, N., et al. *The High Stability and Selectivity of Electrochemical Sensor Using Low-Cost Diamond Nanoparticles for the Detection of Anti-Cancer Drug Flutamide in Environmental Samples*. Sensors, 2024. **24**, DOI: 10.3390/s24030985.

204. Vaz, S., *Chapter 4 - Fundamentals of analytical chemistry*, in *Analysis of Chemical Residues in Agriculture*, S. Vaz, Editor. 2021, Elsevier. p. 85-109.

205. Dang, J., et al., *Determination of Norfloxacin Using a Tetraoxocalix[2]arene[2]triazine Covalently Functionalized Multi-walled Carbon Nanotubes Modified Electrode.* Anal Sci, 2019. **35**(9): p. 979-985.

206. Huang, K.-J., et al., *Electrochemical behavior and voltammetric determination of norfloxacin at glassy carbon electrode modified with multi walled carbon nanotubes/Nafion.* Colloids and Surfaces B: Biointerfaces, 2008. **64**(2): p. 269-274.

207. da Silva, H., et al., *Molecularly imprinted sensor for voltammetric detection of norfloxacin.* Sensors and Actuators B: Chemical, 2015. **219**: p. 301-307.

208. Ghosal, S., et al., *Desmodium alkaloids1*. Planta Medica, 1973. **23**(04): p. 321-329.

209. Azizi, S., M. Chaichi, and M. Yousefi, *Investigation of solvent effects on UV–vis absorption spectra of dihydroxybenzene derivatives by solvatochromic parameters.* Spectrochimica Acta Part A: Molecular and Biomolecular Spectroscopy, 2009. **73**(1): p. 101-105.

210. Živanović, S.C., R.S. Nikolić, and G.M. Nikolić, *The influence of Mg (II) and Ca (II) ions on rutin autoxidation in weakly alkaline aqueous solutions.* Acta Facultatis Medicae Naissensis, 2016. **33**(3): p. 163-171.

211. Chiyindiko, E., E.H. Langner, and J. Conradie, *Spectroscopic behaviour of copper (II) complexes containing 2-hydroxyphenones.* Molecules, 2022. **27**(18): p. 6033.

212. Azizi, S.N., M.J. Chaichi, and M. Yousefi, *Investigation of solvent effects on UV–vis absorption spectra of dihydroxybenzene derivatives by solvatochromic parameters.* Spectrochimica Acta Part A: Molecular and Biomolecular Spectroscopy, 2009. **73**(1): p. 101-105.

213. Wong, K., et al., *Review of Spectrometric Identif ication of Organic Compounds, 8th Edition.* Journal of chemical education, 2015. **92**.

214. Patel, K.D. and H.S. Patel, *Synthesis, spectroscopic characterization and thermal studies of some divalent transition metal complexes of 8-hydroxyquinoline*. Arabian Journal of Chemistry, 2017. **10**: p. S1328-S1335.

215. Nakamoto, K., *Infrared and Raman spectra of inorganic and coordination compounds, part B: applications in coordination, organometallic, and bioinorganic chemistry*. 2009: John Wiley & Sons.

216. Roselló-Márquez, G., et al., *Electropolymerization of PPy, PEDOT, and PANi on WO3 nanostructures for high-performance anodes in Li-ion batteries.* Heliyon, 2024. **10**(24): p. e41075.

217. Tsuji, K., T. Maeda, and A. Hotta, *9 - Polymer Surface Modifications by Coating*, in *Printing on Polymers*, J. Izdebska and S. Thomas, Editors. 2016, William Andrew Publishing. p. 143-160.

218. Turbale, M., et al., *Adsorptive stripping voltammetric determination of Tetracycline in pharmaceutical capsule formulation using Poly(Malachite green) modified glassy carbon electrode*. Heliyon, 2020. **6**(12): p. e05782.

219. Kassa, A., et al., *Potentiodynamic poly (resorcinol)-modified glassy carbon electrode as a voltammetric sensor for determining cephalexin and cefadroxil simultaneously in pharmaceutical formulation and biological fluid samples.* ACS omega, 2022. **7**(38): p. 34599-34607.

220. Galeano-Díaz, T., et al., *Adsorptive stripping square wave voltammetry (Ad-SSWV) accomplished with second-order multivariate calibration.* Analytica chimica acta, 2008. **618**: p. 131-9.

221. Metto, M., et al., *Novel Poly (Cytosine) Based Electrochemical Biosensor for Sensitive and Selective Determination of Guanine in Human DNA, Blood Serum, and Urine Samples.* Blood Serum, and Urine Samples.

222. Amiri-Aref, M., J.B. Raoof, and R. Ojani, *A highly sensitive electrochemical sensor for simultaneous voltammetric determination of noradrenaline, acetaminophen, xanthine and*

*caffeine based on a flavonoid nanostructured modified glassy carbon electrode.* Sensors and Actuators B: Chemical, 2014. **192**: p. 634-641.

223. Amare, M. and S. Aklog, *Electrochemical Determination of Caffeine Content in Ethiopian Coffee Samples Using Lignin Modified Glassy Carbon Electrode.* J Anal Methods Chem, 2017. **2017**: p. 3979068.

224. Vargas Ramos, D., et al., *Device for Electrochemical Caffeine Analysis in Fluids (DECAF): A Stir-Bar-Embedded Sensor for Real-Time Caffeine Analysis in Commercial and Homemade Beverages.* Small, 2025. **21**(45): p. e06439.

225. Dang, J., et al., *Determination of norfloxacin using a tetraoxocalix [2] arene [2]-triazine covalently functionalized multi-walled carbon nanotubes modified electrode.* Analytical Sciences, 2019. **35**(9): p. 979-985.

226. Goyal, R., A. Raj, and H. Chasta, *Electrochemical sensor for the sensitive determination of norfloxacin in human urine and pharmaceuticals.* Bioelectrochemistry (Amsterdam, Netherlands), 2011. **83**: p. 46-51.

227. Karahan, F., et al., *Electrochemical determination of fluoroquinolone antibiotic norfloxacin in the presence of anionic surfactant using the anodically pretreated boron-doped diamond electrode.* ChemistrySelect, 2020. **5**(42): p. 12862-12868.